MULTICOMPONENT CRYSTALS OF SELECTED HYDROXYCINNAMIC ACIDS

by

SOSTHENE NYOMBA KAMANDA

Dissertation submitted in fulfilment of the requirements for the degree

Master of Applied Science: Chemistry

in the Faculty of Applied Sciences

at the Cape Peninsula University of Technology

Supervisor: Prof. Ayesha Jacobs

Cape Town
April 2019

DECLARATION

I, Sosthene Nyomba Kamanda, declare that the contents of this dissertation/thesis represent my own unaided work and that the dissertation/thesis has not previously been submitted for academic examination towards any qualification. Furthermore, it represents my own opinions and not necessarily those of the Cape Peninsula University of Technology.

_____   _____

Signed   **Date**

ABSTRACT

The solid-state modification of a given active pharmaceutical ingredient is a desired way to alter its physicochemical properties, such as solubility or bioavailability. Multicomponent crystals constructed with *p*-coumaric acid (*p*CA) and *trans*-ferulic acid (TFA) were investigated with the amines (2-amino-4-picoline (2A4MP), 2-amino-6-picoline (2A6MP), 4,4'-bipyridine (BIPY) and pyridine (PYR)) and 1,4-dioxane (DX). Eight compounds were prepared using the slow evaporation technique. *p*CA formed one co-crystal, two salts and two solvates while TFA formed a co-crystal, a salt and a solvate. The crystal structures were determined using single crystal X-ray diffraction crystallography. Further characterisations were done using thermal analysis and FTIR spectroscopy. Z' > 1 was observed for some of the crystal structures of *p*CA. The solvent assisted grinding method for preparation of these compounds was not successful as they all resulted in unknown compounds. The Hirshfeld analysis confirmed that the crystal structures generated in this study were dominated by hydrogen bonding (O-H•••O, O-H•••N and C-H•••O) and the π-π stacking had minimal contribution in the packing arrangement of the new solid forms.

ACKNOWLEDGEMENT

I wish to thank:

- My family, friends and colleagues for their support and encouragement.
- My supervisor, Prof. Ayesha Jacobs for her willingness to help and support.
- The Department of Chemistry at CPUT.

DEDICATION

I dedicate this work to my family and to my beloved friends.

TABLE OF CONTENTS

TABLE OF FIGURES

TABLE OF TABLES

GLOSSARY

Terms/ Acronyms/ Abbreviations   Definition/ Explanation

α, β and γ	: Angle between b and c unit cell axes
a, b and c	: Unit cell axes
Dcal	: Calculated density
Goof	: Goodness of fit
kDa	: kilodalton
T_{on}	: Onset temperature
V	: Unit cell volume
Z	: Number of formula units per cell
CSD	: Cambridge Structural Database
PXRD	: Powder X-ray Diffraction
TGA	: Thermogravimetry Analysis
DSC	: Differential Scanning Calorimetry
2-A4MP	: 2-amino-4-methylpyridine
2-A6MP	: 2-amino-6-methylpyridine
BIPY	: 4,4'-Bipyridine
DX	: 1,4-dioxane
PYR	: Pyridine

ATOM COLOURS
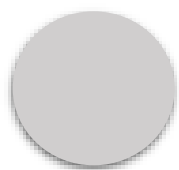
Carbon
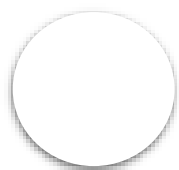
Hydrogen

Nitrogen
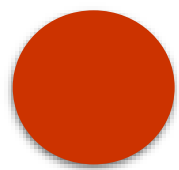
Oxygen

CHAPTER 1: INTRODUCTION

1.1 Background

Chemistry is the study of matter and its properties. Matter forms when atoms or molecules come together through a bond or bonds. Understanding the attractive forces between atoms or molecules and the strength of these forces is important in understanding under which conditions matter exists as a solid, liquid and gas (William, 2017). Chemical bonds dictate structures and bulk properties of matter. In the gas phase, the attractive forces are weak as atoms or molecules behave independently. This is the result of the entities having large kinetic energy, thus weakening the attractive forces between them. In the liquid phase, the attractive forces are moderate as the kinetic energy is low compared to that of the gas phase leading to the strengthening of the attractive forces between molecules. In the solid phase, the attractive forces are strong such that atoms or molecules gain as many interactions as possible in a minimum energy configuration. In the same way, crystals form as molecules are held together in a solid form under the influence of intermolecular forces while minimizing the repulsive intermolecular forces (Bennett, 2010).

A crystal can be defined as a solid material whose constituents are arranged in a highly ordered microscopic structure, which has essentially a sharp diffraction pattern. It is interesting and challenging to study crystals as they are an assembly of molecules that are held together by intermolecular forces. When two or more molecules are assembled, the new properties are often a better version of the two individual molecule's properties. Time and money are required to research and develop an active pharmaceutical ingredient (API) in a solid form but it is unfortunate that some of them show poor properties and therefore cannot be released onto the market (Chadha, *et al*., 2011).

To remediate these poor properties, research is conducted by scientists to enrich those APIs to drug candidates by designing new solid forms. Designing new solids with desired physicochemical properties is difficult, thus it is particularly important to understand intermolecular forces. Crystal formation depends on the solution media, temperature, and pressure. Consequently, it is said that the crystalline phase is thermodynamically favoured at high pressures and low temperatures in a favourable medium (Markov, 2016). The

intermolecular forces are responsible for the physicochemical properties and crystal engineering can be utilized to improve the physicochemical properties of an API.

These properties include solubility, stability and bioavailability without compromising the stability of the solid form (Sanphui, *et al*., 2011). Sanphui et al. reported an improvement in the dissolution rate of curcumin-resorcinol and curcumin-pyrogallol that are 5 to 12 times faster than that of curcumin alone, in that order.

1.2 Supramolecular chemistry

Supramolecular chemistry is defined by the Nobel laureate Jean Marie Lehn as the chemistry beyond the molecule (Lehn, 1985). In other words, it is the study of how chemical entities are held together by intermolecular forces (Ariga & Kunikate, 2006). The origin of supramolecular chemistry can be traced back to the concepts of the lock-and-key model (Fischer, 1894). The discipline has been enhanced by research in the 1960's and 1970's involving host-guest systems (Cram & Cram, 1974) for selective binding of small alkali metal cations by macrocyclic receptors, which encompassed mostly crown ethers (Pedersen, 1967) and cryptands (Dietrich, et al., 1969). An understanding of the affinity that lead molecules in nature to recognize and bind (the self-assembly of DNA, antigen-antibody recognition and protein folding), motivated chemists to study supramolecular systems. (MacGillivray & Atwood, 1997). Supramolecular chemistry is classified into two categories: the chemistry associated with a molecule recognizing a partner molecule, "molecular recognition", and the chemistry of molecular assembly from numerous molecules (Schneider, 2012).

1.2.1 Molecular recognition

Molecular recognition is regarded as the multistep procedure in which molecules recognize each other due to complementarity (Gorbitz, 2017). The interaction of molecules in the binding process requires the following: functional groups, configuration and chirality, size and shape, interactive bonds and positioning of structures. Thus, molecular recognition forms the basis of supramolecular chemistry because the construction of a supermolecule involves selective molecular combination (Chatterji, 2016). Figure 1.1 illustrates the schematic representation of molecular recognition.
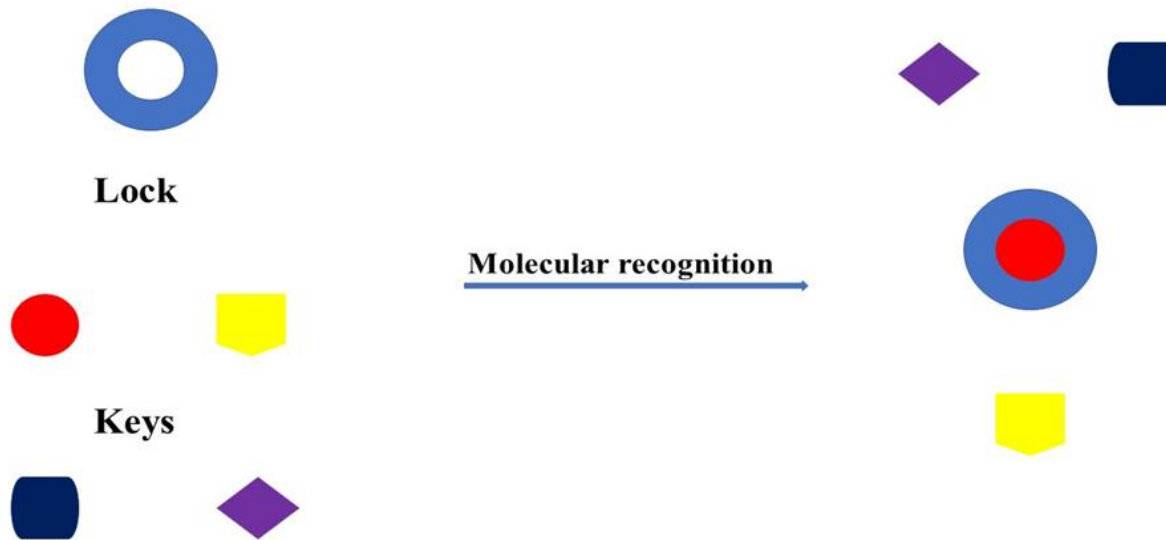
Figure 1.1: Schematic representation of molecular recognition

1.2.2 Molecular self-assembly

Molecular self-assembly, by definition, is the spontaneous organization of molecules to form a definite stable arrangement through various non-covalent interactions (Palmer & Stupp, 2008). The organization of the self-assembled structure is maintained by a balance of weaker intermolecular forces. The key component of molecular self-assembly is chemical complementarity and structural compatibility (Fujita, 2003). For example, when two polar molecules come into proximity, an attractive interaction can develop as the positively-charged region in one molecule interacts with the negatively-charged region of the second molecule. In Figure 1.2, it is clearly seen that there is a natural attraction between component **A** and **B** in terms of shape and size resulting in the complex component **C**.
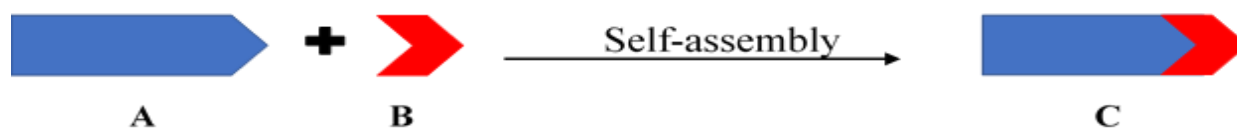
Figure 1.2: Schematic representation of molecular self-assembly

3

1.2.3 Intermolecular forces and hydrogen bond role

Matter results in a rich enticing variety of species held together by stabilising interactions. This can be divided into two categories, short-range and long-range. Short-range forces (e.g. covalent) are responsible for the formation of molecular systems (Maitland, et al., 1981). Long-range interactions include dipole-dipole, π-π and hydrogen bonds, are those that contribute to the association of molecules into supramolecular structures with defined stoichiometries. A thorough knowledge of the non-covalent interactions is required, their various types and relative strengths as it is of crucial importance to control supramolecular assemblies. A general comparison of selected chemical bond types is presented in Table 1.1.

Table 1.1: Comparison of selected chemical bond types and their features.

Chemical bonds	Bond energies (kJ/mol)	Building blocks	Products	Features
Covalent	200-400	Atoms	Molecules	$\Delta H > T\Delta S$ MW: 1 - 1000 g mol^{-1} Solvent effect: Secondary
Hydrogen bond **Dipole-dipole** **π-π stacking** **Van der Waals**	4-120 5-50 <50 <5	Molecules	Supramolecules	$\Delta H \approx T\Delta S$ MW: 1 - 100 kg mol^{-1} Solvent effect: Primary

Dipole-dipole and ion-dipole interactions play important roles in neutral species instead of electrostatic interactions. Hydrogen bonding is weaker than the electrostatic interactions, and it only occurs when the functional groups that are interacting are properly oriented (Jeffrey, 1997). The contribution of hydrogen bonding in designing novel materials is dominant with both weak and strong hydrogen bonded interactions. Therefore, it is taken as the means to design new materials capable of self-assembly into well-ordered crystal structure due to its strength and directionality.

Hydrogen bonding is referred to as an attractive weak electrostatic chemical interaction which forms between covalently bonded hydrogen atoms and strongly electronegative atoms with a lone pair of electrons, such as nitrogen, oxygen or fluorine in the same or different molecule (Steed & Atwood, 2009). Hydrogen bonding is denoted as D-H•••A, with D-H being the donor group and A the acceptor (Desiraju, *et al*., 2011). A hydrogen atom can act as a donor when its

dipole moment is induced by an atom whose electronegativity is higher than the connected hydrogen atom to form a hydrogen bond with another atom of higher electronegativity. Yet, if the difference in electronegativity is not large enough, this bond may be regarded as very weak and can be considered as van der Waals forces. Thus, oxygen and nitrogen are the most typical and strongest hydrogen bonding acceptors due to their high electronegativity and polarity. Hydrogen bonds are subdivided into three categories (weak, moderate and strong) (Jeffrey, 1997). The concept is explained by Desiraju according to their hydrogen bond properties, Table 1.2 (Desiraju, 2011).

The strength of hydrogen bonds are strongly influenced by the solvent system. The polar aprotic solvents, such dimethyl sulfoxide, *N'N*-dimethyl-formamide or acetonitrile, are strong hydrogen bond acceptors and they can weaken or destroy strong hydrogen bonding. Polar protic solvents, such as water, methanol and ethanol, behave both as donors and acceptors, can also compete with the solute molecule whose hydrogen bonds are relatively strong as the ones provided by these protic solvents. Thus, the choice of solvent is crucial in designing crystal structures (Pihko, 2009). A solvent maybe seen trapped in a crystal through hydrogen bonding to the target molecule or to fill the space formed due to the rigidity of the molecule when the solvent can act as donor/ acceptor (Li & Wu, 2015).

Table 1.2 : Types of hydrogen bonds

Strength	Example	$D \cdots A$ $(d_{D \cdots A}, \text{Å})$	$H \cdots A$ $(d_{H \cdots A}, \text{Å})$	$D\text{-}H \cdots A$ (θ)
Very strong	$[F - H - F]^-$	2.2-2.25	1.2-1.5	175-180
Strong	O-H⋯O-H	2.6-3.0	1.6-2.2	145-180
	O-H⋯N-H	2.6-3.0	1.7-2.3	140-180
	N-H⋯O=C	2.8-3.0	1.8-2.3	150-180
	N-H⋯O-H	2.7-3.1	1.9-2.3	150-180
	N-H⋯N-H	2.8-3.1	2.0-2.5	150-180
Weak	C-H⋯O	3.0-4.0	2.0-3.0	110-180

1.3 Crystal engineering

The concept of crystal engineering was first introduced by Pepinsky in 1955. It was further implemented by Gerhardt Schmidt in 1960 (Tiekink, *et al*., 2010). Crystal engineering is defined by Desiraju as "the understanding of the intermolecular interactions in the context of crystal packing and the utilization of such understanding in the design of new solids with desired physical and chemical properties" (Desiraju, *et al*., 2011). Precise prediction of supramolecular architecture is ambiguous even with the most intense computational methodologies. It is not easy to predict whether crystallisation will take place and what properties the new solid will have. Crystal packing is governed by many weak non-covalent intermolecular forces (Evans & Lin, 2002). Thus, it is important to study the properties of both components such as pK_a, functional groups present and solubility. Through this information, a supramolecular structure can be synthesised (Desiraju *et al*, 2011).

1.4 Cambridge structural database

To derive knowledge from the crystal engineering literature and integrity of the new information that will be used as a prerequisite for the formation of new solids, crystal structures are deposited in the Cambridge Structural Database, CSD (Allen & Kennard, 1993). Recently, the database celebrated its one-millionth structure (Robinson, *et al*., 2019). The CSD is a database developed by crystallographers to store/archive new crystal structures and new structural discoveries. It contains a collection of X-ray and neutron diffraction data for both small-molecule organic and metal-organic crystal structures (CSD version 5.40, November 2018). Therefore, it is important that a search of the CSD is done prior to any crystal engineering project as the CSD provides an overview of the arrangement of compounds within crystals (Allen, *et al*., 1983). A new crystal structure is accepted into this collection by assessing it with the previously established structures and this is applied at both molecular and supramolecular levels (Authier, 2013).

1.5 Supramolecular synthon

The concept of a synthon was first introduced in synthetic chemistry by Corey in 1965 and defined as structural units within molecules that can be formed or assembled by known or conceivable synthetic operations. In crystal engineering, the concept of a supramolecular synthon was introduced by Desiraju in 1995 (Nangia & Desiraju, 1998).

A supramolecular synthon is defined as a robust structural unit within a supermolecule which can be formed by known or conceivable intermolecular interactions. The term has been used since to represent the key structural unit in target molecules (Moulton & Zaworotko, 2001). Supramolecular synthons depict the various ways in which complementary portions of molecules approach one another. (Aakeröy & Sinha, 2018). A supramolecular synthon is important as it remains intact from one network structure to another irrespective of other existing functionality, which ensures repeatability and generality (Mirzaei, *et al*., 2018).

Synthons can be classified as homosynthons or heterosynthons. Homosynthons are formed by self-complementary molecules, for example, the carboxylic acid dimer and amides dimer. Heterosynthons are kinetic units that concentrate most importantly on the chemical moieties and geometrical recognition between two or more different molecular components, this is shown in Figure 1.3.

Homosynthon   **Heterosynthon**

Figure 1.3: Schematic representation of supramolecular synthons

1.6 Multicomponent crystal

Multicomponent crystals are structurally homogeneous crystalline materials containing two or more building blocks present in definite stoichiometric amounts (Desiraju, 2002). The design and synthesis of multicomponent crystals have considerable therapeutic and commercial benefits as they often lead to improvement of physicochemical properties like solubility, bioavailability, stability and dissolution rate.

In the process of designing a crystal, the identification of a suitable solid form is the first and foremost step. A solid should possess specific characteristics for it to be suitable in the design of a crystal. The solid should be stable under different humidity and temperature conditions, (Herbstein, 2005). Multicomponent crystals encompass co-crystals, molecular salts, hydrates and solvates.

1.6.1 Co-crystal and salt

Co-crystals or organic salts are solids that are crystalline materials composed of two or more different molecular compounds generally in a stoichiometric ratio (Lombard, *et al.*, 2018). Organic salts and co-crystals are multicomponent crystals that can be distinguished by the location of a proton between an acid and a base. In a salt, proton transfer is observed which is not the case in a co-crystal (Karki, *et al*., 2009). The nature of the substituent of the donating molecule is the key in the donating ability of a carboxylic acid group. If the substituent is an electron withdrawing group, the acidity of the species will increase relative to the carboxylic acid, whereas an electron donating group reduces the acidity. The same analogy is also applied but in the opposite way for a given hydrogen bond accepting molecule (Seaton, 2011). The reaction of an acid and a base will produce organic salts or co-crystals depending on the pK_a difference of an acid and a base. According to the previous observations on the pK_a rule in the literature, if the ΔpK_a (pK_a base $-pK_a$ acid) is less than -1, non-ionised acid-base complexes are exclusively observed. Ionized acid-base complexes are exclusively expected for ΔpK_a greater or equal to 4 (Cruz-Cabeza, 2012). This is not always the case, because the pK_a is an acid dissociation constant measured in water at a fixed temperature. When the ΔpK_a falls between -1 and 4, there is a probability of having either a salt or co-crystal (Ramon *et al*, 2013).

1.6.2 Hydrate and solvate

Solvates are crystalline materials in which solvent molecules are incorporated in the crystal lattice. When the incorporated solvent is water, the solvate crystals are termed hydrates (Goèrbitz & Hersleth, 2000). Hydrates can be classified as isolated hydrates, channel hydrates and ion-associative hydrates. In isolated hydrates, the water molecules are isolated from each other by the host molecule in the crystal lattice. A channel hydrate occurs when the water molecules are linked to one another to form a channel. The water molecules might be present either

stoichiometrically or non-stoichiometrically inside the crystal lattice. Ion-associative hydrates are typically seen when the water is metal ion coordinated (Schmidt & Schwarz, 2006).

Hydrates are known to be formed as either stoichiometric or non-stoichiometric hydrates and can be classified as a: monohydrate, semihydrate, hemihydrate, sesquihydrate, dehydrate, trihydrate or simply hydrate (Chorgrade, 2007).

1.7 X-ray crystallography

The work of Max von Laué and the Braggs (father and son) enhanced the concept of crystals with a clear definition of them as periodic arrays that are capable of diffracting X-rays (Woolfson, 1997). X-ray crystallography is the study of crystal substances based on their ability to diffract an incident electron/X-ray beam causing it to scatter in specific directions (Warren, 1990). The crystallographic technique can provide, with certainty, the molecular structure of a given compound in the solid crystalline state. The technique is known as crystal structure determination because the object studied is a crystalline sample. In a crystal, there are large numbers of identical molecules, locked in a regular arrangement, which together gives significant scattering (William, 2015). A detailed picture of the crystal structure is obtained at the atomic level when the experiment is completed (Datta & Grant, 2004).

1.8 Hirshfeld surfaces

Hirshfeld surfaces are used to visualize and analyse packing modes and intermolecular interactions in molecular crystals that is different to the conventional crystal structure analysis method. The Hirshfeld surface divides the crystal into regions where the electron distribution of a sum of spherical atoms for the molecule dominates the corresponding sum over the crystal. The crystallographic information file (CIF) is given as input to the Crystal Explorer program (Turner, et al., 2017) which generates Hirshfeld surfaces and a two-dimensional (2D) fingerprint plot. The 2D fingerprint plot condenses information into a single picture which summarizes quantitatively the types of intermolecular contacts experienced by molecules in the bulk (McKinnon, *et al*., 2004). A whole molecule approach to understanding intermolecular interactions in conjunction with more direct atom-atom approach to gain fuller insight of the important interactions in a molecular crystal is explored. Each surface point, both the distance and the identity of the nearest atoms internal and external to the surface is required to display d_{norm} (Wolff, *et al*., 2012).

1.9 Aspects of this research

The aim of this research is to synthesise and characterise multicomponent crystals of the selected hydroxycinnamic acids, *p*-coumaric acid, and *trans*-ferulic acid. A search of the CSD (May 2019 update) resulted in five multicomponent structures of *p*-coumaric acid (*p*CA) and seven multicomponent crystals of *trans*-ferulic acid (TFA). Thus, there are few crystal structures of these two compounds reported in the literature. Hydroxycinnamic acids are important natural phenolic antioxidants. They are of great importance regarding human health as the studies conducted showed that they are anticarcinogenic (Ferguson, *et al*., 2005) and also have antioxidant and anti-inflammatory properties (Luceri, et al., 2007). Hydroxycinnamic acids are present at relatively high percentages in herbaceous plants, of which *p*CA and TFA are the most prevalent (Blokker, *et al*., 2004). The two hydroxycinnamic acids differ structurally due to the substituted methoxy group present in the *meta* position in TFA. *p*CA and TFA both contain carboxylic acid (hydrogen bond donor) and hydroxyl (hydrogen bond acceptor) functional groups. The carboxylic acid group of the hydroxycinnamic acids with its ability to donate a proton can be considered as a possible way of forming salts or synthons. In this study, *p*CA and TFA were combined with amides, amines, and 1,4-dioxane as co-formers to form multicomponent crystals. These co-formers were selected according to their ability to form hydrogen bonds via O-H•••N or N-H•••O interactions. Eight new multicomponent crystals were prepared. *p*CA formed one co-crystal, two salts and two solvates while TFA formed one co-crystal, one salt and one solvate. Figure 1.4 shows the structures of both starting materials and the co-formers that were successful in producing new solid forms. All solid forms were characterised using well-known techniques including;

- Thermal analysis - thermogravimetry (TG) and differential scanning calorimetry (DSC).
- Powder X-ray diffraction and single crystal X-ray diffraction.
- Fourier transform infrared (FTIR) spectroscopy.
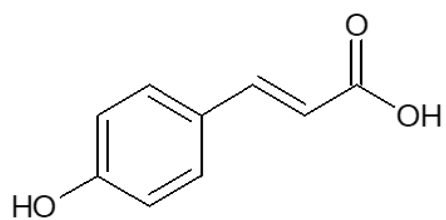
_p_CA
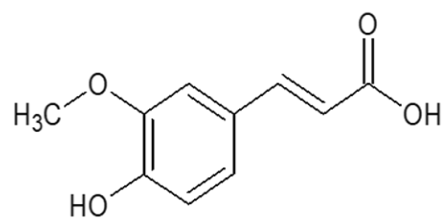
TFA
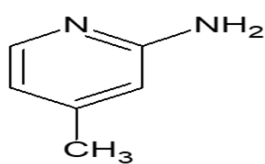
2A4MP
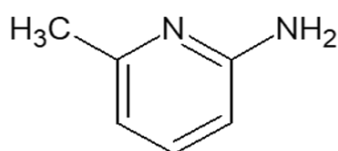
2A6MP
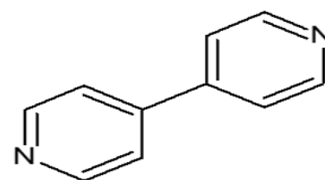
BIPY
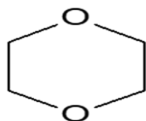
DX
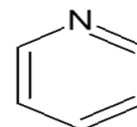
PYR

Figure 1.4: Structural line diagrams of _p_-coumaric acid (_p_CA), _trans_-ferulic acid (TFA), pyridine (PYR), 2-amino-6-picoline (2A6MP), 2-amino-4-picoline (2A4MP), 4,4'-bipyridine (BIPY) and 1,4-dioxane (DX).

1.10 References

Aakeröy, C. B. & Sinha, A. S., 2018. *Co-crystals: Preparation, characterization, and applications.* s.l.:Royal Society of Chemistry.

Allen, F. H. & Kennard, O., 1993. *Chem. Des. Autom. News,* Volume 8, p. 31.

Allen, F. H., Kennard, O. & Taylor, R., 1983. *Acc. Chem. Res. ,* Volume 16, p. 146.

Ariga, K. & Kunikate, T., 2006. *Supramolecular chemistry: Fundamentals and applications.* Tokyo: Springer.

Atwood, J. & Steed, J., 2004. *Encyclopedia of supramolecular chemistry.* 1st ed. New York : M. Dekker .

Authier, A., 2013. *Early days of X-ray crystallography.* 1st ed. Oxford : Oxford University Press.

Bauer, R., Birk, J. & Marks, P., 2007. *A conceptual introduction to chemistry.* s.l.:McGraw-Hill Higher Education.

Behr, J.-P., 1994. *The lock and Key principle: the state of the art 100 years on.* 1st ed. Chichester : John Wiley & Sons.

Bennett, D., 2010. Understanding single crystal X-ray crystallography. *Wiley.*

Blokker, P., Boelen, P., Broekman, R. & Rozema, J., 2004. The occurrence of p-coumaric acid and ferulic acid in fossil plant materials and. *Springer ,* Volume 182, p. 197 –207.

Brescia, F., 1975. *Fundamentals of chemistry: laboratory studies.* 3rd ed. ed. New York: Academic Press.

Buckingham, A. D., Legon, A. C. & Roberts, S. M., 1993. *Principals of molecular recognition.* 1st ed. Dordrecht : Springer Science.

Chadha, R. et al., 2011. Multicomponent solids of lamotrigine with some selected coformers and their characterization by thermoanalytical, spectroscopy and X-ray diffraction methods. *CrysEngCom,* Volume 13, pp. 6271-6284.

Chatterji, D., 2016. *Basis of molecular recognition.* Bangalore: CRC Press.

Clugston, M., Flemming, R. & Vogt, D., 2002. *Chemistry: an introduction for Southern African students.* Oxford: Oxford University Press.

Cram, D. J. & Cram, J. M., 1974. Science. Volume 183, p. 803.

Cruz-Cabeza, A., 2012. Acid-base crystalline complexes and the pKa rule. *CrystEngComm,* Volume 14, pp. 6362-6365.

Datta, S. & Grant, D. J. W., 2004. Crystal structure of drugs: advances in determination, prediction, and engineering. *Nature Reviews Drug Discovery.*

Desiraju, G., 2002. hydrogen bridges in crystal engineering: interactions without borders. *Accounts of chemical research.*

Desiraju, G., 2011. *Pharmaceutical salts and co-crystals: retrospect and prospects.*
Desiraju, G., Vital, J. & Ramanan, 2011. *Crystal Engineering : a textbook.* s.l.:World Scientific .

Dietrich, B., Lehn, J. M. & Sauvage, J. P., 1969. Tetrahedron Lett. p. 2889.

Evans, O. & Lin, W., 2002. Crystal engineering of NLO materials based on metal-organic coordination networks. *Account of Chemical Research ,* Volume 35, pp. 511-522.

Ferguson, L., Shuo-tun, Z. & Harris, P., 2005. Antioxidant and antigenotoxic effects of plant cell wall hydroxycinnamic acids in cultured HT-29 cells. *Mol. Nutr. Food Res,* Volume 49, p. 585 – 693.

Fischer, E., 1894. *Deutsch. Chem. Ges.,* Volume 27, p. 2985.

Fujita, M., 2003. Molecular self-assembly: organic versus inorganic approaches. *Springer,* Volume 96.

Goèrbitz, C. & Hersleth, H., 2000. On the inclusion of solvent molecules in the crystal structures of organic compounds. *Acta Crystallogr,* Volume 56, p. 526−534.

Gorbitz, C., 2017. *Basic of molecular recognition.* s.l.:s.n.

Jeffrey, G. A., 1997. *An Introduction to hydrogen bonding.* Oxford: Oxford University Press.

Jeffrey, G. & Saenger, W., 2012. Hydrogen bonding in biological structures. *Springer Science & Business Media.*

Karki, S., Friščić, T. & Jones, W., 2009. Control and interconversion of cocrystal stoichiometry in grinding: stepwise mechanism for the formation of a hydrogen-bonded cocrystal. *CrystEngComm,* Volume 11, pp. 470-481.

Kotz, J. C., 2009. *Chemistry and reactivity.* Chemistry and reactivity ed. Sydney : Thomson Brooks/Cole.

Lehn, J., 1985. Supramolecular chemistry: receptors, catalysts, and carriers.. *Science,* Volume 227, p. 849.

Li, Z. T. & Wu, L. Z., 2015. *Hydrogen bonded supramolecular structures.* New York: Springer Heidelberg.

Li, Z. T. & Wu, L. Z., 2015. *Hydrogen Bonded Supramolecular Structures.* New York: Springer Heidelberg.

Lombard, J., Loots, L., le Roex, T. & Haynes, D. A., 2018. Formation of multi-component crystals with a series of pyridinium-carboxyacrylate zwitterions. *CrystEngComm,* Volume 20, p. 25–34.

Luceri, C. et al., 2007. *p*-Coumaric acid, a common dietary phenol, inhibits platelet activity in vitro and in vivo. *British Journal of Nutrition ,* 97(3), pp. 458-463.

MacGillivray, L. R. & Atwood, J. L., 1997. Nature. Volume 389, p. 469.

Maitland, G. C., Rigby, E. B., Smith, E. B. & Wakeham, W. A., 1981. *Intermolecular forces: Their origin and determination.* Oxford: Oxford University Press.

Markov, I., 2016. *Crystal growth for beginners: Fundamental of nucleation crystal growth and epitaxy..* 3rd ed. New Jersey: World Scientific.

McKinnon, J., Spackman, M. & Mitchell, A., 2004. Novel tools for visualizing and exploring intermolecular interactions in molecular crystals. *Acta Cryst,* Volume 60, p. 627–668.

Mirzaei, M. et al., 2018. Investigation of non-covalent and hydrogen bonding interactions on the formation of crystalline networks and supramolecular synthons of a series of a-aminophosphonates: Crystallography and DFT studies. *Elsevier,* Volume 1163, pp. 316 - 326.

Moulton, B. & Zaworotko, M., 2001. From molecules to crystal engineering: supramolecular isomerism and polymorphism in network solids. *Chemical Reviews,* Volume 101(6), p. 1629–1658.

Nangia, A. & Desiraju, G., 1998. *Supramolecular synthons and pattern recognition.* Berlin: Springer Berlin Heidelberg.

Novoa, J., 2018. *Intermolecular interactions in crystals: fundamentals of crystal engineering.* s.l.:The Royal Society of Chemistry .

Novoa, J., Braga, D. & Addadi, L., 2007. *Engineering of Crystalline Materials Properties: State of the Art in modeling, design, and applications.* Dordrecht: Springer.

Palmer, L. C. & Stupp, S. I., 2008. Molecular self-assembly into one-dimensional nanostructures. *Accounts of chemical research,* Volume 41, pp. 1674-1684.

Pedersen, C. J., 1967. *Chem. Soc.,* Volume 89, p. 7017.

Pihko, P. M., 2009. *Hydrogen Bonding in Organic Synthesis.* Weinheim: Wiley-VCH Verlag GmbH & Co. KGaA.

Sanphui, P., Goud, R., Khandavilli, R. & Nangia, A., 2011. Fast dissolving curcumin cocrystals. *Cryst. Growth Des,* Volume 11, pp. 4135-445.

Scheiner, S., 1997. *Hydrogen Bonding: A Theoretical Perspective.* New York: Oxford University Press.

Schneider, H., 2012. *Applications of supramolecular chemistry.* s.l.:CRC Press.

Seaton, C. C., 2011. Creating carboxylic acid co-crystals: The application of Hammett substitution constants. *CrystEngComm,* Volume 13, p. 6583–6592.

Seddon, K. R. & Zawortko, M., 1999. *Crystal Engineering: the design and application of functional solid.* Dordrecht: Kluwer Academic.

Spackman, M. & Jayatilaka, D., 2009. Hirshfeld Surface Analysis. *CrystEngComm,* Volume 11, pp. 19-32.

Steed, J. W. & Atwood, J. L., 2009. *Supramolecular Chemistry.* s.l.:John Wiley & Sons.

Stupp, S. I. & Palmer, L. C., 2013. Supramolecular chemistry and self-assembly in organic material design. *Chemistry of Materials,* Volume 26, pp. 507-518.

Tiekink, E. R., Vital, J. & Zaworotko, M., 2010. *Organic Crystal engineering:Frontiers in crystal engineering.* 1st ed. Chichester: John Wiley & Sons.

Turner, M. J. et al., 2017. *CrystalExplorer.* s.l.:The University of Western Australia.

Warren, B. E., 1990. *X-ray diffraction.* 1st ed. New York: Addison-Wesley PuB.

William, C., 2015. *X-ray Crystallography.* 2nd ed. New York: Oxford University Press .

William, J., 2017. *Crystal Engineering: How molecules build solids.* California: Morgan & Claypool.

Wolff, S. et al., 2012. Crystal Explorer. *Portuguese Chemical Society,* pp. 35-419.

Woolfson, M. M., 1997. *An introduction to X-ray crystallography.* 2nd ed. New York: Press Syndicate of the University of Cambridge .

CHAPTER 2: METHODOLOGY

2.1 Material used

Two compounds were used as target materials in the formation of new crystal structures. Their properties are listed in Table 2.1. Several groups of compounds were selected as co-formers based on their ability to hydrogen bond with the acids although only amines (pyridine and some of its derivatives) and 1,4-dioxane were successful in forming new solid forms. Table 2.2 summarises the properties of co-formers that successfully formed new compounds with the target acids in this study. Solvents were selected based on their ability to dissolve the solids or solid mixtures. All the multicomponent crystals were obtained using the slow evaporation method from mixtures of solvents in a specific volume to volume ratio. Table 2.3 summarises the properties of the solvents.

Table 2.1: Physical properties and pK$_a$ of the starting materials used in this study

Compounds	Molecular formula	Molecular weight (g mol^{-1})	Melting point (°C)	pK$_a$
p-coumaric acid	C$_9$H$_8$O$_3$	164.05	210-214	4.01
trans-ferulic acid	C$_{10}$H$_{10}$O$_4$	194.18	168-172	4.61

Table 2.2: Physical properties and pK$_a$ of co-formers used in this study

Compounds	Molecular formula	Molecular weight (g mol^{-1})	Melting point (°C)	Boiling point (°C)	pK$_a$
1,4-dioxane	C$_4$H$_8$O$_2$	88.11	-	101	-
2-amino-4-picoline	C$_6$H$_8$N$_2$	108.14	100	-	7.62
2-amino-6-picoline	C$_6$H$_8$N$_2$	108.14	40-44	-	7.60
4,4'-bipyridine	C$_{10}$H$_8$N$_2$	156.19	114	-	4.44, 5.25
pyridine	C$_5$H$_5$N	79.1	-	115	5.12

Table 2.3: Physical properties and pK$_a$ of solvents used in this study

Compounds	Acronyms	Molecular formula	Molecular weight (g mol^{-1})	Boiling point (°C)	pK$_a$
1,2-dichloroethane	DCE	C$_2$H$_4$Cl$_2$	98.96	83.47	-
Dimethyl sulfoxide	DMSO	C$_2$H$_6$OS	78.13	189	-
Ethanol	ETOH	C$_2$H$_5$OH	46.07	78.37	15.9
Ether	PET	C$_6$H$_{14}$	86.18	42-62	-
Ethyl acetate	ETOAC	C$_4$H$_8$O$_2$	88.11	83.47	25
Methanol	MeOH	CH$_3$OH	32.02	64.7	15.5
Propanol	PrOH	C$_4$H$_8$O	60.09	97	-1.99

2.2 Techniques

 The following techniques were used in this study:

- Crystallisation
- Thermal analysis
- X-ray diffraction
- Structure determination with suitable software programs

2.2.1 Crystallisation

Crystallisation is a process where molecules assemble themselves or ions add in their position in the crystal lattice forming a larger molecule. The principal crystallisation processes are nucleation and crystal growth (Pamplin, 1980).

Nucleation is the process where molecules gather into clusters and those molecules redissolve when they are unstable. In crystal growth, both nucleation and crystal growth continue simultaneously with supersaturation being the driving force of the process.

In this study slow evaporation and solvent assisted grinding techniques were used to prepare the multicomponent crystals.

2.2.1.1 Slow evaporation

The new solid forms (salt/co-crystal) were obtained by dissolving the target compound and co-former in a solvent mixture (1:1 molar ratio). For solvates, the target molecule was dissolved in the selected solvent followed by gentle heating on the hot plate and stirring until the solution

became clear. At times, co-solvents were used when incomplete dissolution of the mixture was observed. The co-solvent was selected based on their ability to completely dissolve the solid mixture. The solvent was left to evaporate slowly at ambient temperature and crystals were observed after a few weeks or months.

2.2.1.2 Solvent-assisted grinding

In case of salts/co-crystals, the target compound was ground in an equimolar stoichiometric ratio with the co-former with a maximum of three drops of the solvent/solvent mixture. In the case of the solvate, the target molecule was only ground with the solvent/solvent mixture.
The mixtures were manually ground for 25 to 30 minutes using a mortar and pestle.

2.2.2 Thermal analysis

Thermal analysis is a branch of material science which focuses on studying the thermal properties of materials (Wunderlich, 2001). The measurement is often done by increasing the temperature at a constant rate and there is also the possibility of doing it isothermally (Speyer, 1994). Two thermal techniques were used in this study, specifically differential scanning calorimetry (DSC) and thermal gravimetric analysis (TGA). Table 2.4 provides the parameters of different thermal analysis instruments used in the study.

2.2.2.1 Differential scanning calorimetry

Differential scanning calorimetry is a calorimetric technique that deals with energy differences. DSC comprises measurements of the difference in power requirements between a sample and reference maintained at the same temperature as the sample while both are subjected to a heating program (Höhne, *et al*., 2003). It is sensitive in terms of phase changes that do not result in changes in mass (e.g. melting point) and the integration of the peak area gives quantitative measurements of the enthalpy change, ΔH, associated with the process being studied (Liddington & Bobkov, 2009). If the sample is undergoing a phase change that is endothermic, such as melting, more power will be required in the sample chamber compared to the reference. This will result in a positive peak in the DSC trace. Similarly, exothermic processes result in negative peaks, while a flat trace implies no difference between the behaviour of the sample and reference (Chiavaro, 2015). Measurements were performed on a Perkin Elmer, Pyris 6000 DSC instrument using aluminium pans in a nitrogen atmosphere at a flow rate of 20 mL min^{-1}. The scans were

recorded between 30 to 300 °C at a constant heating rate of 10 Kmin^{-1}. Sample masses, not exceeding 5 mg, were measured into aluminium pans which were crimped prior to analysis.

2.2.2.2 Thermal gravimetric analysis (TGA)

Thermal gravimetric analysis measures the sample weight as a function of increasing temperature or time (Vyazovkin, *et al*., 2018). The sample mass is expressed as a percentage weight of the initial mass, resulting in a trace that exhibits one or more plateaus separated by slopes corresponding to the loss of volatile liquid co-formers at various temperatures (Gabbott, 2008). If the formula mass of the target molecule and co-former is known, then the ratio may be obtained by comparison of calculated and observed weight loss for various stoichiometries (Sepe, 1997). These compounds are often non-stoichiometric and the TG results can be utilised in the assignment of site occupancy factors in the crystal structure (Brown, 1988).

Measurements were performed on a Perkin Elmer, Pyris 6 TGA instrument. The scans were recorded between 30 and 300 ºC at a constant heating rate of 10 Kmin^{-1}. Samples with masses between 2 and 5 mg were analysed using an open ceramic crucible. The % weight loss was calculated using the Pyris 1 software.

Table 2.4: Thermal analysis parameters

DSC and TGA	
Model	Perkin-Elmer DSC Pyris 6000 and TGA 6 System
Purge gas	Nitrogen gas @ 20 mLmin^{-1}
Temperature program	303-573 @ 10 Kmin^{-1}

2.2.3 X-ray diffraction

X-ray diffraction is an analytical technique that relies on the dual wave/particle nature of X-rays to obtain atomic or molecular information of a crystal, in which the crystalline structure diffracts the beam of incident X-rays into many specific directions (Suryanarayana & Norton, 1998). A primary use of the technique is the identification and characterisation of compounds based on their diffraction pattern (Waseda, *et al*., 2011).

2.2.3.1 Powder X-ray diffraction

Powder X-ray diffraction is an analytical method used for the identification of crystalline phases and it also provides information regarding unit cell dimensions (Rissanen, 2014). The diffraction intensity is captured with a point or line detector and plotted in two dimensions as a function of 2θ. The phenomenon is based on interference between X-ray radiation and the crystalline material (Schalley, 2012).

The diffraction is described by Bragg's law:

$$n\lambda = 2d \sin \theta \qquad\qquad\qquad \text{(Eq. 2.1)}$$

θ: is the glancing angle between the X-ray beam and the plane of the crystal under irradiation.

d: is the distance between atomic layers in a crystal.

λ : is the wavelength of the incident X-ray beam

n: is the integer

Samples were powdered manually by grinding both the target compound and the co-former in a 1:1 molar ratio with solvent drops for a few minutes and the resulting powder was placed in a sample holder in the path of the X-ray beam. A D2 PHASER Bruker diffractometer with Cu-Kα radiation (1.54184 Å) was the instrument used in this study. The voltage tube and current were at 30 kV and 10 mA max, respectively with a scintillation counter, 1-dim LYNXEYE detector. The scanning range of each sample was between 4-50˚ 2θ.

The experimental powder patterns were compared to that of the starting material and to the calculated patterns (generated from the known structures) using LAZYPULVERIX (Yvon, *et al*., 1977).

2.2.3.2 Single crystal X-ray diffraction

Single crystal X-ray diffraction is one of the most definitive methods for elucidating the crystal structures of compounds as it gives a detailed picture of the molecular and crystal structure at atomic levels (Clegg, *et al*., 2001). The unit cell dimensions, bond-length, bond-angles and details of site-ordering of crystalline materials can be obtained with the technique. X-ray

diffraction has four major steps: crystallisation, data collection, structure solution, and refinement (Datta & Grant, 2004).

Diffraction data for all compounds were collected on a Bruker APEX II diffractometer with a graphite-monochromated MoK$_\alpha$ = 0.71073 Å at 173 K using an Oxford Cryostream 700 (Bruker, 2005).

SHELXS-97 (Sheldrick, 1997) was the computer program used to solve structures and the graphical user interface was X-seed (Barbour, 2001). The space group was determined by using the collected intensities and pre-determined cell parameters as inputs to the program XPREP (Bruker, 1997). SHELXL-97 was used for the refinement of the structures and uses full-matrix least-squares against F^2 for unique reflections.

$$\sum w \, (F_0^2 - kF_C^2)^2 \qquad \text{(Eq. 2.2)}$$

The agreement between the observed structure factors (F_o) and the calculated structure factors (F_c) were monitored by assessing the residual index R. The indirect measurement of the accuracy of the structure is the residual R which must be low in value if the model is satisfactory.
The residual index R_1 is the agreement between the observed and calculated structure factors based on F ($Eq.\,2.3$) while the residual index wR is the agreement based on F^2 (Eq. 2.4).

$$R_1 = \frac{\sum \lVert F_0 \rvert - \lvert F_c \rVert}{\sum \lvert F_o \rvert} \qquad \text{(Eq. 2.3)}$$

$$w\mathrm{R} = \left[\frac{\sum w(F_o^2 - F_c^2)^2}{\sum w(F_o^2)^2} \right]^{1/2} \qquad \text{(Eq. 2.4)}$$

Where w is the weight allocated to the structure factor during the refinement.

$$w = \frac{1}{\sigma^2(F_o^2) + (aP)^2 + bP} \qquad \text{(Eq. 2.5)}$$

Where $\quad P = \frac{\max(0, F_o^2) + 2F_c^2}{3} \qquad \text{(Eq. 2.6)}$

while a and b were also refined for each structure. The Goodness of Fit (S) was obtained for all the structures and is dependent on F^2 ($see\ Eq.\ 2.7$)

$$S= \left[\frac{W(|F_O|^2-|F_c|^2)^2}{(N-n_p)}\right]^{1/2}$$

(Eq. 2.7)

where N is the number of reflections and n_p is the total number of parameters refined. X-ray powder patterns were calculated using LAZY PULVERIX and compared to experimental powder patterns for crystallisation. All crystal packing diagrams were generated with POV-RAY (Cason, 2004). The program LAYER was utilized to test systematic absences and space group symmetry (Barbour, 1999).

2.2.4 Fourier transform infrared (FTIR) spectroscopy

FTIR spectroscopy is an analytical technique that relies on the fact that most molecules absorb light in the infra-red region of the electromagnetic spectrum (Larkin, 2011). This absorption corresponds specifically to the bonds present in the molecule (Smith, 1996). For the molecular characterisation of compounds, the spectra were collected using a Perkin Elmer Spectrum Two FTIR spectrometer. About 2 mg of sample was weighed, crushed and placed on the crystal. The dice was rolled down until the gauge reached 49. The frequency range is measured as wave numbers typically over the range 4000 – 600 cm^{-1}.

2.3 References

Barbour, L. J., 1999. LAYER. *J. Appl. Cryst,* Volume 32, p. 351.

Barbour, L. J., 2001. X-Seed-A Software Tool for Supramolecular Crystallography. *J. Supramol. Chem 1,* p. 189–191.

Brown, M., 1988. *Introduction to thermal analysis.* London : Chapman and Hall.

Bruker, 1997. *XPREP: Data preparation and reciprocal space exploration.*

Bruker, 2005. *APEX2. Version 1.0-27. Bruker AXS Inc,* Madison, Wisconsin.

Buckton, G., 2007. *Solid-state properties, Aulton's pharmaceutics, the science of dosage form design, Aulton M.E.* 3rd ed. London: Churchill Livingstone.

Cason, C. J., 2004. POV-RAY for Windows Persistence of Vision. *Raytracer Pty. Ltd, Victoria, Australia. URL: http://www.povray.org.*

Chiavaro, E., 2015. *Differential scanning calorimetry: Applications in fat and oil technology.* New York: CRC press.

Clegg, W., Blake, A., Gould, R. & Main, P., 2001. *Crystal structure analysis : Principles and practice.* Chester: Oxford University Press.

Datta, S. & Grant, J., 2004. *Crystal structure of drugs: Advances in determination, prediction and engineering.* s.l.:Nature Reviews Drug Discovery.

Gabbott, P., 2008. *Principles and applications of thermal analysis.* Oxford: Blackwell.

Höhne, G., Hemminger, W. & Flammersheim, H., 2003. *Differential Scanning Calorimetry.* 2nd ed. New York: Springer.

Larkin, P., 2011. *Infrared and raman spectroscopy: Principles and spectral interpretation.* San Diego: Elsevier.

Liddington, R. & Bobkov, A., 2009. *Differential scanning calorimetry : Protocol exchange.*

Pamplin, B., 1980. *Crystal growth: International series on the science of the solid state.* 2nd ed. London: Pergamon Press.

Rissanen, K., 2014. *X-ray crystallography : Encyclopedia of supramolecular chemistry.*

Schalley, C., 2012. *Analytical method in supramolecular chemistry.* 2nd ed. Berlin.

Sepe, M. P., 1997. *Thermal analysis of polymers.*Rapra.

Sheldrick, G. M. , 1997. Program for the Refinement of Crystal Structures from Diffraction Data. University of Göttingen, Göttingen, Germany.

Smith, B., 1996. *Fundamentals of fourier transform infrared spectroscopy.* New York: CRC Press.

Speyer, R., 1994. *Thermal analysis of materials.* New York: Marcel Dekker .

Suryanarayana, C. & Norton, M., 1998. *X-ray diffraction: A practical approach.* New York: Springer Science + Business Media.

Vyazovkin, S., Koga, N. & Schick, C., 2018. *Handbook of thermal analysis and calorimetry: Recent advances, techniques and applications.* 2nd ed. Amsterdam: Elsevier.

Waseda, Y., Matsubara, E. & Shinoda, K., 2011. *X-Ray diffraction crystallography: Introduction, examples and solved.* New York: Springer .

Wunderlich, B., 2001. *Encyclopedia of materials: Science and technology.* 2nd ed. Elsevier.

Yvon, K., Jeitschko, W. & Parthe, E. J., 1977. LAZY PULVERIX: a computer program for calculating X-ray and neutron diffraction powder patterns. *Cryst,* Volume 10, pp. 73-74.

CHAPTER 3: CO-CRYSTALS OF *p*-COUMARIC ACID AND *trans*- FERULIC ACID

3.1 Introduction

A co-crystal results when crystalline materials consisting of neutral molecules are mixed and the neutral molecules are held together by non-covalent interactions, mostly hydrogen bonding (Bevill, *et al*., 2014). 4,4'-bipyridine (BIPY) was selected due to its potential to hydrogen bond with both starting materials via O-H•••N interactions. The chemical structures used in this study are shown in Figure 3.1.

5 mg of the acid and BIPY (1:1 stoichiometric ratio) were dissolved in a vial containing a solvent mixture of 25:75 (v/v) of DMSO and propan-2-ol. The mixtures were stirred on a hot plate at 50 °C for 30 minutes until clear solutions were obtained. These solutions were left to evaporate at room temperature.

Both crystal structures were successfully solved in the monoclinic space group *P2₁/c.* *p*CA with BIPY resulted in a crystal structure with stoichiometry 3:3 (Z' = 3) and TFA with BIPY generated a 1:1 stoichiometry crystal structure (Z'=1). The C-O distances confirmed that there was no proton transferred. The observed intermolecular hydrogen bonds are O-H•••N and C-H•••O.
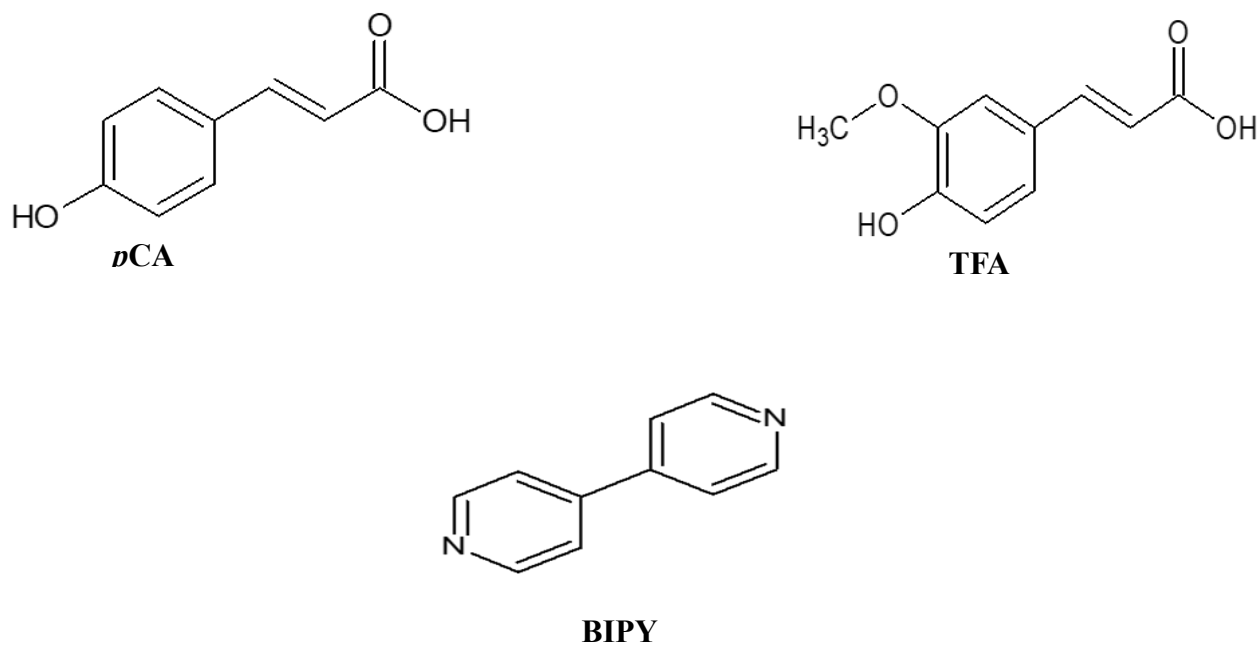
Figure 3.1: Chemical structures used in this study

3.2 Structural analysis of co-crystals of *p*-coumaric acid and *trans*-ferulic acid with 4,4'-bipyridine.

Both compounds formed block-like crystals with different colours. Yellow crystals were observed for the 3(*p*CA)•3(BIPY) co-crystals, whereas the TFA•BIPY formed colourless crystals. Both structures were solved using direct methods with SHELXS-97 (Sheldrick, 1997). The crystal data is summarised in Table 3.1.

Table 3.1: Crystal data and refinement parameters of 3(*p*CA)•3(BIPY) and TFA•BIPY

Compound	3(*p*CA) • 3(BIPY)	TFA•BIPY
Molecular formula	$C_{57}H_{48}N_6O_9$	$C_{20}H_{18}N_2O_4$
M_r (g/mol)	961.01	350.36
Temperature (K)	173	173
Crystal system	Monoclinic	Monoclinic
Space group	$P2_1/c$	$P2_1/c$
a (Å)	20.080(4)	6.4170(13)
b (Å)	11.977(2)	30.894(6)
c (Å)	20.687(4)	9.3866(19)
α (°)	90	90
β (°)	107.63(3)	109.86(3)
γ (°)	90	90
V (Å^3)	4741.5(16)	1750.2(6)
Z	4	4
ρ (calcd) (g/cm^3)	1.346	1.330
Absorption coefficient μ (mm^{-1})	0.092	0.094
$2\Theta_{max}$ (°)	56.5	56.6
Reflections collected	83238	12492
No. data with $I > 2\sigma(I)$	7614	3001
No. parameters	244	244
Final R ($I > 2\sigma(I)$)	R$_1$= 0.0509; wR$_2$= 0.1299	R$_1$= 0.0490; wR$_2$= 0.1315
R indices (all data)	R$_1$= 0.0876; wR$_2$= 0.1562	R$_1$= 0.0776; wR$_2$= 0.1557
Goodness-of-fit on F^2	1.011	0.916
Min, max e$^-$ density (e Å^{-3})	-0.347, 0.345	-0.252, 0.236

3.2.1 Co-crystal of *p*-coumaric acid with 4,4'-bipyridine

Yellow single crystals were obtained after a week of slow evaporation of 1:1 *p*CA and 4,4'-bipyridine (BIPY) in a solvent mixture of 25:75 (v/v) dimethyl sulfoxide and propan-2-ol at room temperature. The structure crystallised in the monoclinic space group $P2_1/c$. The asymmetric unit contains three molecules of *p*CA and three molecules of BIPY, Figure 3.2. No proton transfer was observed as predicted by the difference in pK_a between *p*CA and BIPY (1.24) that falls in the region where co-crystals are most likely to occur (Cruz-Cabeza, 2012). Thus, the 3(*p*CA)•3(BIPY) co-crystal is obtained.
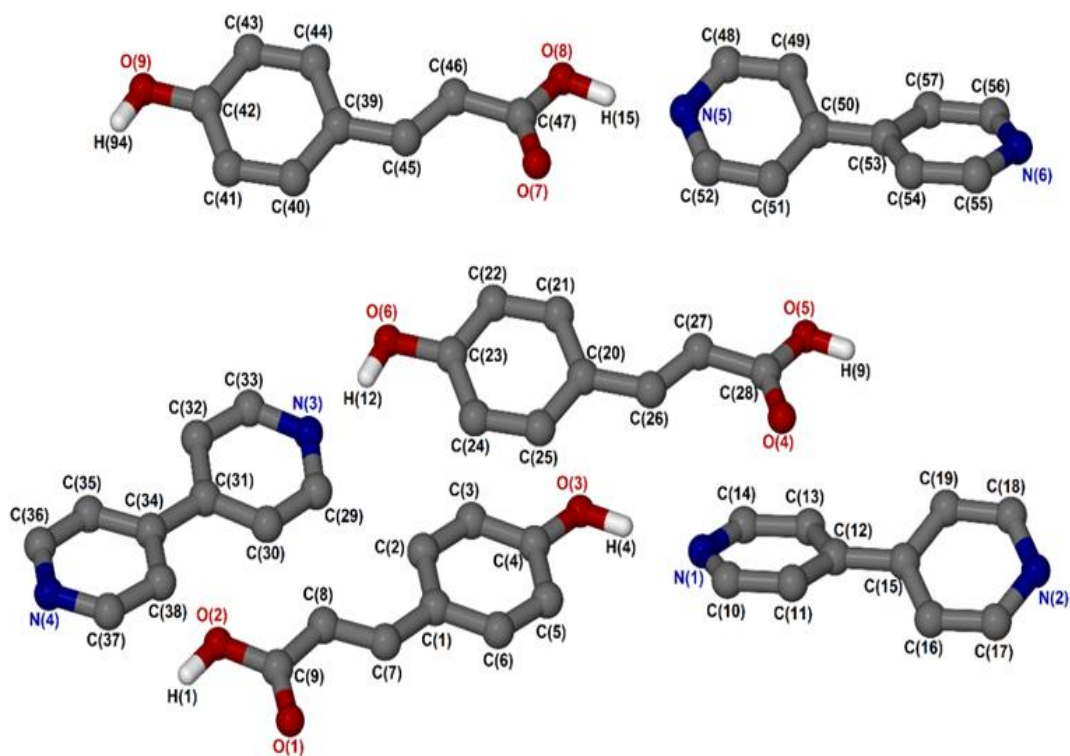
Figure 3.2: Asymmetric unit of 3(*p*CA)•3(BIPY) co-crystal with some hydrogen atoms omitted for clarity

The structure is characterised by O-H•••N interactions (Figure 3.3). There are also some weak C-H•••O hydrogen bonds, summarised in Table 3.2. The pyridine rings of BIPY are not co-planar with dihedral angles of 9.88°, 26.8° and 31.34°. Each BIPY molecule is hydrogen bonded to two *p*CA molecules. The hydrogen bonded units are packed into continuous parallel ribbon

layers, see Figure 3.4. The O-H•••N hydrogen bonding in the packing diagram forms waves that can be described as $C_2^2(19)$ chains (Etter, *et al.*, 1990).
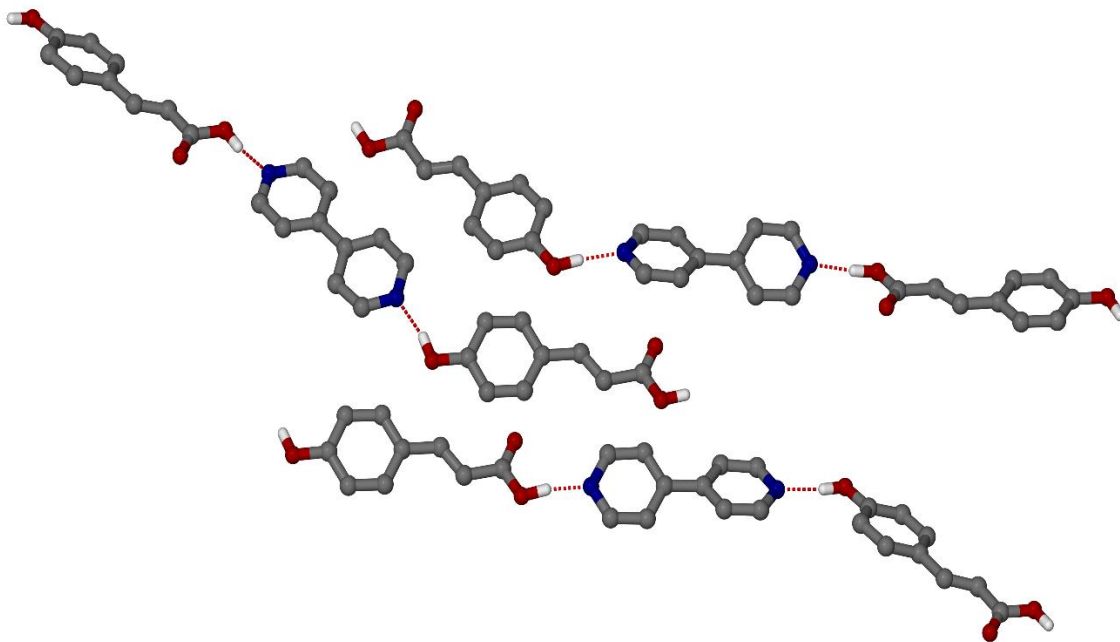
Figure 3.3: Hydrogen bonds of 3(*p*CA)•3(BIPY) co-crystal with some hydrogen atoms omitted for clarity.

Table 3.2: Geometrical data for hydrogen bond of 3(*p*CA)•3(BIPY)

	D-H (Å)	H•••A (Å)	D•••A (Å)	<DHA (º)	Symmetry operations
O3-H4•••N1	0.97(2)	1.78(3)	2.745(2)	172(2)	
O6-H12•••N3	0.90(2)	1.82(2)	2.710(2)	168(2)	
O8-H15•••N5	0.96(2)	1.72(2)	2.678(2)	171(2)	
O9-H94•••N6	0.91(2)	1.82(2)	2.718(2)	169(2)	x-1, -y+½, z-½
O5-H9•••N4	0.93(2)	1.76(2)	2.675(2)	170(2)	x+1, -y+½, z+½
O2-H1•••N2	0.94(2)	1.74(3)	2.674(2)	172(2)	x-1, -y-½, z-½
C54-H54•••O7	0.95	2.80	3.318(2)	115.3	-x+1, -y, -z+1
C55-H55•••O7	0.95	2.43	3.154(2)	132.9	-x+1, -y, -z+1
C13-H13•••O4	0.95	2.80	3.347(2)	117.6	
C14-H14•••O4	0.95	2.56	3.248(2)	129.2	
C25-H25•••O3	0.95	2.75	3.510(2)	137.6	
C38-H38•••O2	0.95	3.16	3.650(2)	113.8	
C37-H37•••O2	0.95	2.85	3.506(3)	126.8	
C48-H48•••O8	0.95	2.73	3.346(2)	123.2	-x+1, -y+1, -z+1
C49-H49•••O8	0.95	2.94	3.441(2)	114.2	-x+1, -y+1, -z+1
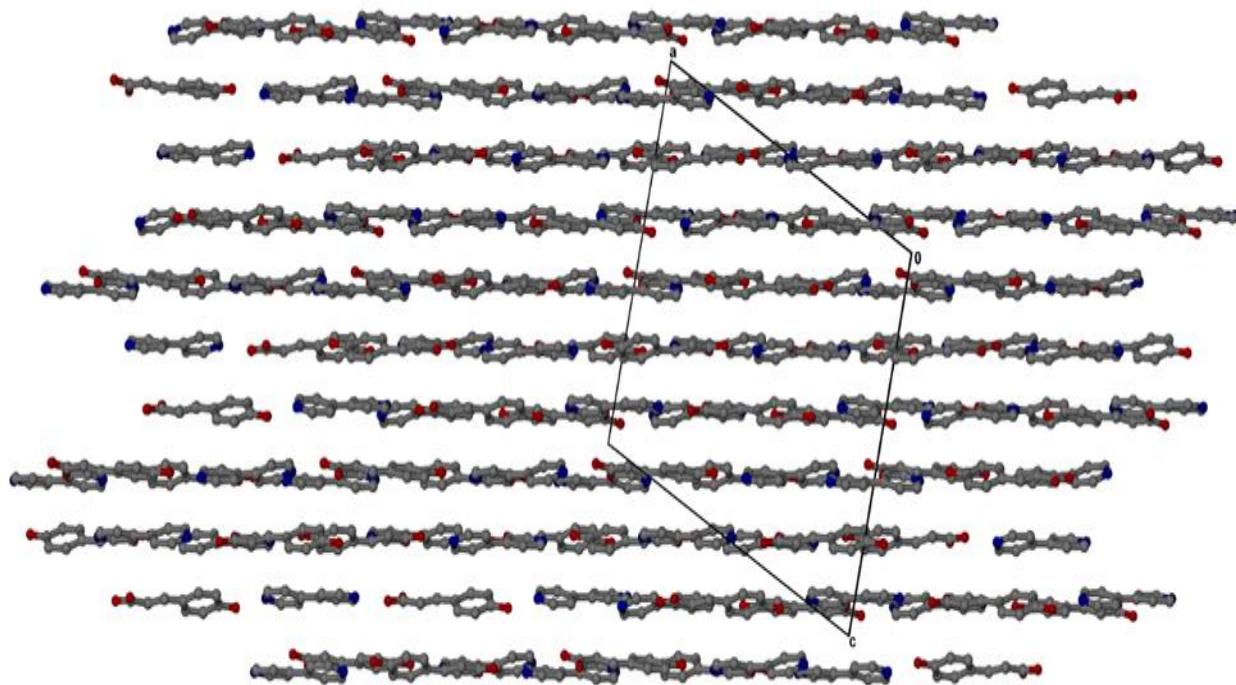
Figure 3.4: Packing diagram of 3(*p*CA)•3(BIPY) along [010]

3.2.2 Co-crystal of *trans*-ferulic acid with 4,4'-bipyridine

A 1:1 ratio of TFA and BIPY was dissolved in a solvent mixture of 25:75(v/v) of dimethyl sulfoxide and propan-2-ol in a vial which was left to evaporate at room temperature. Clear single crystals were obtained after five days. The asymmetric unit consisting of one molecule of TFA and one of BIPY is shown in Figure 3.5.
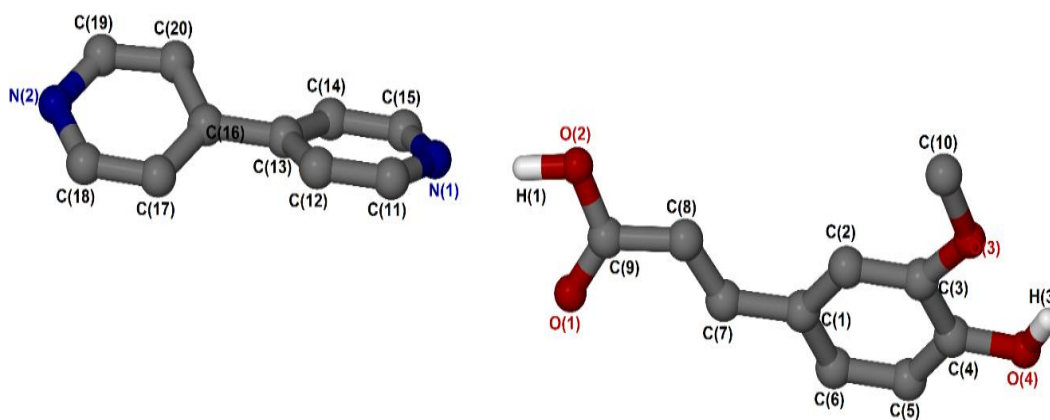
Figure 3.5: Asymmetric unit of TFA•BIPY with only hydrogen atoms involved in hydrogen bonding shown for clarity.

The same types of intermolecular interactions (O-H•••N) found in the previous crystal structure are also displayed in this supermolecule complex, Figure 3.6. The OH group of the carboxylic acid in TFA is hydrogen bonded to the pyridine of BIPY, d(O2-N1) = 2.6657 Å. The hydroxyl group of the TFA molecule is also hydrogen bonded to the same BIPY molecule, d(O4-N2) = 2.8304 Å. The TFA•BIPY packing diagram has a continuous wave shape (Figure 3.7), allowing the carbonyl oxygen of the TFA molecule to point toward C6 and C7 of another TFA molecule, thus resulting in weak hydrogen bonds, d(C6-O1) = 3.422 Å and d(C7-O1) = 2.849 Å. The packing diagram is also sustained by π•••π stacking with d(Cg-Cg) = 4.217 Å and C-H•••π; d(C17•••π) = 3.453 Å and d(C10•••π) = 3.675 Å. It is also observed that the O-H•••N hydrogen

bonding in the packing diagram forms wave-like $C_2^2(19)$ chains. The hydrogen bonds are summarised in Table 3.3. The dihedral angle between the pyridine rings of BIPY is 30.60 º.
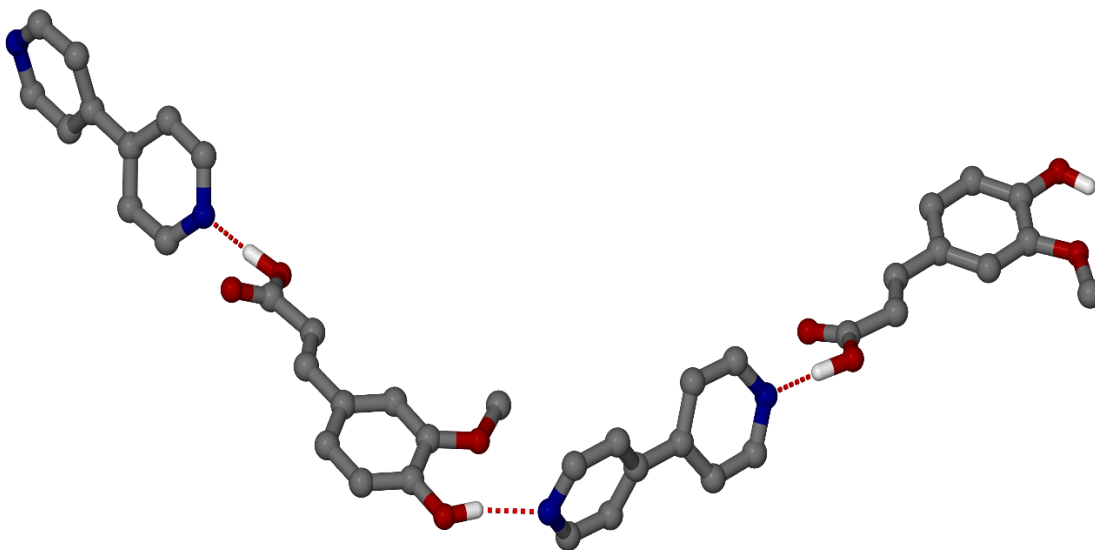
Figure 3.6: Hydrogen bonding of TFA•BIPY with hydrogen atoms not involved in hydrogen bonding omitted.

Table 3.3: Geometrical data for hydrogen bond of TFA•BIPY

	D-H (Å)	H•••A (Å)	D•••A (Å)	<DHA (º)	Symmetry operation
O2-H1•••N1	1.01(3)	1.66(3)	2.666(2)	173(2)	
O4-H3•••N2	0.89(3)	1.96(3)	2.830(2)	164(2)	-x-2, y+½, -z+½
C7-H7•••O1	0.95	2.52	2.849(2)	101	x, y, z
C6-H6•••O1	0.95	2.63	3.422(2)	141	-x-1, -y, -z+1
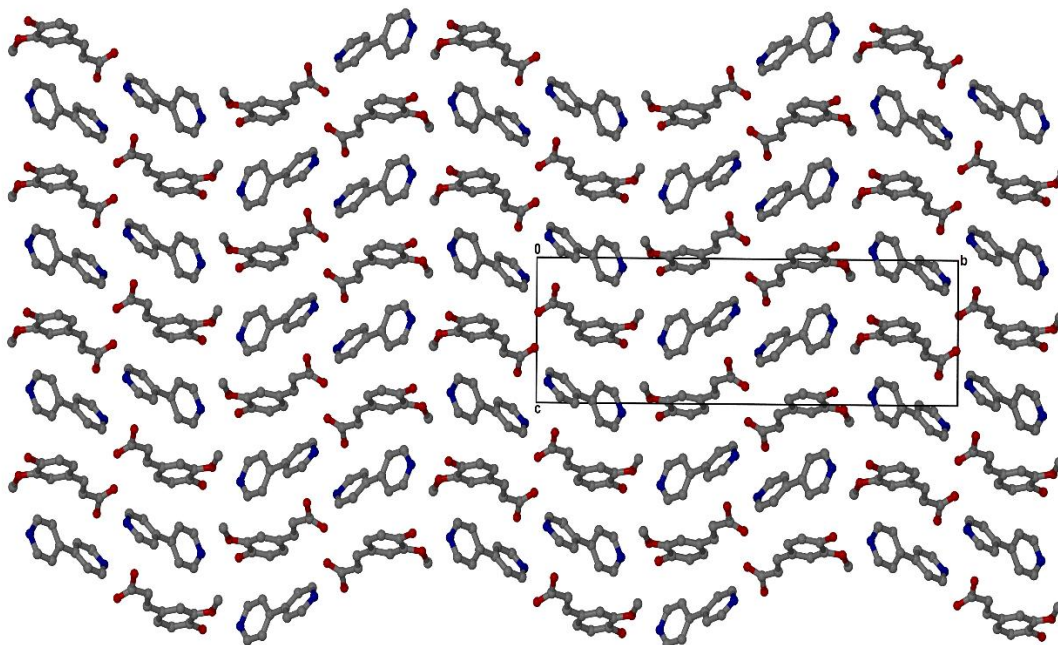
Figure 3.7: Packing diagram of TFA•BIPY (hydrogen atoms have been excluded for clarity) down [100]

3.3 Torsion angles

Two torsion angles were considered in the conformation of *p*CA and TFA (Figure 3.8). 3(*p*CA)•3(BIPY) has a Z'= 3 compared to that of TFA•BIPY with a Z' = 1. The three different molecules of *p*CA in the asymmetric unit have slightly different conformations. Two of the *p*CA molecules have the twisting of the carboxylic acid group, τ'_2 = -10.7° and τ''_2 = -11.7° very close to that of TFA, τ_2 = 10.1°, whereas the third molecule of *p*CA has a carboxylic acid group twisting torsion angle that is slightly less (1.3°). The freedom of rotation involving the twisting of the ring (τ_1 = 12.8°) for the TFA molecule is higher compared to the *p*CA molecules (τ_1 = -3.7°, τ'_1 = -7.1°, τ''_1 = -6.1°). Table 3.4 summarizes the torsion angles of 3(*p*CA)•3(BIPY) and TFA•BIPY.
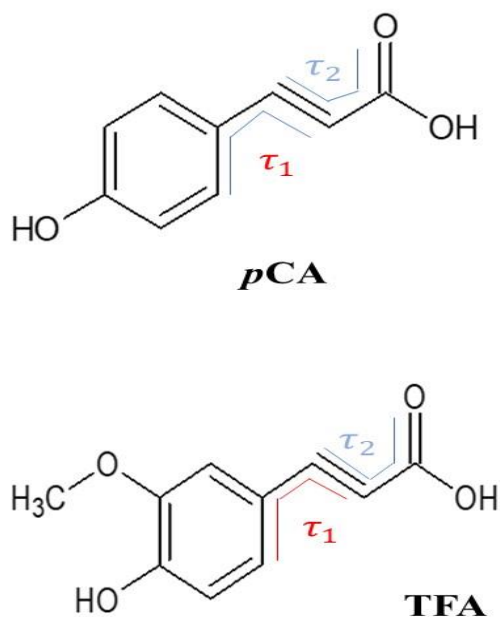
Figure 3.8: Torsion angles of *p*CA and TFA

Table 3.4: Torsion angles of 3(*p*CA)•3(BIPY) and TFA•BIPY

	TFA•BIPY	3(*p*CA) • 3(BIPY)
Torsion angle	(°)	(°)
τ_1(C2-C1-C7-C8)	12.8	3.7
τ'_1(C21-C20-C26-C27)	-	7.1
τ''_1(C44-C39-C45-C46)	-	6.1
τ_2(C7-C8-C9-O1)	10.1	1.3
τ'_2(C26-C27-C28-O4)	-	10.7
τ''_2(C45-C46-C47-O7)	-	11.7

3.4 Hirshfeld surface analysis of 3(*p*CA)•3(BIPY) and TFA•BIPY co-crystals

Hirshfeld surface (McKinnon, *et al*., 2007) analysis was used to examine the strength and role of hydrogen bonds and other intermolecular forces and to estimate their importance in the crystal lattice stability (Spackman & McKinnon, 2002). The characteristic features in the fingerprint plots show that the crystal packing for both co-crystals are dominated by H•••H, O•••H and C•••H contacts. The *p*CA and TFA molecules both have C•••H contacts that result in an asymmetric pair of wings (Figure 3.9b for *p*CA and 3.10b for TFA) and H•••H contacts appear as scattered points along a broad peak in the middle of the region of the fingerprint plot (Figure 3.9d, 3.10d and 3.11d for *p*CA and Figure 3.12d for TFA). There is a slight difference in their percentage contributions. The O•••H contacts which is attributed to C-H•••O hydrogen bond interactions, also occur as a pair of asymmetric wings for both co-crystals. The O•••H percentage contribution in the crystal packing of the three molecules of *p*CA in 3(*p*CA)•3(BIPY) are 26.7, 22.5 and 25.8 % (Figure 3.9f, 3.10f and 3.11f respectively) and that of TFA in TFA•BIPY is 26.5 %, Figure 3.12f. The N•••H contacts (Figure 3.9e, 3.10e, 3.11e for *p*CA and 3.12e for TFA) appear as a long sharp spike on the top left side of the fingerprint plot and it is attributed to the O-H•••N hydrogen bond, which is a moderate hydrogen bond interaction. The N•••H contribution for the three molecules of *p*CA in 3(*p*CA)•3(BIPY) are 7.5, 7.8 and 7.4 % respectively while that for the TFA molecule in the crystal packing is 7.4 %. Figure 3.9b, 3.10b and 3.11 for *p*CA and Figure 3.12b for TFA, concern the relative areas associated with C•••C contacts (often referred to as π•••π contacts) and associated with the planar stacking arrangement. 6.6 % of the surface can be identified as C•••C for all the molecules of *p*CA in 3(*p*CA)•3(BIPY) co-crystal and in TFA•BIPY a negligible amount (0.1 %) is identified as C•••C for the molecules of TFA. Table 3.5 summarises the various quantitative interactions for both co-crystals.
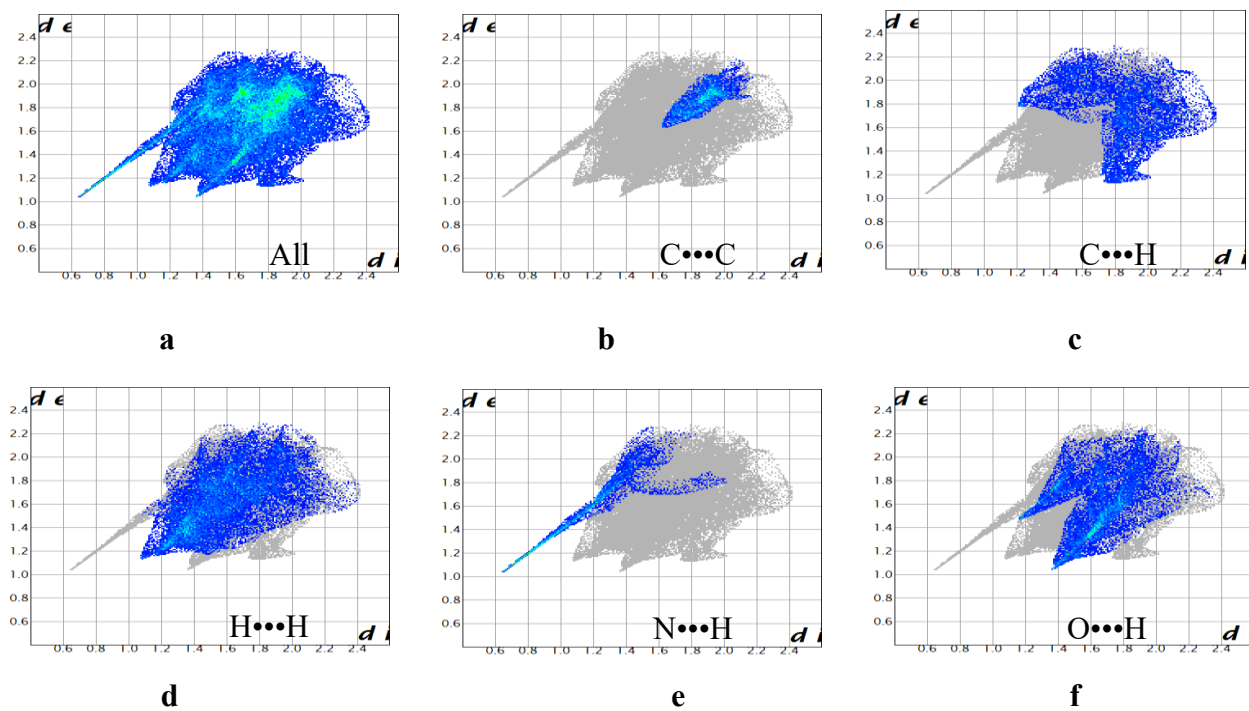
Figure 3.9: Fingerprint plot of *p*CA in the 3(*p*CA)•3(BIPY) co-crystal
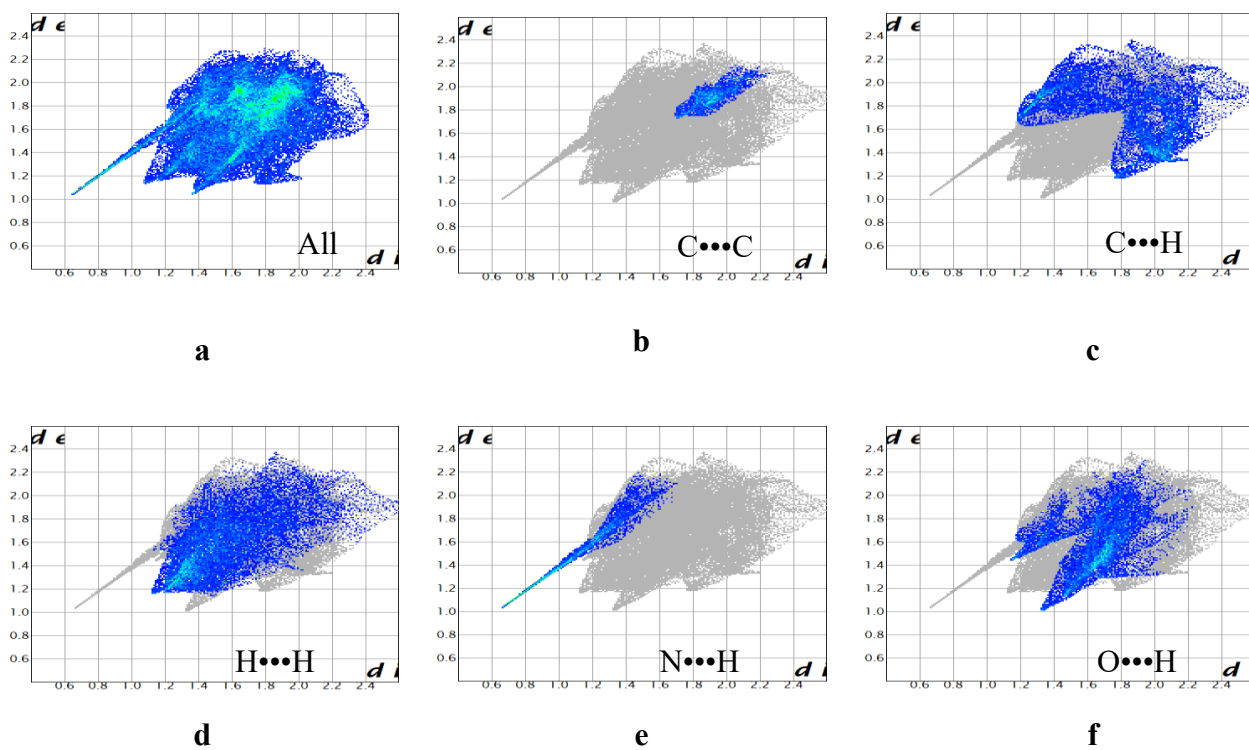
Figure 3.10: Fingerprint plot of *p*CA′ in the 3(*p*CA)•3(BIPY) co-crystal
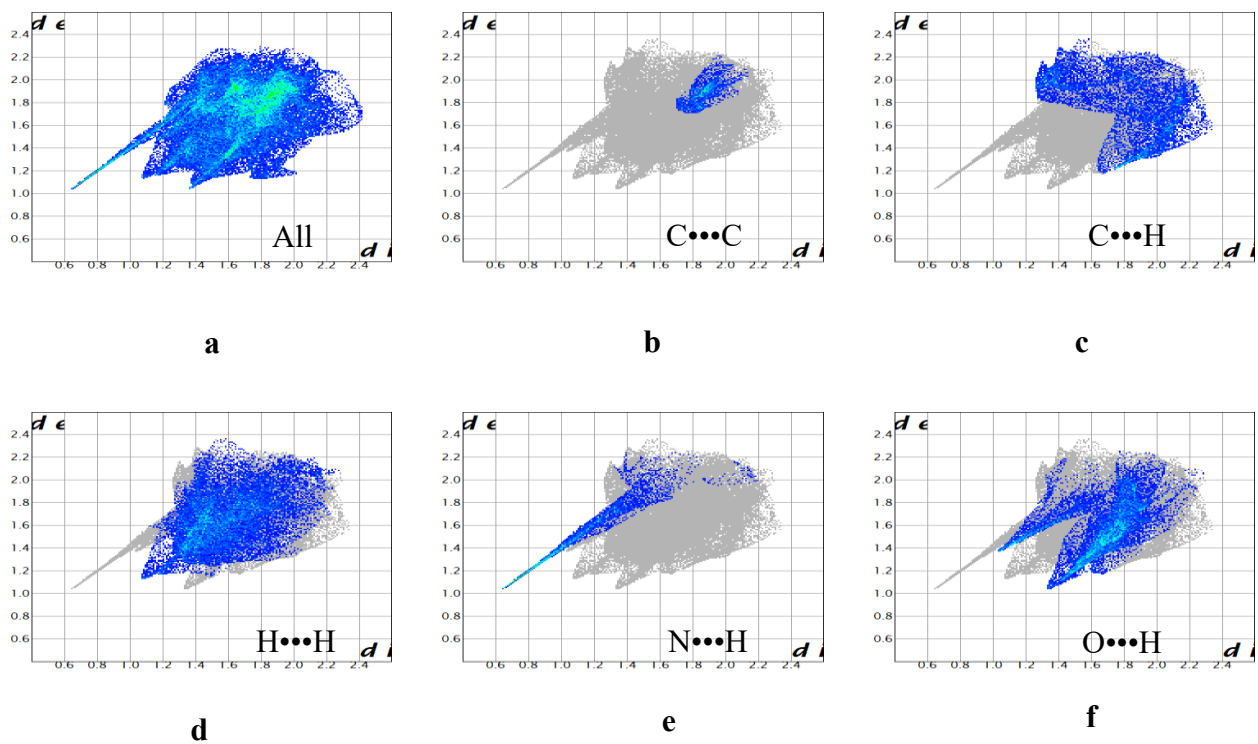
Figure 3.11: Fingerprint plot of *p*CA″ in the 3(*p*CA)•3(BIPY) co-crystal
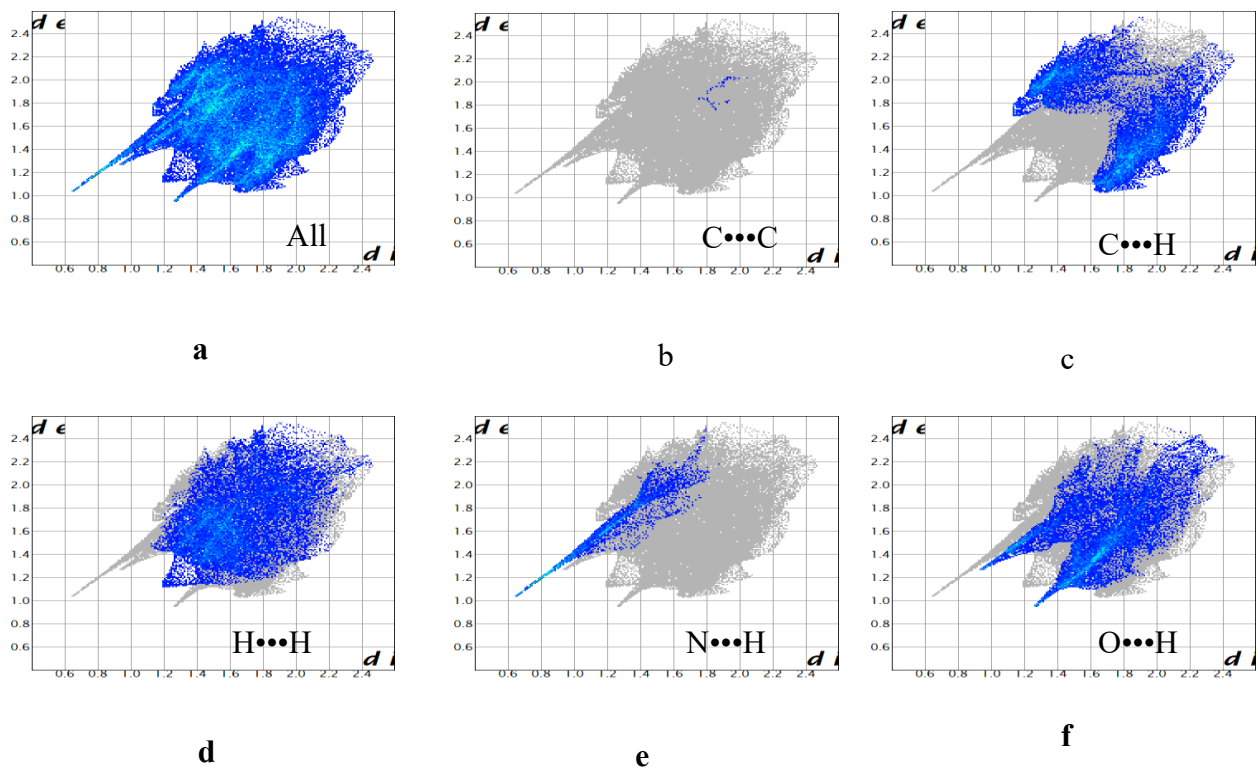
Figure 3.12: Fingerprint plot of TFA in TFA•BIPY

Table 3.5: Quantitative summary of various interactions of *p*CA and TFA co-crystals

Compounds	C•••C (%)	C•••H (%)	H•••H (%)	N•••H (%)	O•••H (%)
3(*p*CA)•3(BIPY)	8.8	17.4	34.6	7.5	26.7
3(*p*CA)•3(BIPY)′	6.4	26.0	31.9	7.8	22.5
3(*p*CA)•3(BIPY)″	4.6	19.9	35.8	7.4	25.8
TFA•BIPY	0.1	29.4	33.1	7.4	26.5

3.5 Thermal analysis

The DSC curve of 3(*p*CA)•3(BIPY) shows one broad endothermic peak, depicting the melting point of the crystal at 194.5 °C. The melting of the crystal is in between the melting point of the two starting materials, BIPY at 133 °C and *p*CA at 216 °C (Figure 3.13). It is also observed that the DSC curve of TFA•BIPY (Figure 3.14) shows one endothermic peak at 202.5 °C corresponding to the melt of the TFA•BIPY co-crystal. The co-crystal melt is found to be higher than the melting point of both starting materials, TFA (174 $^{\circ}$C) and BIPY (133 $^{\circ}$C). Based on the melting point of both co-crystals, TFA•BIPY is more stable compared to 3(*p*CA)•3(BIPY). This can be correlated to the higher percentage of C•••H contacts in TFA•BIPY and the slightly elevated O•••H interactions due to the presence of the methoxy group.
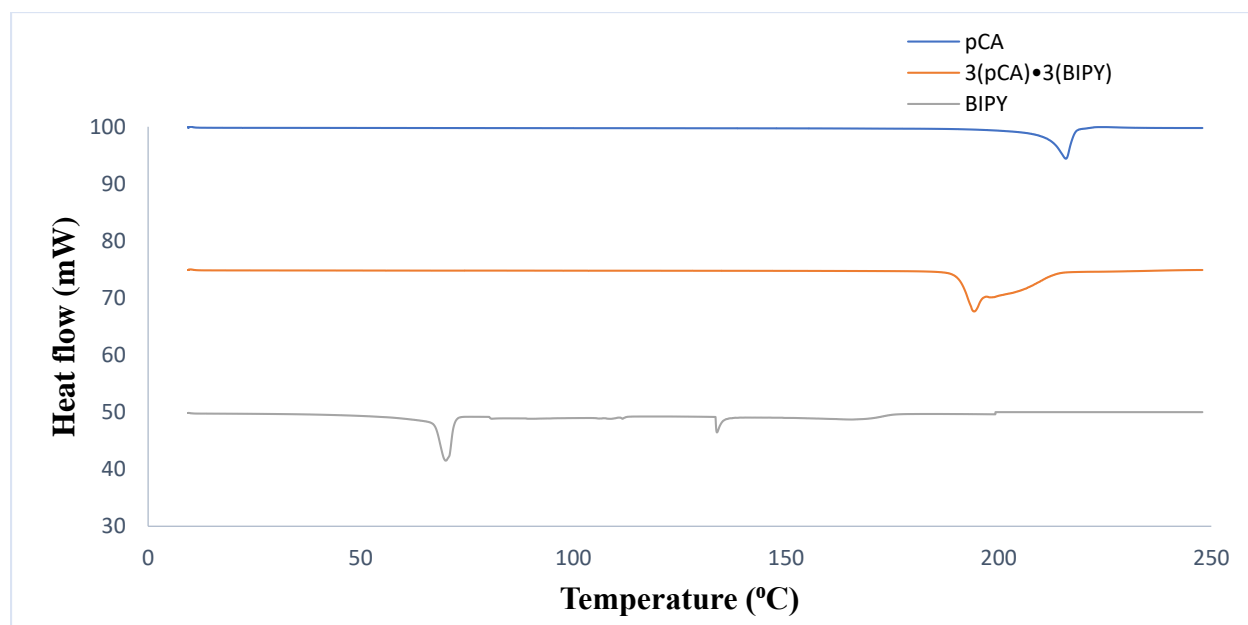
Figure 3.13: DSC curves of *p*CA (blue), BIPY (grey) and 3(*p*CA)•3(BIPY) (orange)
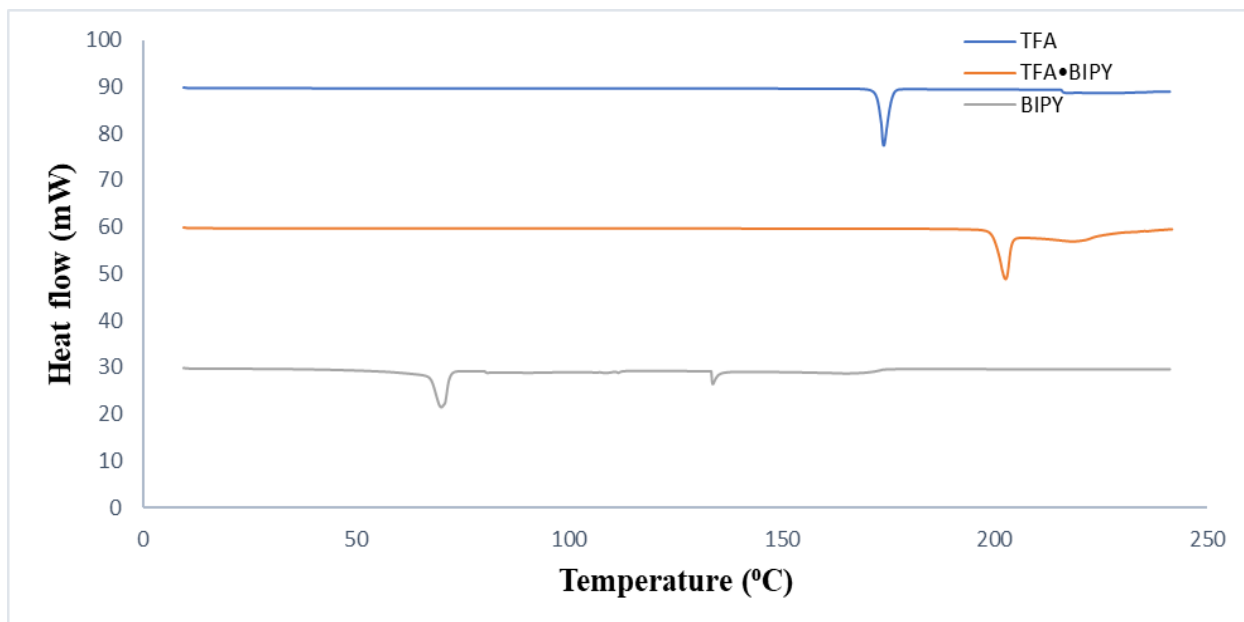
Figure 3.14: DSC curves of TFA (blue), BIPY (grey) and TFA•BIPY (orange)

3.6 PXRD analysis

The solvent assisted grinding technique was used in an attempt to prepare the two co-crystals. A few drops of solvent (25:75 (v/v) DMSO:propan-2-ol) were added to 1:1 ratios of *p*CA with BIPY and TFA with BIPY respectively. The PXRD patterns of the ground products were compared to those calculated from LAZY PULVERIX (Yvon *et al*. 1977). These are illustrated in Figures 3.15 and 3.16.   For 3(*p*CA)•3(BIPY), the single crystal PXRD pattern and the ground pattern have different peaks from that of their starting materials. However, the PXRD patterns of 3(*p*CA)•3(BIPY) differ for both techniques. For TFA•BIPY, a slight similarity in the patterns for both techniques was observed. Thus, as no perfect similarities were obtained when comparing the patterns of the two techniques, it can be concluded that unknown compounds were formed when trying to reproduce TFA•BIPY and 3(*p*CA)•3(BIPY) co-crystals using the solvent assisted grinding method.
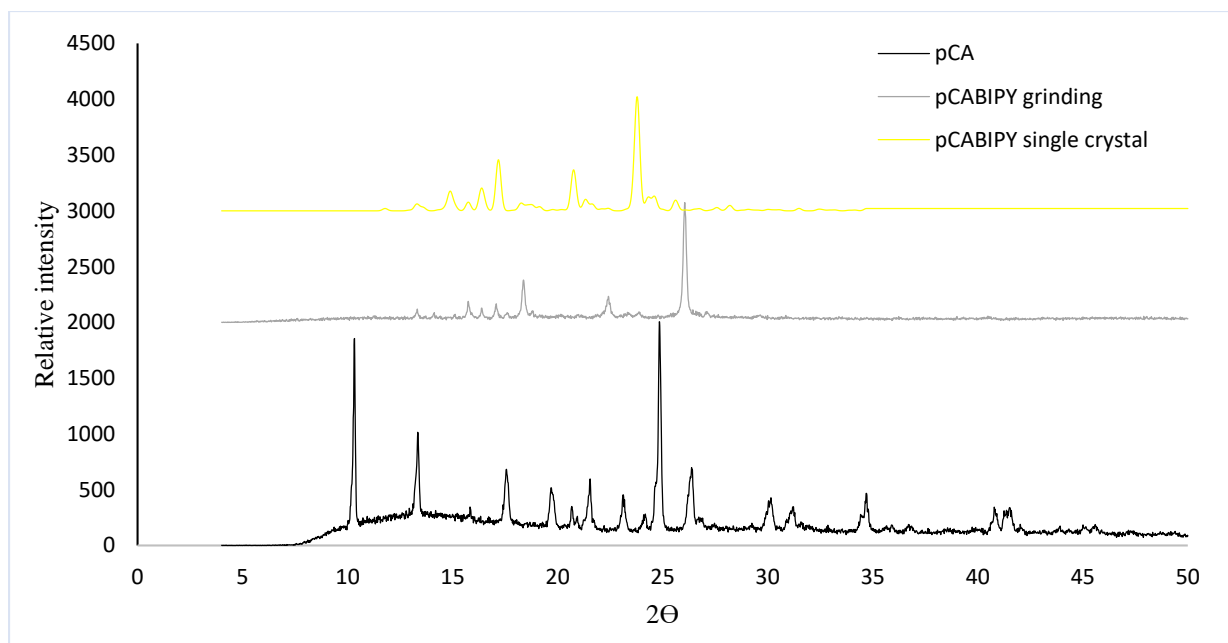
Figure 3.15: PXRD analyses of 3(pCA)•3(BIPY): the calculated pattern (yellow) obtained from LAZY PULVERIX, grinding experiment (grey) and pCA (black).
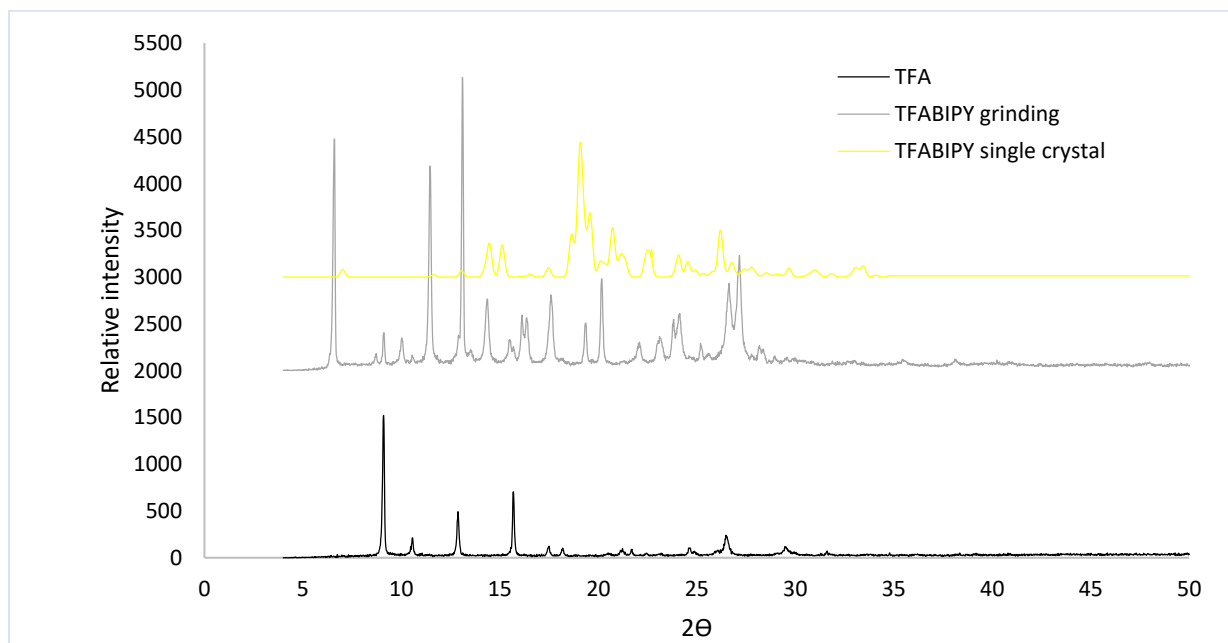
Figure 3.16: PXRD analyses of TFA•BIPY: the calculated pattern (yellow) obtained from LAZY PULVERIX, grinding experiment (grey) and TFA (black).

3.7 FTIR analysis

Infrared spectroscopy is one of the valuable supplementary techniques for the identification of new solid forms. Figure 3.17 and 3.18 show the corresponding IR spectra of co-crystals and starting materials. For both co-crystals, the resulting spectra are different from superimposed spectra of the starting materials. In this study, we are interested in COOH and OH FTIR features. For the 3(pCA)•3(BIPY) co-crystal, a peak shift was observed from 3373 cm^{-1} to 3439 cm^{-1} compared to the starting material. This shift can be assigned to the hydrogen bond interaction of the OH groups of *p*CA with the nitrogens of BIPY. The carboxylic acid bands of *p*CA, 2840 cm^{-1} is shifted to 2815 cm^{-1} as the carboxylic acid OH is involved in the hydrogen bonding with the nitrogen of BIPY. For the (TFA)•(BIPY) co-crystal, a shift is observed from 3432 cm^{-1} to 3000 cm^{-1} compared to the starting material. This can be attributed to the hydrogen bond formed between the phenol OH of TFA with the nitrogen of BIPY. A further relevant characteristic peak at 2460 cm^{-1} was assigned to the COOH forming a hydrogen bond with the nitrogen of BIPY.
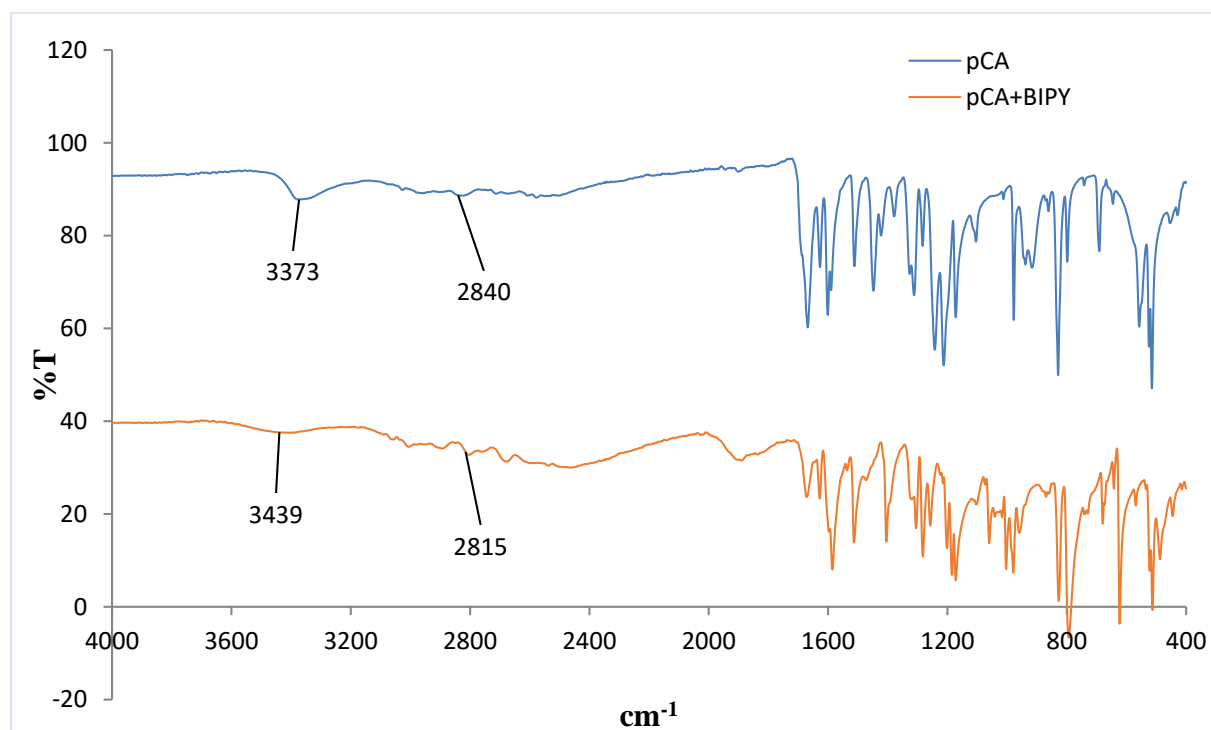
Figure 3.17: FTIR spectra of *p*CA (blue) and 3(*p*CA)•3(BIPY) (orange).
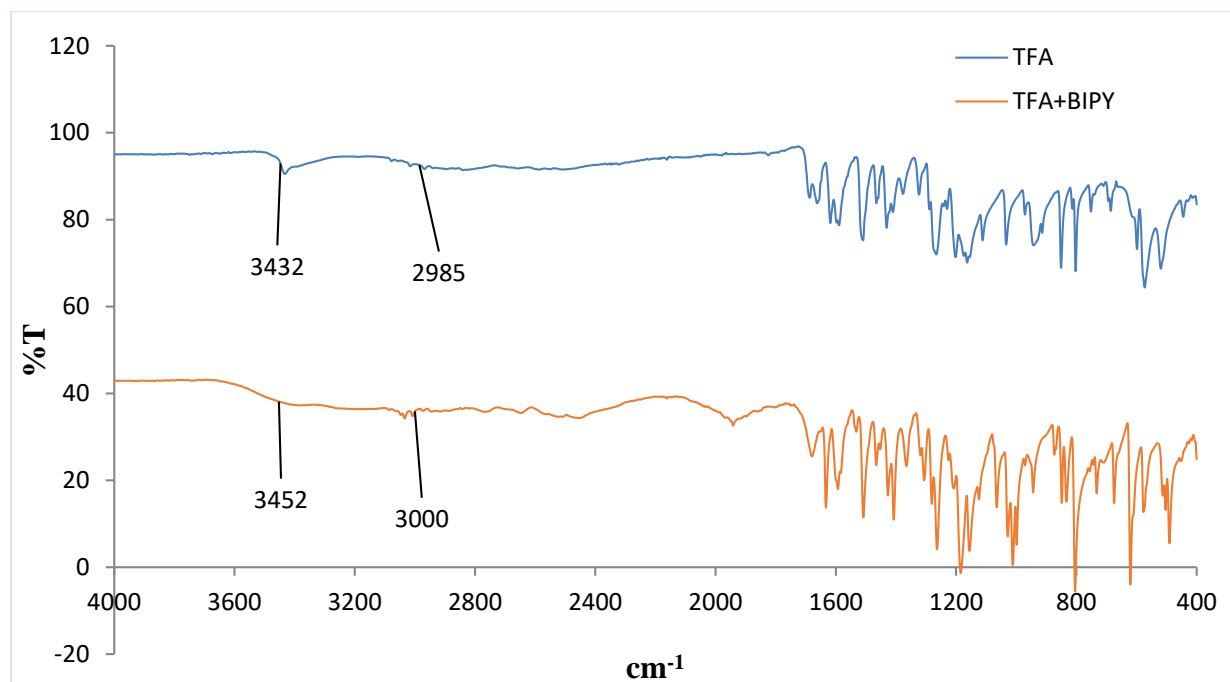
Figure 3.18: FTIR spectra of TFA (blue) and TFA•BIPY (orange).

3.8 Conclusion

Two co-crystals were successfully prepared which verified the pK$_a$ rule. The new solid forms were characterised using single crystal X-ray diffraction. Both crystal structures were solved in the monoclinic space group $P2_1/c$. pCA with BIPY resulted in a crystal structure having a higher Z' (3) compared to TFA with BIPY with a lower Z' (1). FTIR spectroscopy also clearly shows the presence of the OH band involved in the hydrogen bond in the spectra of both co-crystals.

The DSC results revealed that the TFA•BIPY co-crystal is more when stable compared to 3(pCA)•3(BIPY).

The preparation of the new solid forms using the solvent assisted grinding method showed that unknown compounds were formed and this was confirmed using PXRD analysis.

The two co-crystals have shown similarity in the O-H•••N supramolecular synthon, leading to the formation of $C_2^2(19)$ chains. However, no similarity was found in the crystal packing.

3.9 References

Bevill, M. J., Vlahova, P. I. & Smit, J. P., 2014. Polymorphic Cocrystals of Nutraceutical Compound p-Coumaric Acid with Nicotinamide: Characterization, Relative Solid-State Stability, and Conversion to Alternate Stoichiometries. *Cryst. Growth & Des. ,* Volume 14, p. 1438−1448.

Cruz-Cabeza, A., 2012. Acid-base crystalline complexes and the pK$_a$ rule. *CrystEngComm,* Volume 14, pp. 6362-6365.

Etter, M., Macdonald, J. & Bernstein, J., 1990. Graph-set analysis of hydrogen bond patterns. *Acta crystallographica,* Volume 46, pp. 256-262.

McKinnon, J., Jayatilaka, D. & Spackman, M., 2007. *Chem.Comm,* Volume 37, pp. 3814-3816.

Sheldrick, G. M. , 1997. Program for the Refinement of Crystal Structures from Diffraction Data. University of Göttingen, Göttingen, Germany.

Spackman, M. & McKinnon, J., 2002. *CrystEngComm,* Volume 4, pp. 378-392.

Yvon, K., Jeitschko, W. & Parthe, E. J., 1977. LAZY PULVERIX: a computer program for calculating X-ray and neutron diffraction powder patterns. *J. Appl. Cryst,* Volume 10, pp. 73-74.

CHAPTER 4: SALTS OF *p*-COUMARIC ACID AND *trans*-FERULIC ACID

4.1 Introduction

Salts are crystalline materials made of ionizable molecules that are held together by hydrogen bonding. Salt formation can be predicted by looking at the difference in pKa of the acid and the base with 95% salt probability expected when $\Delta pK_a \geq 4$ (Cruz-Cabeza, 2012). A salt can improve the physicochemical properties such as solubility of an API 100-1000 times more than co-crystallisation. Thus 50% of the drugs on the market are in a salt form (Cavanagh, *et al.*, 2017). This chapter focuses on the synthesis and characterisation of the salts of *p*-coumaric acid and *trans*-ferulic acid with selected aminopicolines (Figure 4.1). The ΔpK_a for *p*CA with 2A4MP and *p*CA with 2A6MP are respectively 3.61 and 3.59 while TFA with 2A4MP is 4.03.
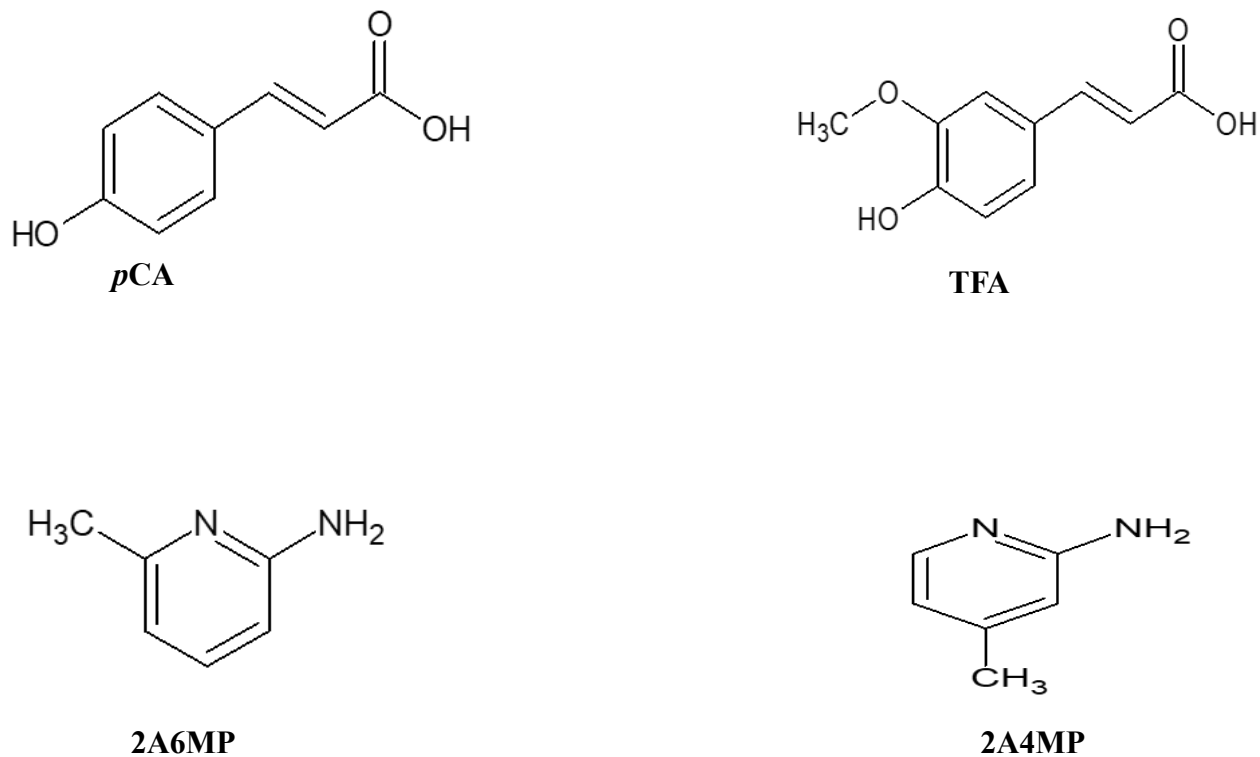

Figure 4.1: Chemical structures used in this study

4.2 Structural analysis of salts of *p*-coumaric acid and *trans*-ferulic acid

The salts formed block-like crystals, 2-amino-4-picolinium *p*-coumarate salt, $(p\text{CA}^-)(2\text{A4MP}^+)$ and 2-amino-6-picolinium *p*-coumarate salt, $4(p\text{CA}^-) \cdot 4(2\text{A6MP}^+)$ displayed a yellow colour, while the 2-amino-4-picolinium *trans*-ferulate salt, $(\text{TFA}^-)(2\text{A4MP}^+) \cdot (\frac{3}{2}\text{H}_2\text{O})$ is colourless. The structures were solved using direct methods with SHELXS-97 (Sheldrick, 1997). Table 4.1 below illustrates the crystal data parameters.

Table 4.1: Crystal data and refinement parameters of the salts of *p*CA and TFA

Compound	$(p\text{CA}^-)(2\text{A4MP}^+)$	$4(p\text{CA}^-)4(2\text{A6MP}^+)$	$(\text{TFA}^-)(2\text{A4MP}^+) \cdot (\frac{3}{2}\text{H}_2\text{O})$
Molecular formula	$C_{15}H_{16}N_2O_3$	$C_{60}H_{64}N_8O_{12}$	$C_{16}H_{21}N_2O_6$
M_r (g/mol)	272.30	1089.19	329.35
Temperature (K)	173	173	173
Crystal system	Orthorhombic	Monoclinic	Monoclinic
Space group	*Pbca*	$P2_1$	C2/*c*
a (Å)	12.056(2)	13.930(3)	20.111(4)
b (Å)	9.1511(18)	9.948(2)	12.016(2)
c (Å)	25.048(5)	20.797(4)	14.226(2)
α (°)	90	90	90
β (°)	90	94.33	104.96
γ (°)	90	90	90
V (Å^3)	2763.4(9)	2873.6(10)	3321.4(11)
Z	8	2	8
λ (Å)	0.71073	0.71073	0.71073
ρ (calcd) (g/cm^3)	1.309	1.259	1.317
Absorption coefficient μ (mm^{-1})	0.092	0.089	0.100
$2\theta_{max}$ (°)	56.6	55.8	56.7
Reflections collected	26738	23267	24936
No. data with $I > 2\sigma(I)$	3424	13608	4149
No. parameters	198	789	288
Final R ($I > 2\sigma(I)$)	R_1=0.0460; wR_2= 0.1049	R_1= 0.0574; wR_2= 0.1372	R_1= 0.0431; wR_2= 0.1072
R indices (all data)	R_1= 0.0714; wR_2= 0.1198	R_1= 0.0783; wR_2= 0.1493	R_1= 0.0540; wR_2= 0.1153
Goodness-of-fit on F^2	1.028	1.052	1.030
Min, max e$^-$ density (e Å^{-3})	-0.241, 0.199	-0.234, 0.239	-0.239, 0.297

4.2.1 Salt of *p*-coumaric acid with 2-amino-4-picoline

The salt of (*p*CA⁻)(2A4MP⁺) crystallised by dissolving a 1:1 molar ratio of *p*CA with 2A4MP in a 50:50(v/v) solvent mixture of tetrahydrofuran and 1,2-dichloroethane, which was left to evaporate at room temperature. Yellow crystals were obtained after one week. The structure was solved in the orthorhombic space group *Pbca*. The asymmetric unit contains one 2A4MP⁺ ion and one *p*CA⁻ ion, Figure 4.2.
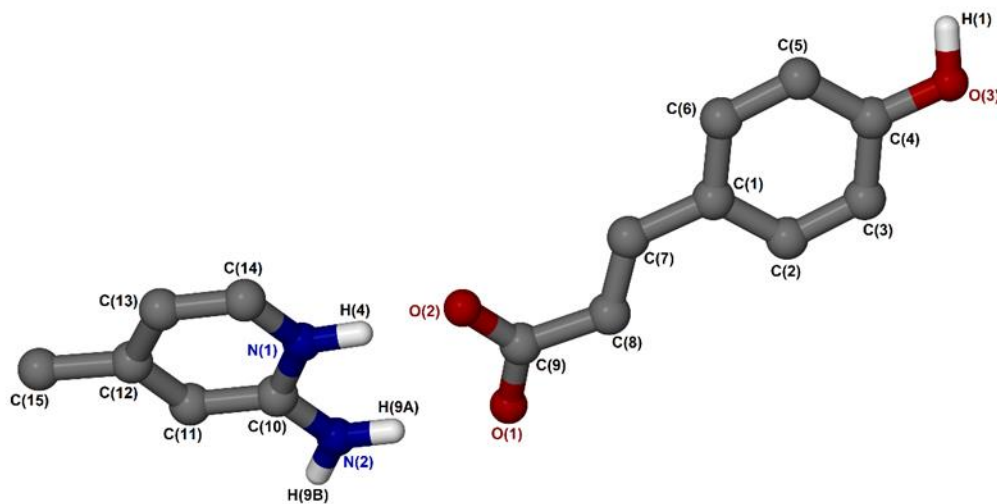
Figure 4.2: Numbering scheme of the asymmetric unit of (*p*CA⁻)(2A4MP⁺) with some hydrogen atoms omitted.

The *p*CA's carboxylic acid group was deprotonated to the pyridine's nitrogen of 2A4MP forming a heterosynthon (N_{pyr}^+-H•••COO⁻) and the amine group of 2A4MP also forms a hydrogen bond with the carboxylate group resulting in R_2^2 (8) rings with d(N1-O2) = 2.662 Å and d(N2-O1) = 2.671 Å, see Figure 4.3. This 2-aminopyridinium carboxylate heterosynthon is a robust interaction that has previously been studied (Bis & Zaworotko, 2005). The phenol OH

also forms O-H•••O hydrogen bonds to the carboxylate group of *p*CA⁻. The geometrical data of the hydrogen bonds are summarised in Table 4.2.
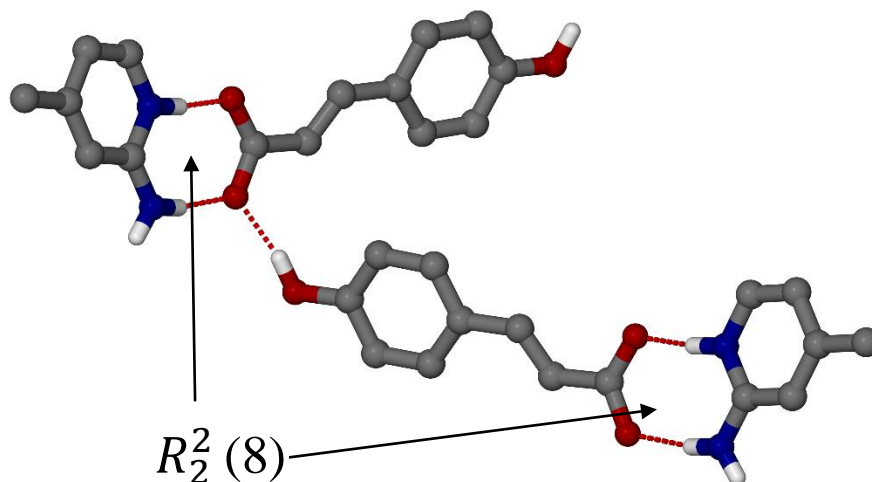
Figure 4.3: Hydrogen bond of (*p*CA⁻)(2A4MP⁺) salt with some hydrogen atoms omitted for clarity.

Table 4.2: Geometrical data for hydrogen bonds of (*p*CA⁻)(2A4MP⁺)

	D-H (Å)	H•••A (Å)	D•••A (Å)	<DHA (º)	Symmetry operation
N1-H4•••O2	0.95	1.71	2.662(2)	173.5	
N2-H9A•••O1	0.92	1.98	2.893(3)	171.6	
O3-H1•••O1	0.89	1.79	2.671(2)	169.6	x-½, y, -z+³/₂
N2-H9B•••O2	0.82	2.60	3.365(2)	156.3	x+½, -y+½, -z+1

The packing diagram of the (*p*CA⁻)(2A4MP⁺) salt is shown in Figure 4.4. A column of 2A4MP⁺ ions alternating a column of *p*CA⁻ ions forming $C_2^2(6)$ chains and a layer of *p*CA⁻ ions forming a ribbon supported with $C_1^1(10)$ chains (Etter, et al., 1990). There are also π•••π stacking interactions between 2A4MP⁺ ions with d(Cg-Cg) = 4.394 Å.
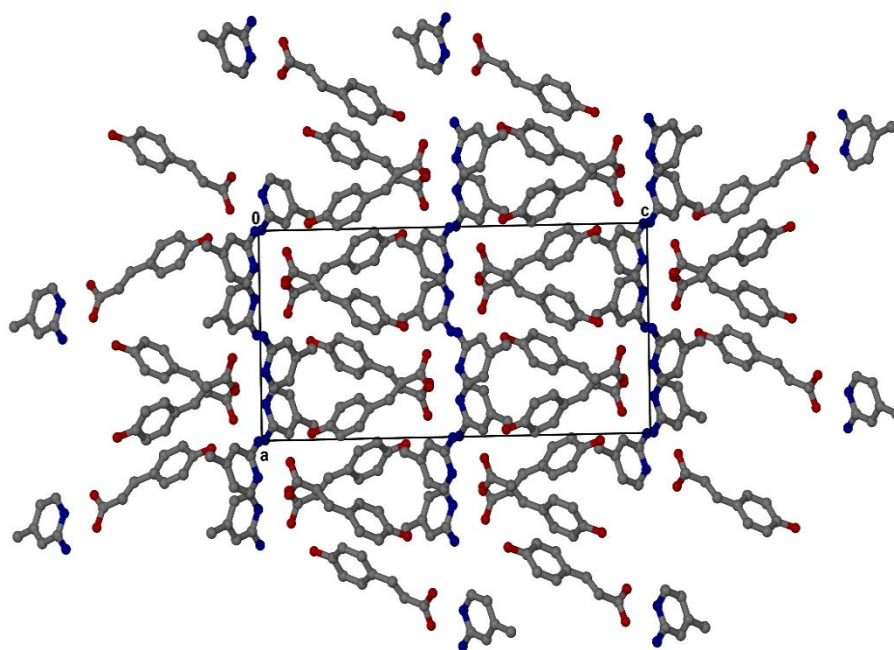
Figure 4.4: Packing diagram of (pCA$^-$)(2A4MP$^+$) along [010] with hydrogen atoms omitted.

4.2.2 Salt of p-coumaric acid and 2-amino-6-picoline

The salt of 4(pCA$^-$)4(2A6MP$^+$) was obtained by dissolving an equimolar mixture of pCA with 2A6MP in the solvent mixture, 25:75 (v/v) of 1,2-dichloroethane and ethanol using the slow evaporation method. The solution was left at room temperature for one week. The obtained yellow crystal was analysed and solved in the orthorhombic space group *Pbca* with the asymmetric unit containing four molecules of both pCA and 2A6MP, Figure 4.5.
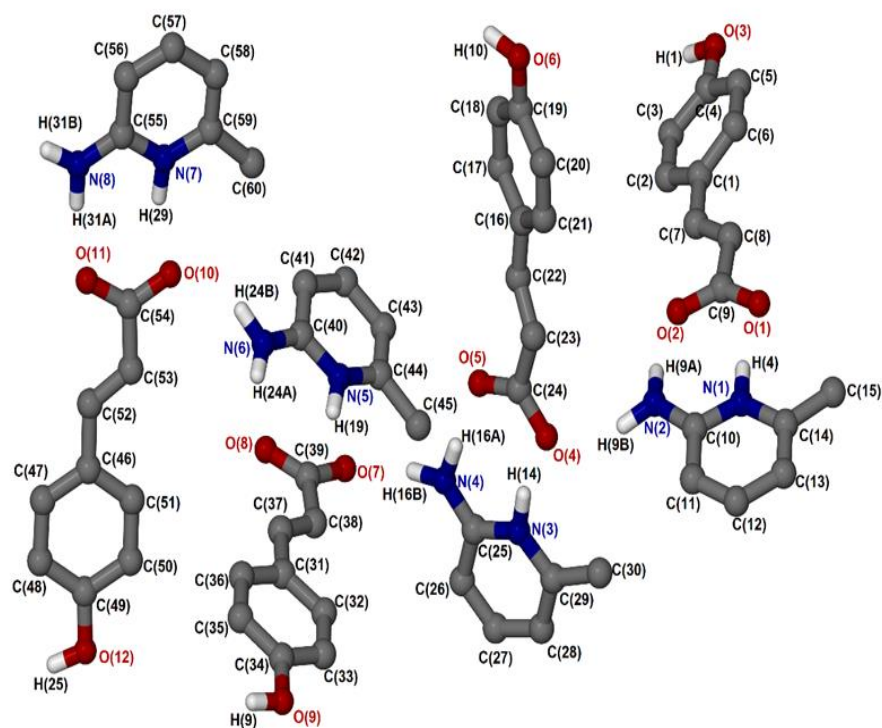
Figure 4.5: Numbering scheme of the asymmetric unit of 4(pCA$^-$)4(2A6MP$^+$) with some hydrogen atoms omitted.

The 2-aminopyridinium carboxylate heterosynthon persists forming R_2^2 (8) rings (Figure 4.6). Again, the phenol OH forms O-H•••O hydrogen bonds to the carboxylate group of pCA$^-$ resulting in $C_2^2(20)$ chains which gives a wave in the packing diagram, Figure 4.7. The geometrical data for the hydrogen bonds is summarised in Table 4.3.

$R_2^2 (8)$
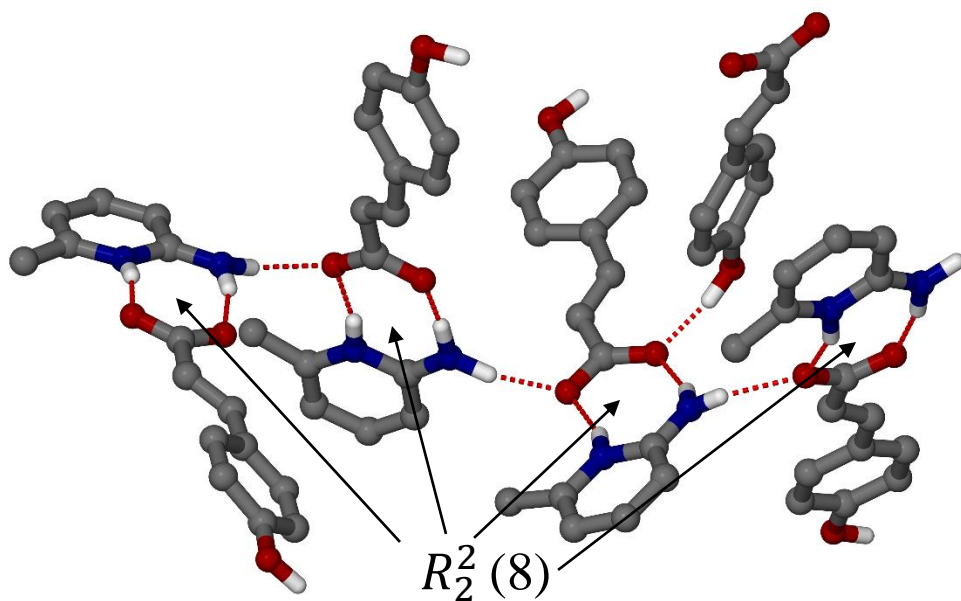
Figure 4.6: Hydrogen bond of 4(pCA$^-$)4(2A6MP$^+$) salt with some hydrogen atoms omitted for clarity.
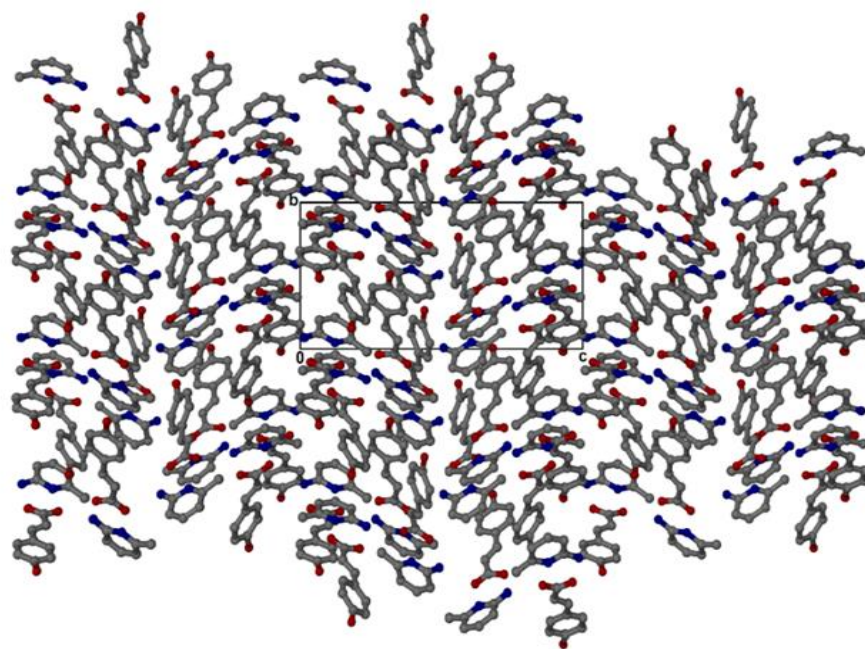
Figure 4.7: Packing diagram of 4(pCA$^-$)4(2A6MP$^+$) along [100] with hydrogen atoms omitted.

Table 4.3: Geometrical data for hydrogen bond of 4(*p*CA⁻)4(2A6MP⁺)

	D-H (Å)	H•••A (Å)	D•••A (Å)	<DHA (º)	Symmetry operation
N1-H4•••O1	0.88	1.87	2.741(3)	169	
N2-H9A•••O2	0.93	1.92	2.822(4)	1.65.7	
N3-H14•••O4	0.95	1.82	2.753(3)	1.65.5	
N4-H16A•••O5	1.00	1.76	2.758(3)	172.3	
N5-H19•••O7	0.97	1.80	2.722(2)	1.59.4	
N6-H24A•••O8	0.87	2.00	2.845(3)	163.5	
N7-H29•••O10	0.97	1.81	2.793(3)	158.6	
N8-H31•••O11	0.93	1.87	2.793(3)	167.7	
N2-H9B•••O4	0.94	2.05	2.941(3)	156.1	
N4-H16B•••O7	0.99	1.90	2.861(3)	162.7	
N6-H24B•••O10	0.92	2.06	2.898(3)	151.8	
O3-H1•••O8	0.92	1.77	2.668(3)	165.1	-x, y-½, 1-z
O9-H9•••O2	0.90	1.72	2.621(3)	175.8	1-x, ½+y, 1-z
N8-H31B•••O1	0.96	1.97	2.894(3)	161.0	x, y, 1+z
O6-H10•••O5	0.96	1.71	2.666(3)	171.1	-x, ½+y, 1-z
O12-H25•••O11	0.89	1.73	2.606(3)	169.1	1-x, y-½, 2-z

4.2.3 Salt of *trans*-ferulic acid with 2-amino-4-picoline

A 1:1 ratio of TFA and 2A4MP was transferred into a vial containing a solvent mixture of 25/75 (v/v) of 1,2-dichloroethane and ethanol. The mixture was stirred and left on a hot plate at 60 °C, two drops of water was added to give a solution. A hydrated salt was obtained after 4 days at room temperature, thus the water was incorporated into the crystal structure. The structure was solved in the monoclinic space group C2/*c*. The asymmetric unit consists of one TFA⁻ anion, one 2A4MP⁺ cation and $^3/_2$ molecules of water, Figure 4.8. Once again, the structure is characterized

by the carboxylate aminopyridinium heterosynthon with d(N1-O2) = 2.647 Å and d(N2-O1) = 2.904 Å.
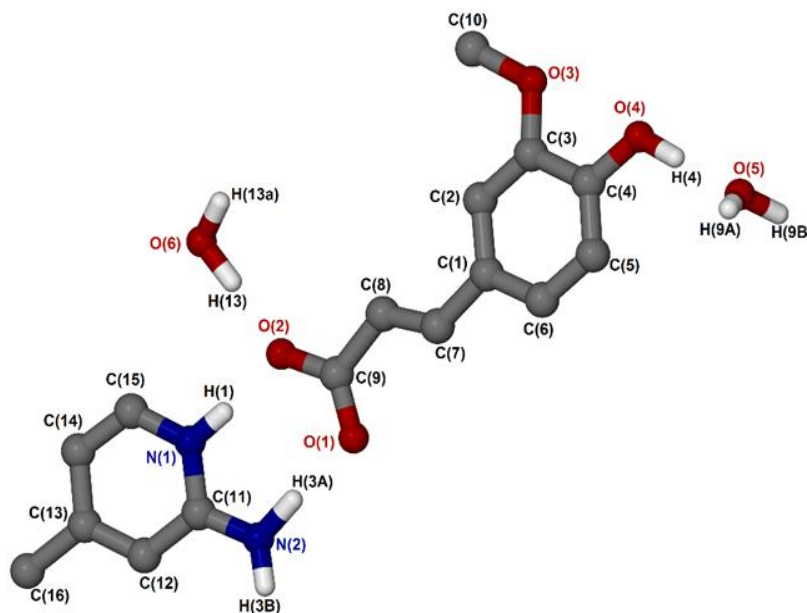

Figure 4.8: Numbering scheme of the asymmetric unit of $(TFA^-)(2A4MP^+) \cdot (\frac{3}{2} H_2O)$ with some hydrogen atoms omitted for clarity.

The hydrated salt of $(TFA^-)(2A4MP^+) \cdot (\frac{3}{2} H_2O)$ has three moderate hydrogen bonds involving nitrogen *i.e.*. the $N_{pyr}{}^+$-H•••O⁻ (pyridinium carboxylate synthon), N-H•••O⁻ (amine carboxylate synthon), N-H•••O (amine hydroxyl heterosynthon). There are also moderate O-H•••O⁻ and O-H•••O hydrogen bonds. In addition, there is a very weak hydrogen bond (C-H•••O) between an aromatic H and the methoxy group. The hydrogen bond data are summarised in Table 4.4. The 2-aminopyridium carboxylate heterosynthon persist again with a $R_2^2(8)$ rings. The water molecules act as a bridge connecting two TFA⁻ ions forming $R_4^4(24)$ rings. The TFA⁻ anions are linked to 2A4MP⁺ cations via N-H•••O hydrogen bonding forming $C_2^2(14)$ chains. The TFA anion is disordered over two positions with the major component having a site occupancy of 0.80837 and the minor component being 0.19163. The hydrogen bonding is shown in Figure 3 with the major component of the TFA anion shown Figure 4.9. There are π•••π stacking interactions between TFA⁻ anions with d(Cg-Cg) = 3.855 Å and there are also π•••π stacking

interactions between 2A4MP$^+$ cations with d(Cg-Cg) = 3.539 Å. The packing diagram is shown in Figure 4.10.
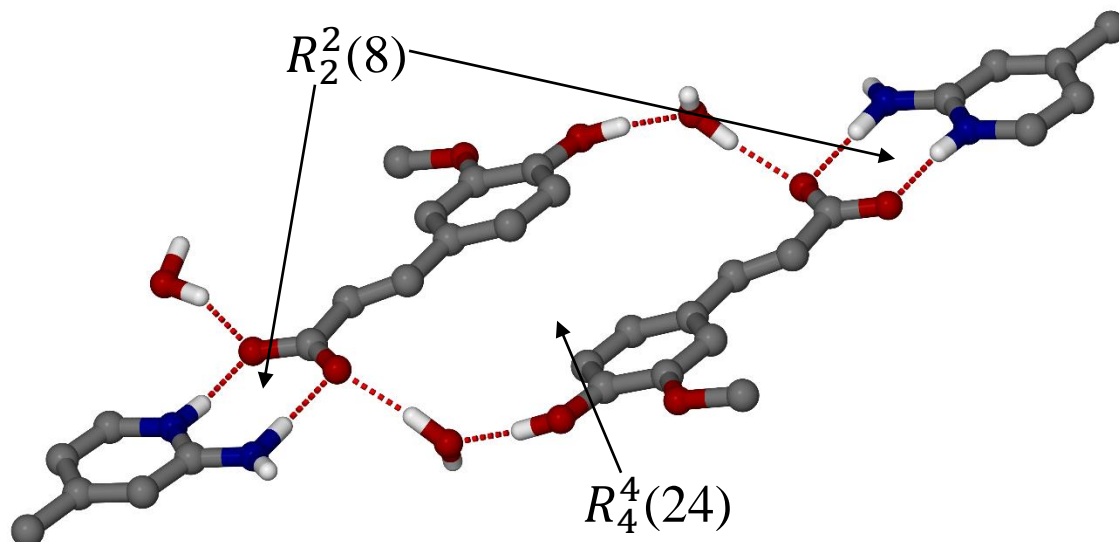
Figure 4.9: Hydrogen bond of (TFA$^-$)(2A4MP$^+$)•($\frac{3}{2}$H$_2$O) salts with some hydrogen atoms omitted for clarity.

Table 4.4: Geometrical data for hydrogen bond of (TFA$^-$)(2A4MP$^+$)($\frac{3}{2}$H$_2$O)

	D-H (Å)	H•••A (Å)	D•••A (Å)	<DHA (º)	Symmetry operation
N1-H1•••O2	0.90(3)	1.75 (3)	2.647(3)	172(3)	
N2-H3A•••O1	1.05(3)	1.85(3)	2.904(3)	175(2)	
O6-H13•••O2	0.97(4)	1.75(4)	2.661(2)	156(4)	
O6-H13•••O2	0.95(4)	1.64(4)	2.589(3)	174(3)	
N2-H3B•••O4	0.91	2.10(4)	2.964(3)	156(3)	x-½, y+^{5}/$_2$, z-½
O5-H9B•••O1	0.92(4)	1.84(4)	2.745(3)	169(3)	-x, -y+2, -z
O5-H9A•••O6	0.64(4)	2.16(4)	2.789(3)	170(5)	x, y-1, z
C12-H12•••O3	0.95	3.28	3.447(3)	92.2	-x, -y+3, -z
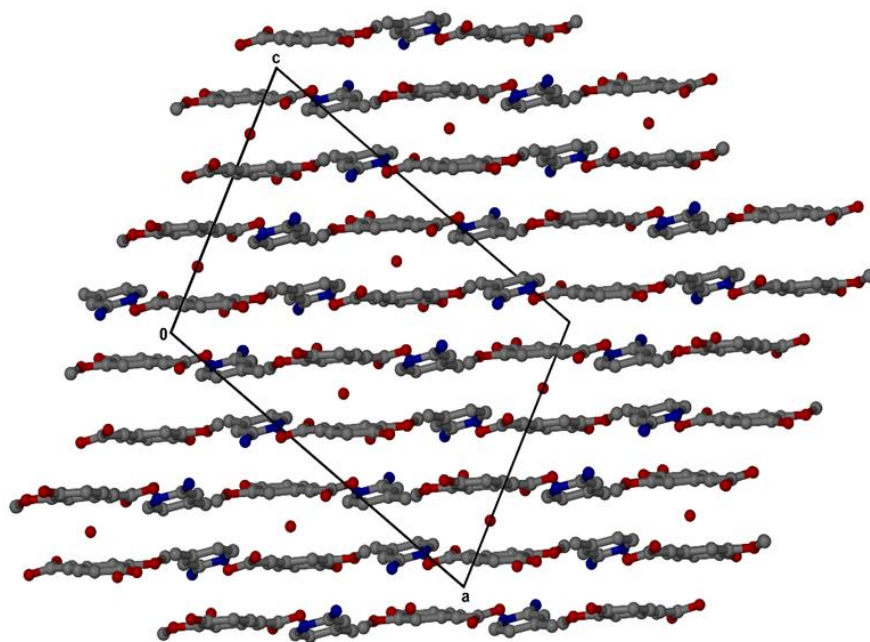
Figure 4.10: Packing diagram of (TFA$^-$)(2A4MP$^+$)•($\frac{3}{2}$H$_2$O) along [010] with hydrogen atoms omitted.

4.3 Torsion angles

The same torsion angles were considered as discussed in chapter 3, Figure 4.11. The torsion angles for all four pCA$^-$ anions in 4(pCA$^-$)4(2A6MP$^+$) were collected and significant differences were found. For this salt, $\boldsymbol{\tau_1}$ varied from 0.5-14.4^o and $\boldsymbol{\tau_2}$ varied from 5.1-26.7^o. (pCA$^-$)(2A4MP$^+$) showed similar flexibility in the rotation of the ring ($\boldsymbol{\tau_1}$) compared to 4(pCA$^-$)4(2A6MP$^+$) with $\boldsymbol{\tau_1}$ = 12.8^o. However (pCA$^-$)(2A4MP$^+$) has a lower $\boldsymbol{\tau_2}$ of 10.1^o. TFA$^-$ has both the lowest ring twist torsion angle ($\boldsymbol{\tau_1}$ = 0.2^o) and the lowest carboxylic acid twist torsion angle ($\boldsymbol{\tau_2}$ = 4.9^o). Table 4.5 summarises the torsion angles for the constructed salts.
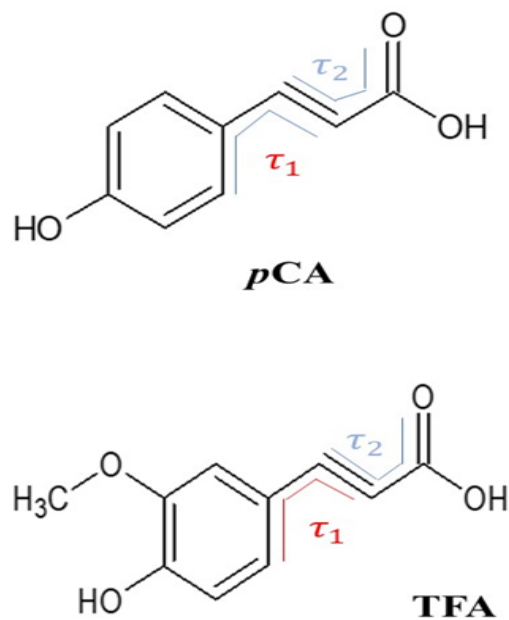
Figure 4.11: Torsion angles of *p*CA and TFA

Table 4.5: Torsion angles of $(p\text{CA}^-)(2\text{A4MP}^+)$, $4(p\text{CA}^-)4(2\text{A6MP}^+)$ and $(\text{TFA}^-)(2\text{A4MP}^+)\bullet(\frac{3}{2}$ $H_2O)$.

	$(p\text{CA}^-)(2\text{A4MP}^+)$	$4(p\text{CA}^-)4(2\text{A6MP}^+)$	$(\text{TFA}^-)(2\text{A4MP}^+)\bullet(\frac{3}{2} H_2O)$
Torsion angle	(°)	(°)	(°)
τ_1(C2-C1-C7-C8)	12.8	14.4	0.2
τ'_1(C17-C16-C22-C23)	-	0.5	-
τ''_1(C32-C31-C37-C38)	-	2.7	-
τ'''_1(C47-C46-C52-C53)	-	4.6	-
τ_2(C7-C8-C9-O1)	10.1	12.8	4.9
τ'_2(C22-C23-C24-O4)	-	26.7	-
τ''_2(C37-C38-C39-O7)	-	9.1	-
τ'''_2(C52-C53-C54-O10)	-	5.1	-

4.4 Hirshfeld surface analysis

The 2-D fingerprint plots of the salts for all major intermolecular interactions are shown in Figure 4.12 for pCA^- in $(pCA^-)(2A4MP^+)$ salt, Figure 4.13-4.16 for the four pCA^- anions in $4(pCA^-)4(2A6MP^+)$ and Figure 4.17 for TFA^- in $(TFA^-)(2A4MP^+)\bullet(\frac{3}{2}H_2O)$. For all three salts, it was observed that the leading interactions are as follows, $H\bullet\bullet\bullet H > O\bullet\bullet\bullet H > C\bullet\bullet\bullet H$. The molecular stacking $\pi\bullet\bullet\bullet\pi$ represented by $C\bullet\bullet\bullet C$ contributes the least in the stability of the salt with $(TFA^-)(2A4MP^+)\bullet(\frac{3}{2}H_2O)$ having the highest $C\bullet\bullet\bullet C$ contribution (7.5%). Similar percentage contributions were found for the $O\bullet\bullet\bullet H$ interactions in the three salts. For all three salts, the $C\bullet\bullet\bullet H$ contacts are shown as asymmetric wings. The $H\bullet\bullet\bullet H$ contacts is prominent in the molecular packing and appear as scattered points in the middle of the region of the 2D fingerprint plots. The $(TFA^-)(2A4MP^+)\bullet(\frac{3}{2}H_2O)$ salt has the highest $H\bullet\bullet\bullet H$ contribution (45.1%) and the lowest $C\bullet\bullet\bullet H$ contribution (13.5%). The quantitative summary of various interactions of both pCA^- and TFA^- anions is depicted in Table 4.6.
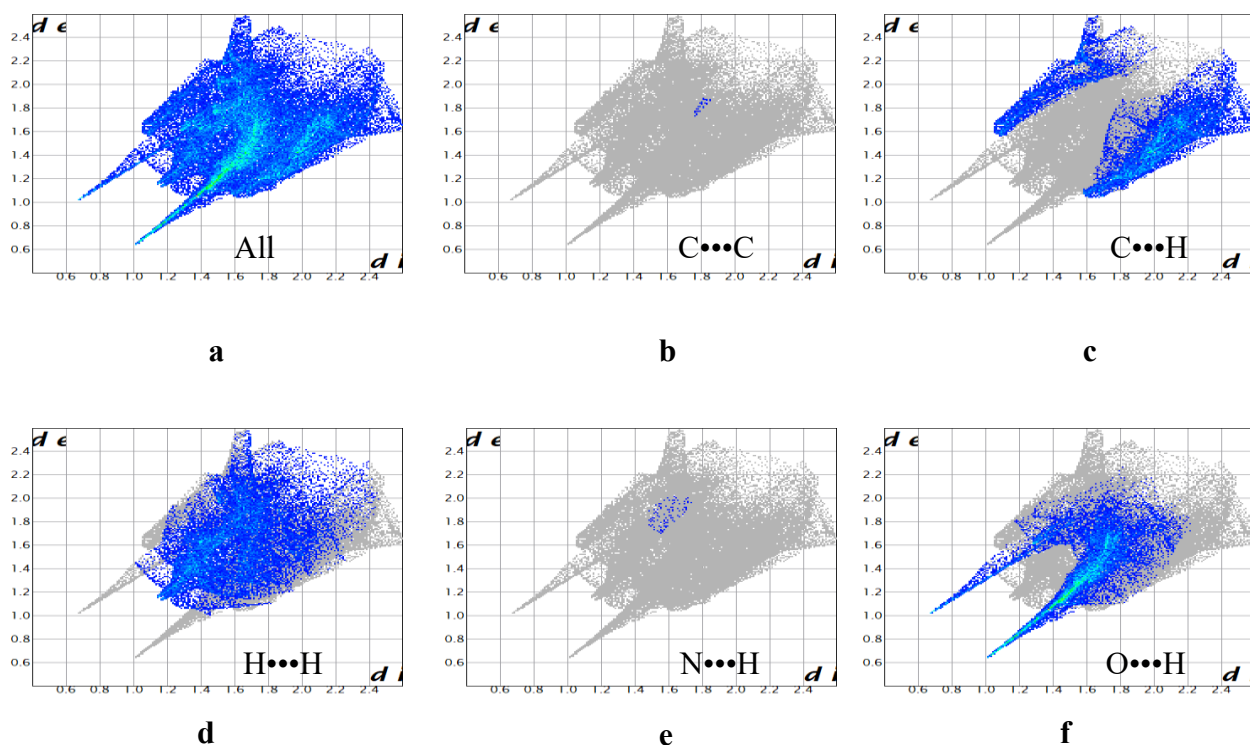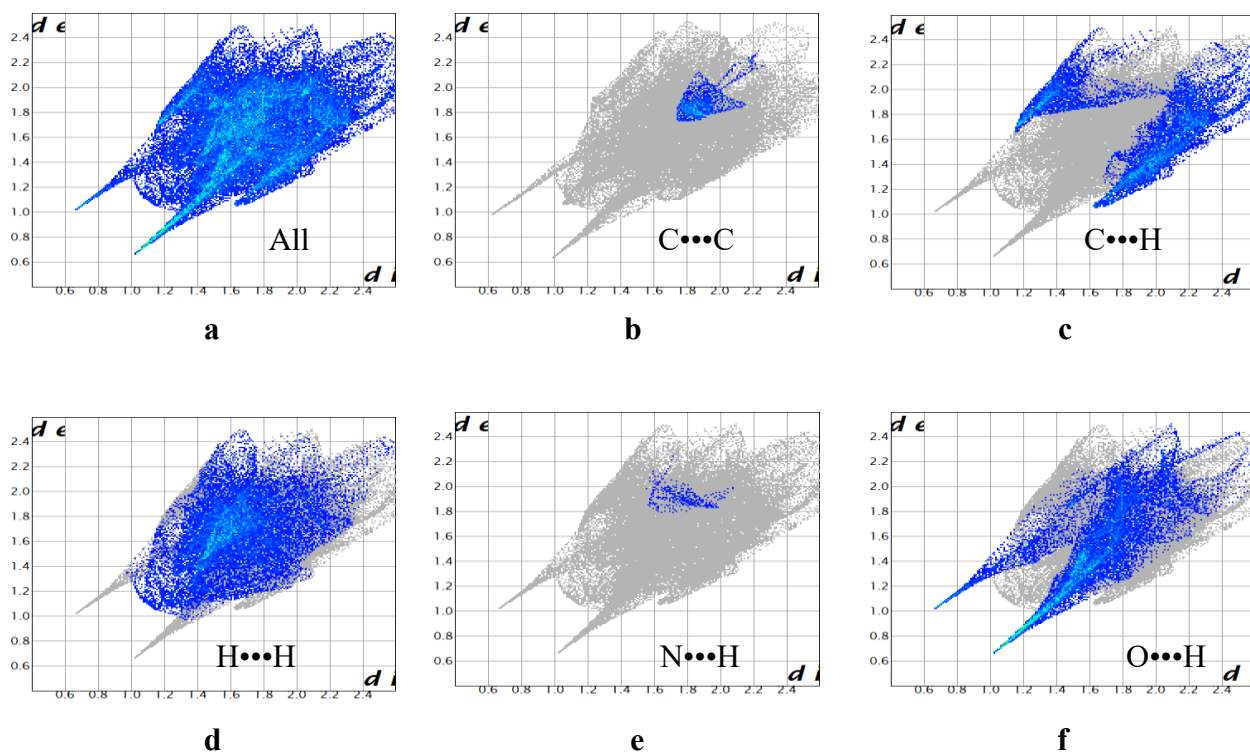
Figure 4.12: Fingerprint plot of pCA in the $(pCA^-)(2A4MP^+)$ salt.

Figure 4.13: Fingerprint plot of pCA in the $4(p$CA$^-)4(2$A6MP$^+)$ salt.
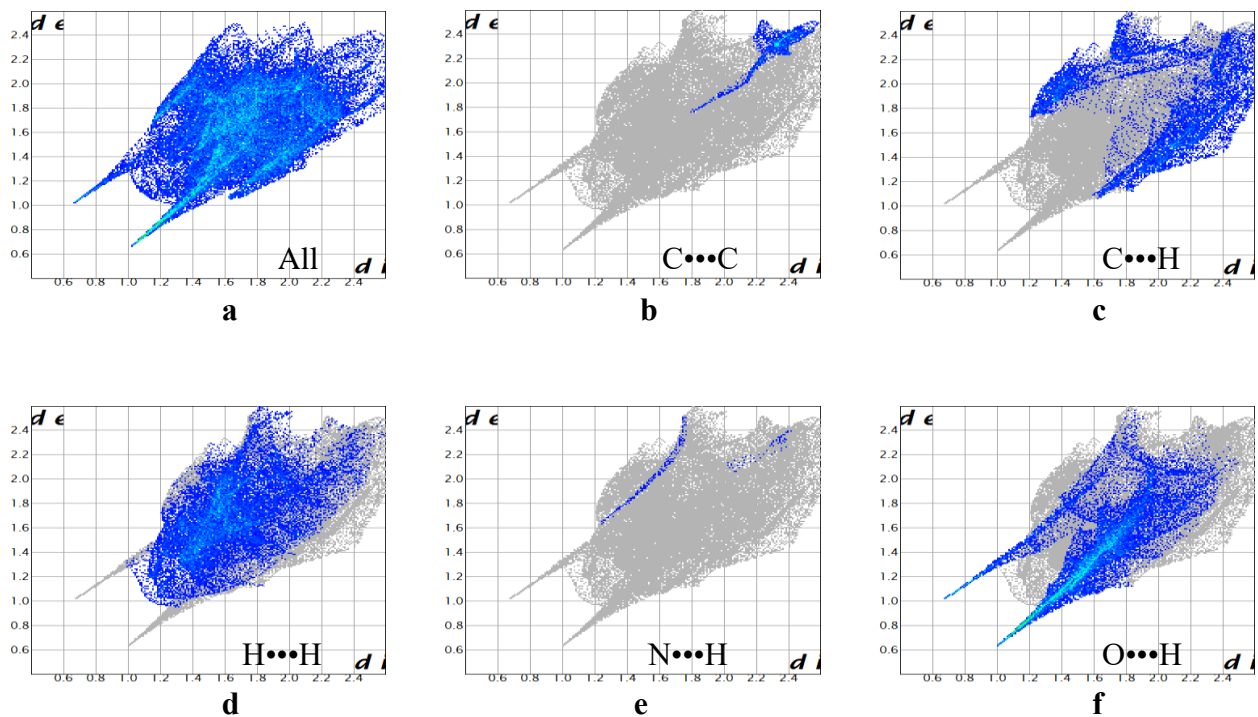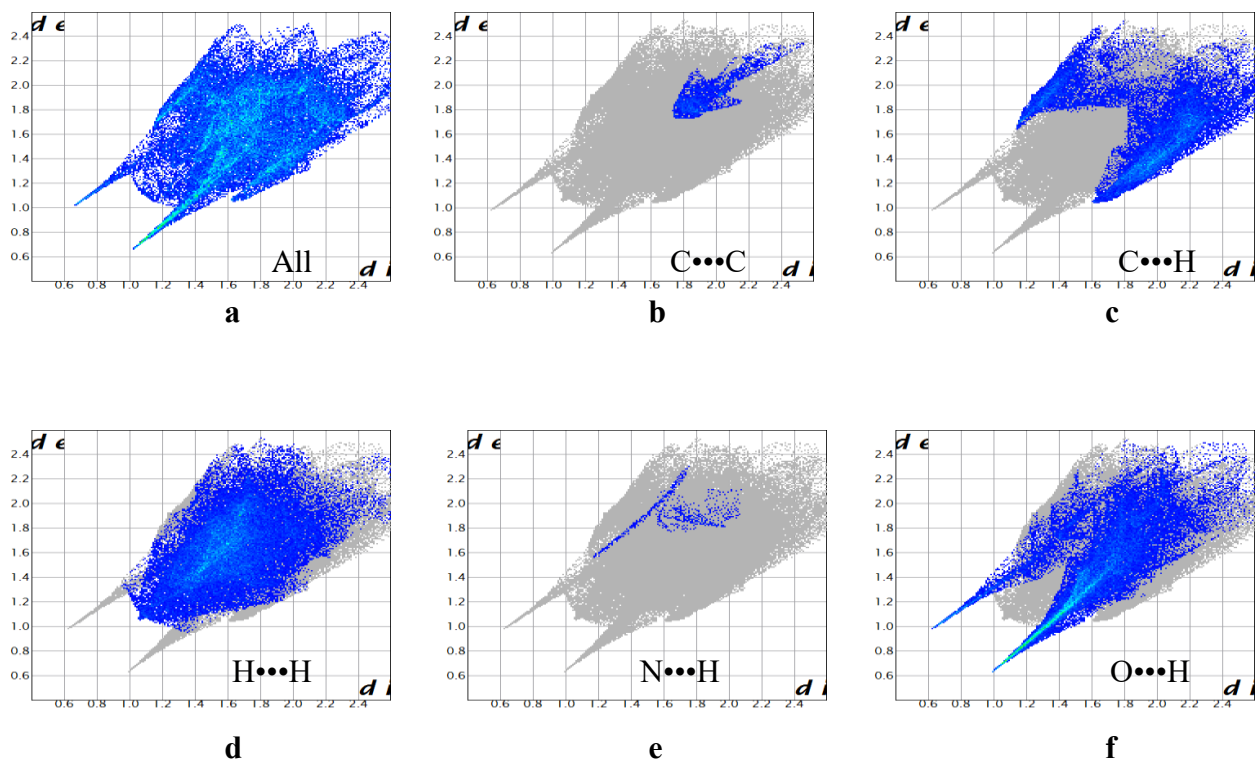
Figure 4.14: Fingerprint plot of *p*CA′ in the 4(*p*CA⁻)4(2A6MP⁺) salt

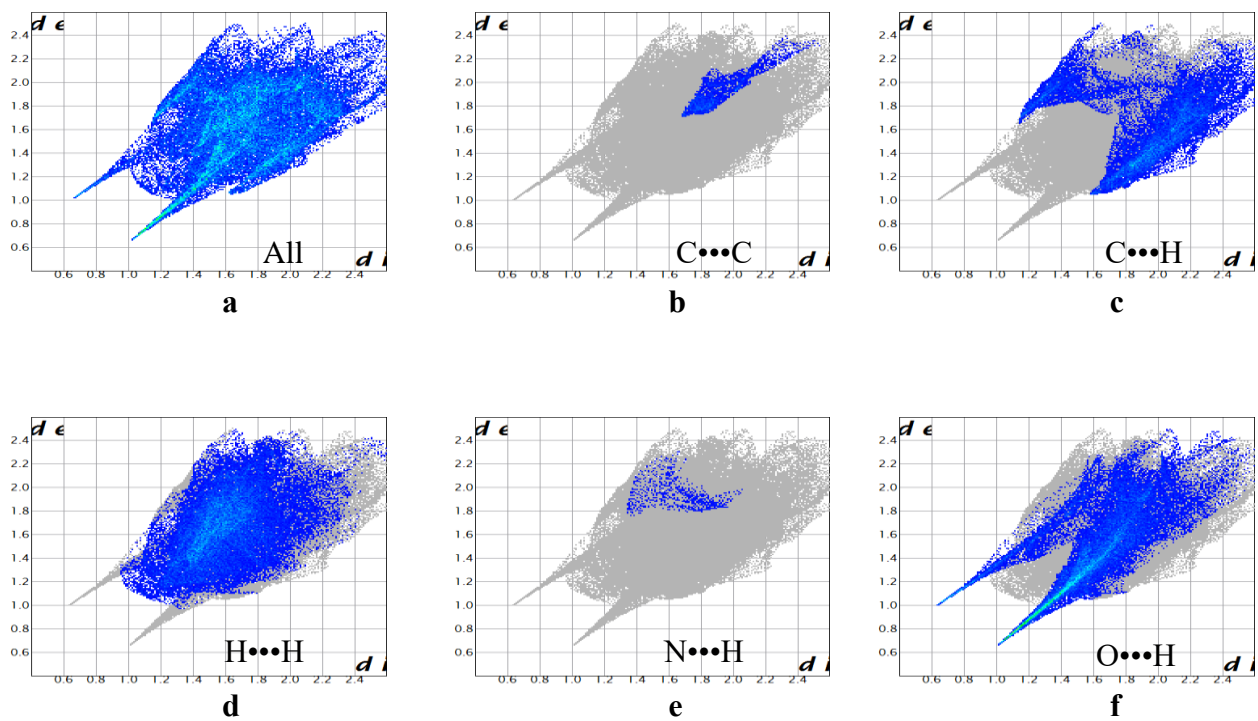Figure 4.15: Fingerprint plot of *p*CA″ in 4(*p*CA⁻)4(2A6MP⁺) salt

58

Figure 4.16: Fingerprint plot of pCA''' in 4(pCA⁻)4(2A6MP⁺) salt
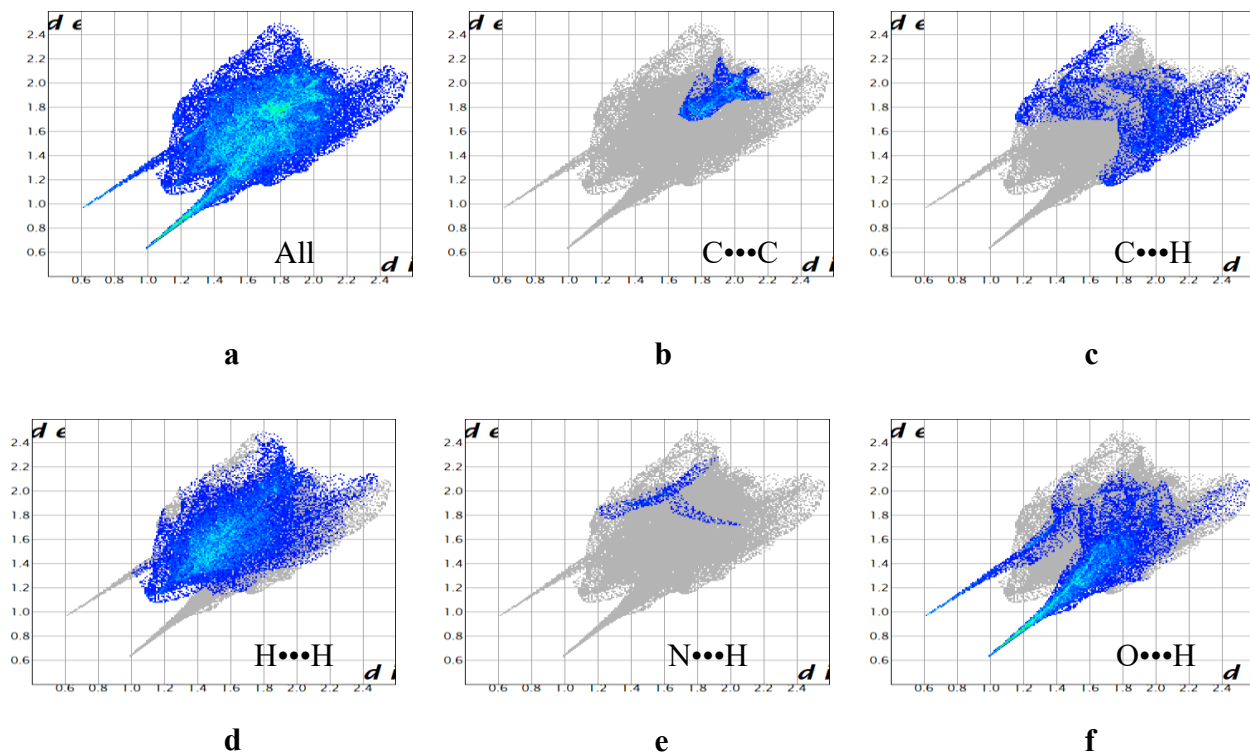
Figure 4.17: Fingerprint plot of TFA in the $(TFA^-)(2A4MP^+) \cdot (\frac{3}{2}H_2O)$ salt.

Table 4.6: Quantitative summary of the various interactions of pCA and TFA salts

Compounds	C•••C (%)	C•••H (%)	H•••H (%)	N•••H (%)	O•••H (%)
$(p\text{CA}^-)(2\text{A4MP}^+)$	0.1	29.6	38.3	0.2	30.1
$4(p\text{CA}^-)4(2\text{A6MP}^+)$	1.7	25.2	38.9	0.7	30.8
$4(p\text{CA}^-)4(2\text{A6MP}^+)'$	3.4	22.7	38.4	0.5	31.6
$4(p\text{CA}^-)4(2\text{A6MP}^+)''$	2.8	23.3	40	0.7	30.7
$4(p\text{CA}^-)4(2\text{A6MP}^+)'''$	2.5	21.9	39.6	0.8	32.1
$(\text{TFA}^-)(2\text{A4MP}^+) \cdot (\frac{3}{2}\text{H}_2\text{O})$	7.5	13.5	45.1	1.3	29.5

4.5 PXRD analysis

An equimolar mixture of pCA with 2A4MP was placed in a mortar and ground for 20 minutes with a few drops of the solvent mixture, 75:25 (v/v) ethanol and 1,2-dichloroethane. The same method was used for pCA with 2A6MP and for TFA with 2A4MP. The PXRD patterns of the ground products were compared to that of the calculated patterns from LAZY PULVERIX (Yvon, *et al*., 1977). For pCA and 2A4MP the ground PXRD pattern showed similarities to

those of the starting materials and the calculated pattern indicating that the reaction was incomplete (Figure 4.18).

The ground PXRD pattern of *p*CA with 2A6MP is different to that of the starting materials and to the calculated pattern indicating that a new compound was formed (Figure 4.19). The ground PXRD pattern of TFA with 2A4MP showed some similarities with the starting materials and the calculated pattern indicating that partial reaction had occurred (Figure 4.20).

Figure 4.18: PXRD analyses of (*p*CA$^-$)(2A4MP$^+$), the calculated pattern (yellow) obtained from LAZY PULVERIX, grinding experiment (grey) and *p*CA (black).
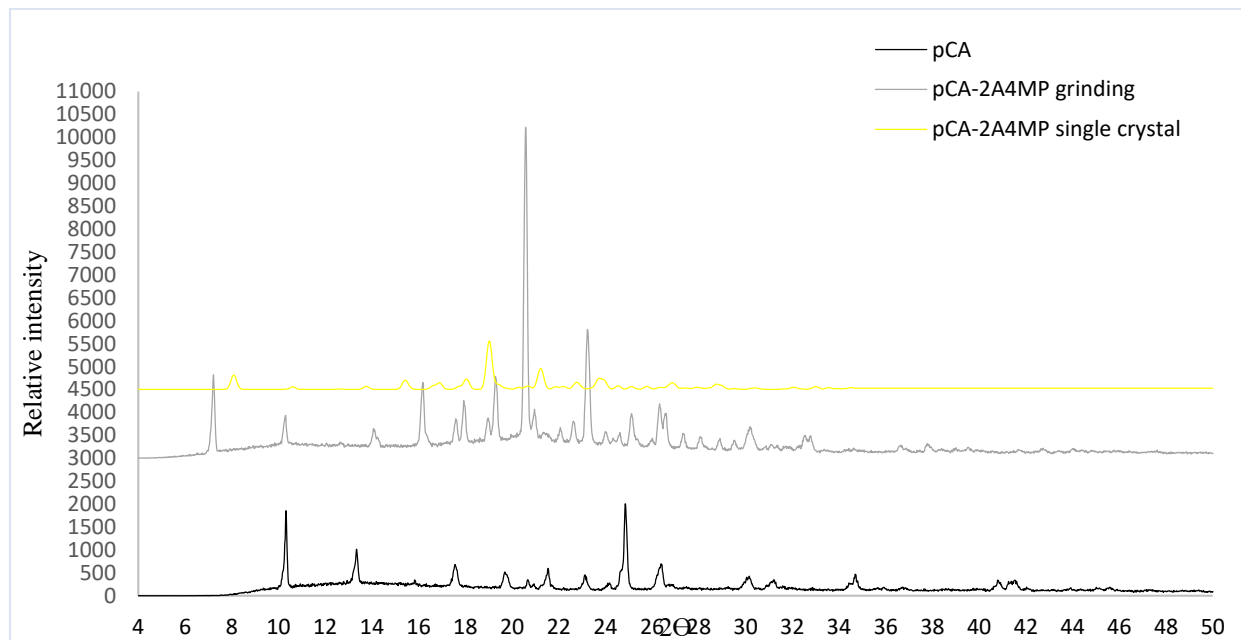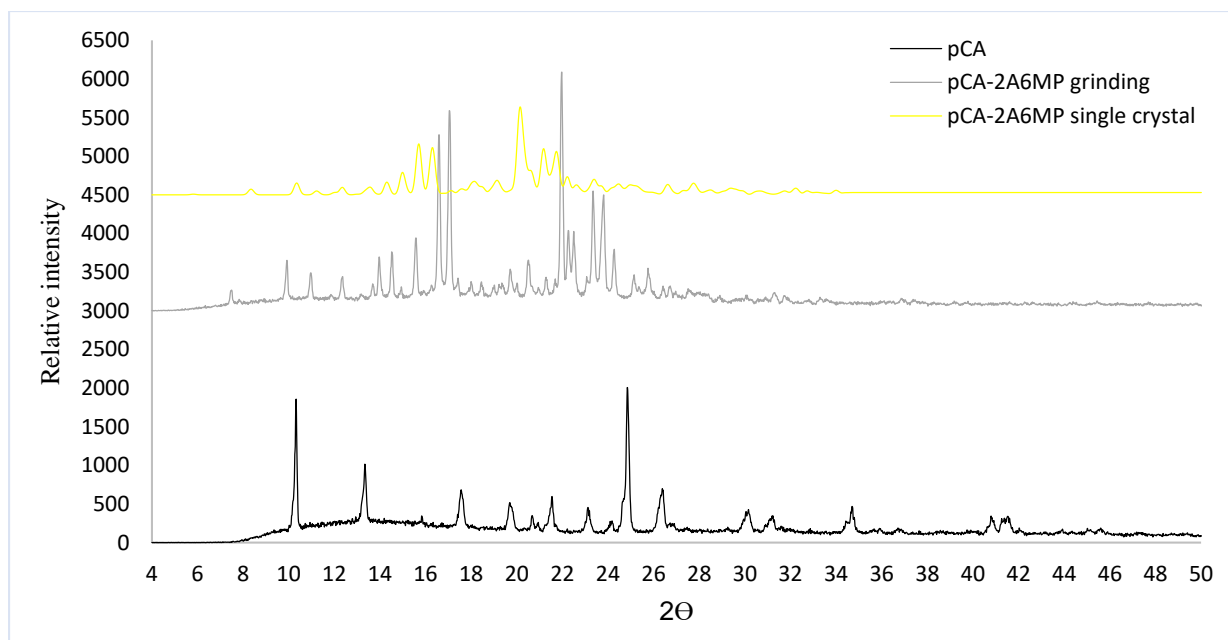
Figure 4.19: PXRD analyses of 4(*p*CA⁻)4(2A6MP⁺), the calculated pattern (yellow) obtained from LAZY PULVERIX, grinding experiment (grey), *p*CA (black) and 2A6MP (orange)
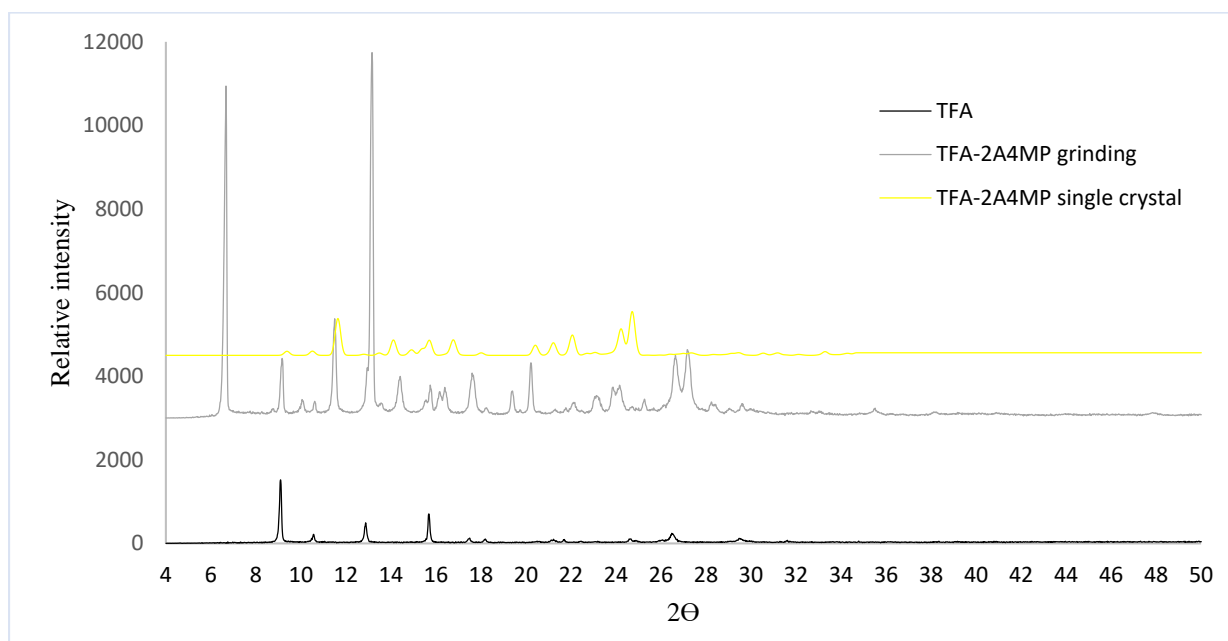

Figure 4.20: PXRD analyses of $(TFA^-)(2A4MP^+) \cdot (\frac{3}{2}H_2O)$, the calculated pattern (yellow) obtained from LAZY PULVERIX, grinding experiment (grey), TFA (black) and 2A4MP (orange).

4.6 Thermal analysis

2A4MP, 2A6MP, pCA, TFA and their salts were characterised by DSC. The melting point of the (pCA$^-$)(2A4MP$^+$) salt results in an endothermic peak at 170 °C which differs from the melting points of pCA (214.9 °C) and that of 2A4MP (99.9 °C), Figure 4.21. The DSC curve for the salt 4(pCA$^-$)4(2A6MP$^+$) is shown in Figure 4.22. This salt melts at a slightly higher temperature (173.3 °C) compared to (pCA$^-$)(2A4MP$^+$). This melting point is also in between that of pCA at 214.9 °C and 2A6MP at 128.3 °C. (TFA$^-$)(2A4MP$^+$)•($\frac{3}{2}$H$_2$O) has the lowest melting point at 135 °C. The melting point of the TFA salt is also in between those of the starting materials TFA (174.5°C) and 2A4MP (99.9 °C), Figure 4.23. The inclusion of water could have contributed to the lower melting point of this salt. The thermal analysis data are summarised in Table 4.7.

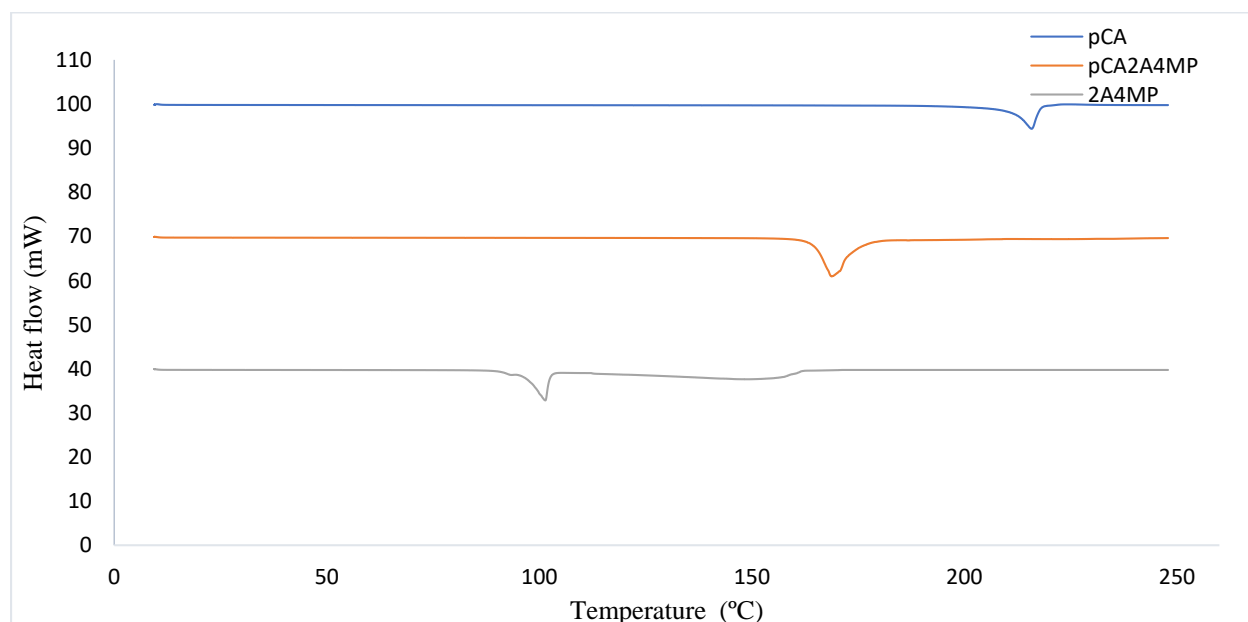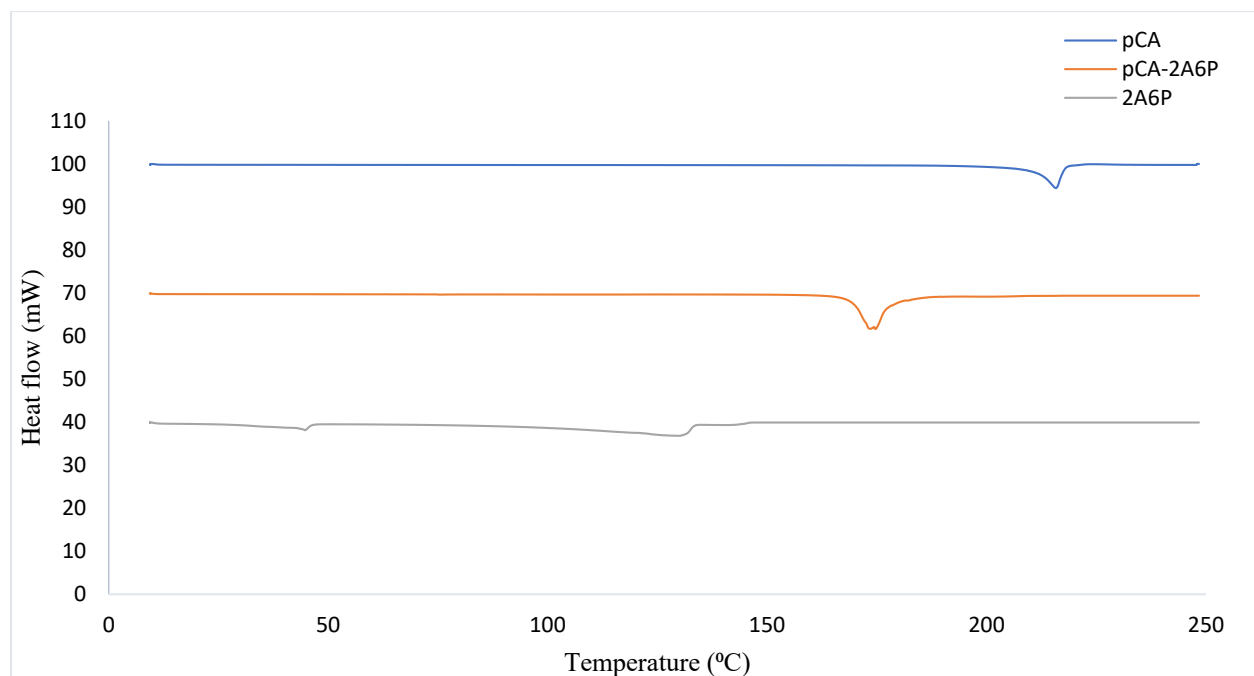Figure 4.21: DSC curve of pCA (blue), 2A4MP (grey) and (pCA$^-$)(2A4MP$^+$) (orange).

63

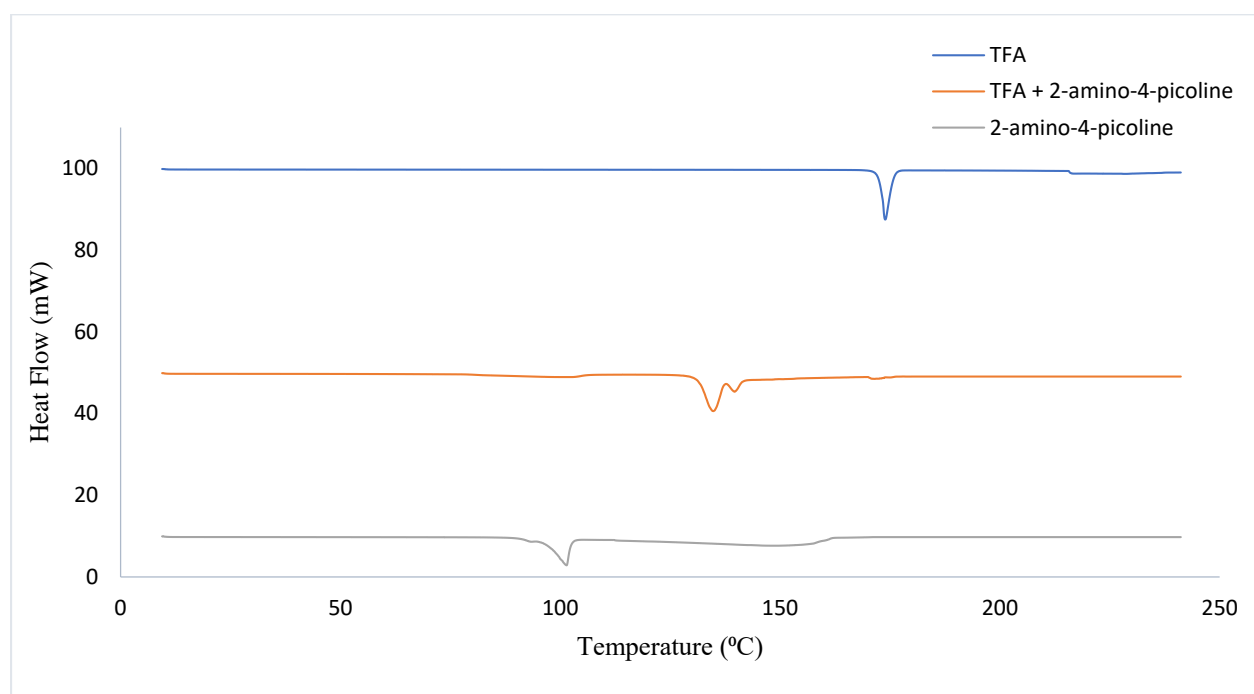Figure 4.22: DSC curve of *p*CA (blue), 2A6MP (grey) and 4(*p*CA⁻)4(2A6MP⁺) (orange).

Figure 4.23: DSC curve of TFA (blue), 2A4MP (grey) and $(TFA^-)(2A4MP^+) \cdot (\frac{3}{2}H_2O)$ (orange).

Table 4.7: Thermal analysis of salts

Salts	$(p\mathrm{CA}^-)(\mathrm{2A4MP}^+)$	$4(p\mathrm{CA}^-)4(\mathrm{2A6MP}^+)$	$(\mathrm{TFA}^-)(\mathrm{2A4MP}^+)\bullet(\frac{3}{2}\,\mathrm{H_2O})$
Stoichiometric ratio	1:1	4:4	$1{:}1{:}\frac{3}{2}$
Melting point peak of salt °C	170	175	134

4.7 FTIR analysis

Upon deprotonation of a carboxylic acid, a carboxylate moiety (COO⁻) is formed. The carboxylate symmetric and antisymmetric stretching modes are typically found in the range 1400 -1600 cm^{-1}. The principal bands were identified and associated changes were recorded. The IR spectrum for pCA which is plotted with its salts (Figure 4.24 and 4.25) shows the presence of the characteristic peak at 3370 cm^{-1} assigned to O-H of the carboxylic acid and 1669 cm^{-1}, assigned to the conjugated carbonyl (COO). The IR spectrum for the $(p\mathrm{CA}^-)(\mathrm{2A4MP}^+)$ salt (Figure 4.24), shows two weak slightly broad bands at 3313-3441cm^{-1} corresponding to the primary amine (NH$_2$) of the co-former that is hydrogen bonded to the carboxylate of pCA. The carboxylic acid OH stretching band is absent, confirming that there is a proton transfer. A shift is observed for the carbonyl group at 1638 cm^{-1} due to hydrogen bonding intermolecular interactions with the amine of the co-former. In Figure 4.25, the IR spectrum of the $4(p\mathrm{CA}^-)4(\mathrm{2A6MP}^+)$ salt is shown. A carboxylic acid O-H peak is shifted to 3000 cm^{-1} for the salt. The carbonyl group is shifted at 1679 cm^{-1} due to the hydrogen bonding intermolecular interactions with the amine of the co-former. In Figure 4.26, the spectra of TFA and $(\mathrm{TFA}^-)(\mathrm{2A4MP}^+)\bullet(\frac{3}{2}\,\mathrm{H_2O})$ salt is shown. Two characteristic peaks are observed for TFA, at 3439 cm^{-1} an O-H stretching band assigned to the carboxylic group of TFA and at 1667 cm^{-1} is the one assigned to the conjugated carbonyl group. Two weak primary amine bands are observed at 3373 cm^{-1} corresponding to the co-former that is hydrogen bonded to the carbonyl group of pCA.
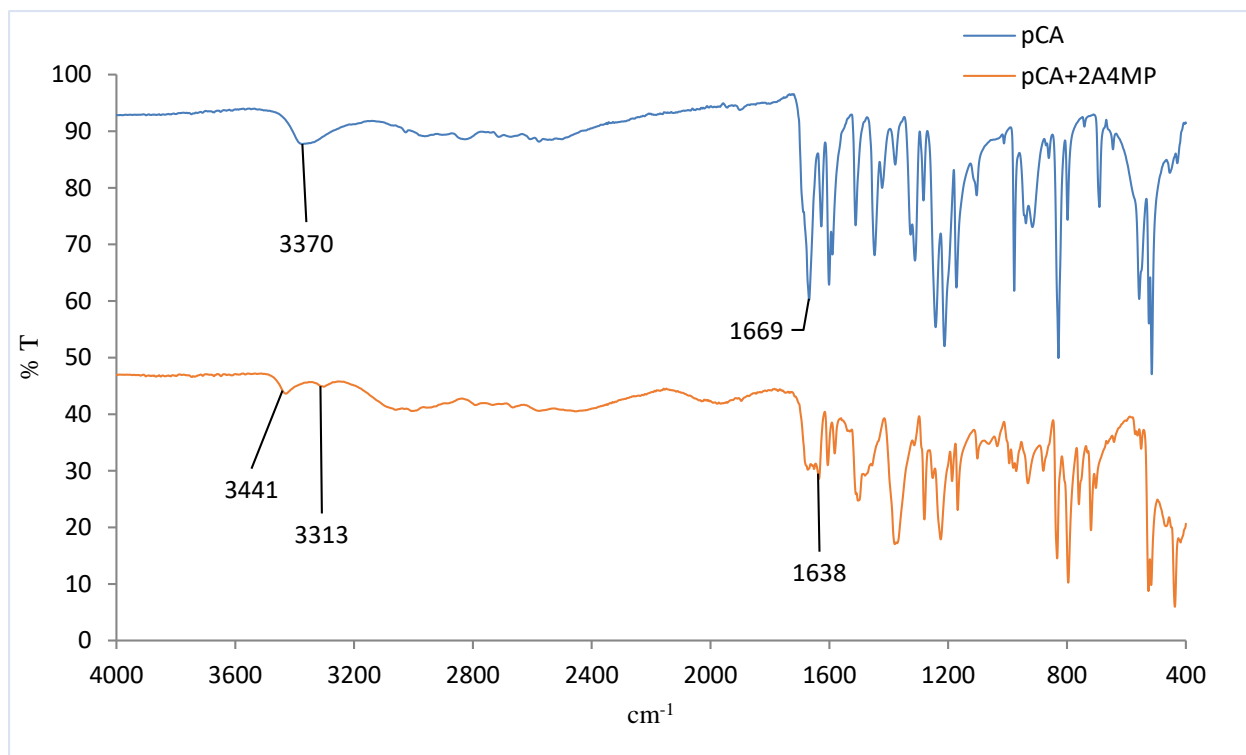
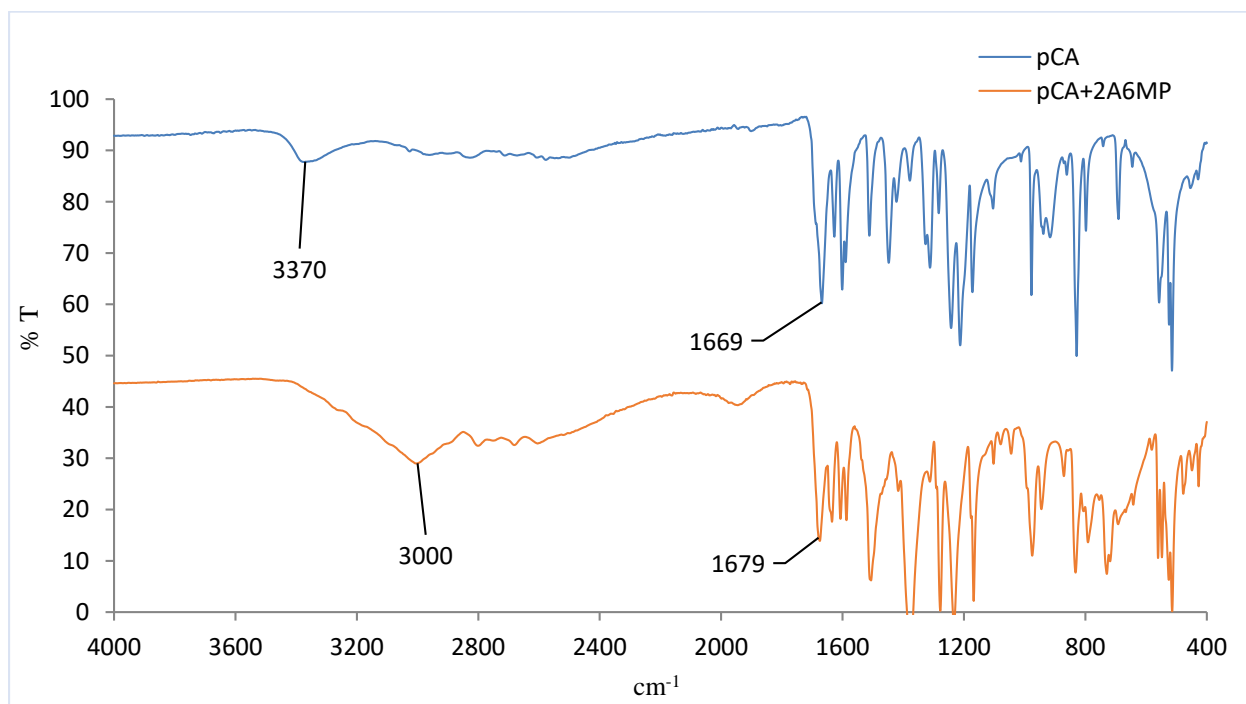Figure 4.24: FTIR spectra of *p*CA (blue) and (*p*CA⁻)(2A4MP⁺) (orange).

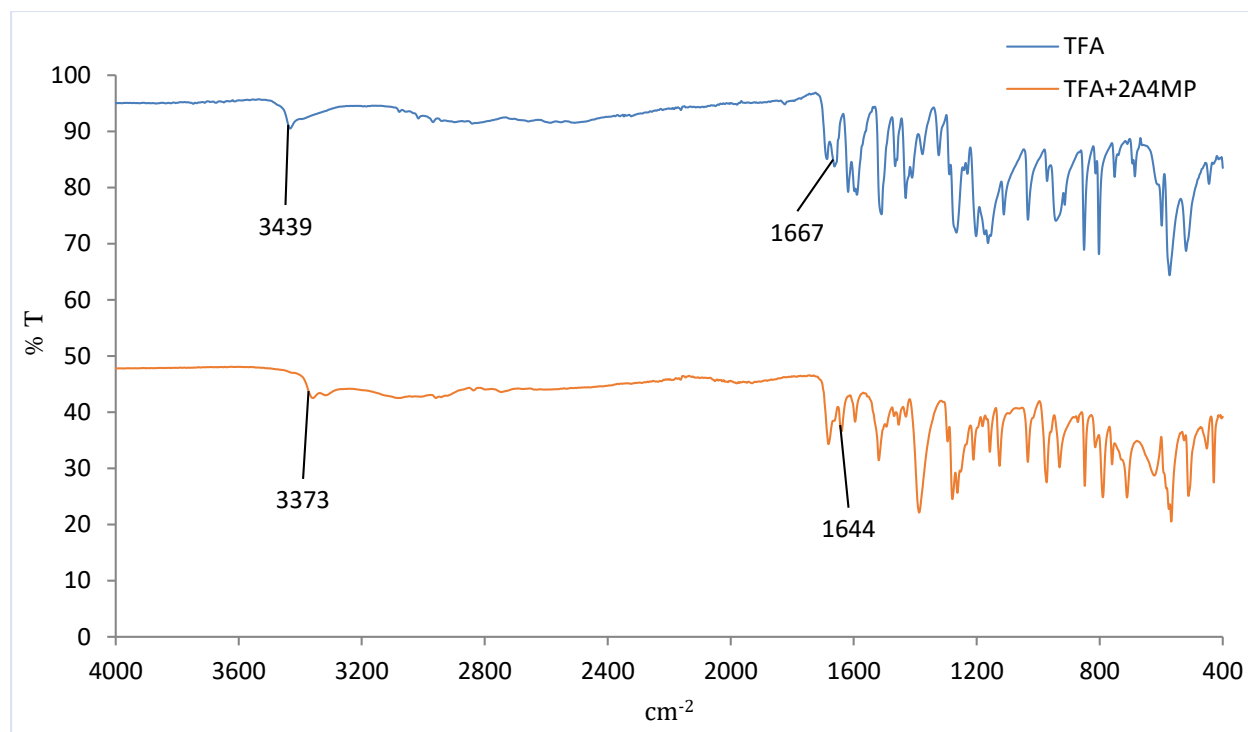Figure 4.25: FTIR spectra of *p*CA (blue) and 4(*p*CA⁻)4(2A6MP⁺) (orange).

Figure 4.26: FTIR spectra of pCA (blue) and $(\text{TFA}^-)(\text{2A4MP}^+)\bullet(\frac{3}{2}\text{H}_2\text{O})$ (orange).

4.8 Conclusion

As predicted by the pK$_a$ rule, pCA formed salts with 2A4MP and 2A6MP while TFA formed a salt only with 2A4MP. All the structures displayed the aminopyridinium carboxylate supramolecular heterosynthon. For the pCA salts the phenol OH hydrogen bonds to the carboxylate. For the TFA salt, water forms a bridge between the phenol OH and the carboxyl group. The methoxy group of TFA did not greatly impact on the formation of the salts. All the salts formed a heterosynthon. For the TFA salt, water bridged molecules of TFA resulting in a 1:1:$\frac{3}{2}$ ratio with 2A4MP while pCA formed a 1:1 ratio salt with 2A4MP and a 4:4 ratio salt with 2A6MP. Both salts of pCA were solved in the orthorhombic $Pbca$ space group and the TFA salt in the monoclinic space group C2/c.

The thermal stability trend as determined by the DSC melting points for the salts is $4(p\text{CA}^-)4(\text{2A6MP}^+) > (p\text{CA}^-)(\text{2A4MP}^+) > (\text{TFA}^-)(\text{2A4MP}^+)\bullet(\frac{3}{2}\text{H}_2\text{O})$.

4.9 References

Bis, J. & Zaworotko, M., 2005. The 2-aminopyridinium-carboxylate supramolecular heterosynthon: a robust motif for generation of multiple-component crystals. *Crystal Growth & Design ,* Volume 5 , pp. 1169-1179.

Cavanagh, K. L., Maheshawri, C. & Rodriguez-Hornedo, N., 2017. Understanding the differences between cocrystal and salt aqueous solubilities. *Elsevier,* Volume 107, pp. 113-120.

Cruz-Cabeza, A., 2012. Acid–base crystalline complexes and the pKa rule. *CrystEngComm,* Volume 14, pp. 6362-6365.

Etter, M., Macdonald, J. & Bernstein, J., 1990. Graph-set analysis of hydrogen bond patterns. *Acta crystallographica,* Volume 46, pp. 256-262.

Macrae, C. et al., 2008 . Mercury CSD 2.0 - New Features for the Visualization and Investigation of Crystal Structures. *J. Appl. Cryst,* Volume 41, pp. 466-470.

Sheldrick, G. M. , 1997. Program for the Refinement of Crystal Structures from Diffraction Data. University of Göttingen, Göttingen, Germany.

Yvon, K., Jeitschko, W. & Parthe, E. J., 1997. LAZY PULVERIX, a computer program, for calculating X-ray and neutron diffraction powder patterns. *Appl.Cryst,* Volume 10, pp. 73-74.

CHAPTER 5: SOLVATES OF *p*-COUMARIC ACID AND *trans*-FERULIC ACID

5.1 Introduction

Solvates are crystalline materials that incorporate solvent molecules in their crystal lattice. If the included solvent is water, the resulting solid is a hydrate. Solvates or hydrates are important in the manufacturing and processing of drugs as they alter their physicochemical properties (Surov, *et al*., 2015). The benefit of studying solvates is that undesirable solvates obtained during the process of purification and formulation of the API due to the exposure to solvents can be controlled. In this chapter, the focus is on the preparation and characterisation of *p*-coumaric acid and *trans*-ferulic acid solvates. Various solvents were used in the co-crystallisation experiments however, only two solvents formed solvates with the acids. *p*CA formed solvates with 1,4-dioxane (DX) and pyridine (PYR) whereas TFA only formed a solvate with DX. The molecular structures of DX and PYR are shown in Figure 5.1.
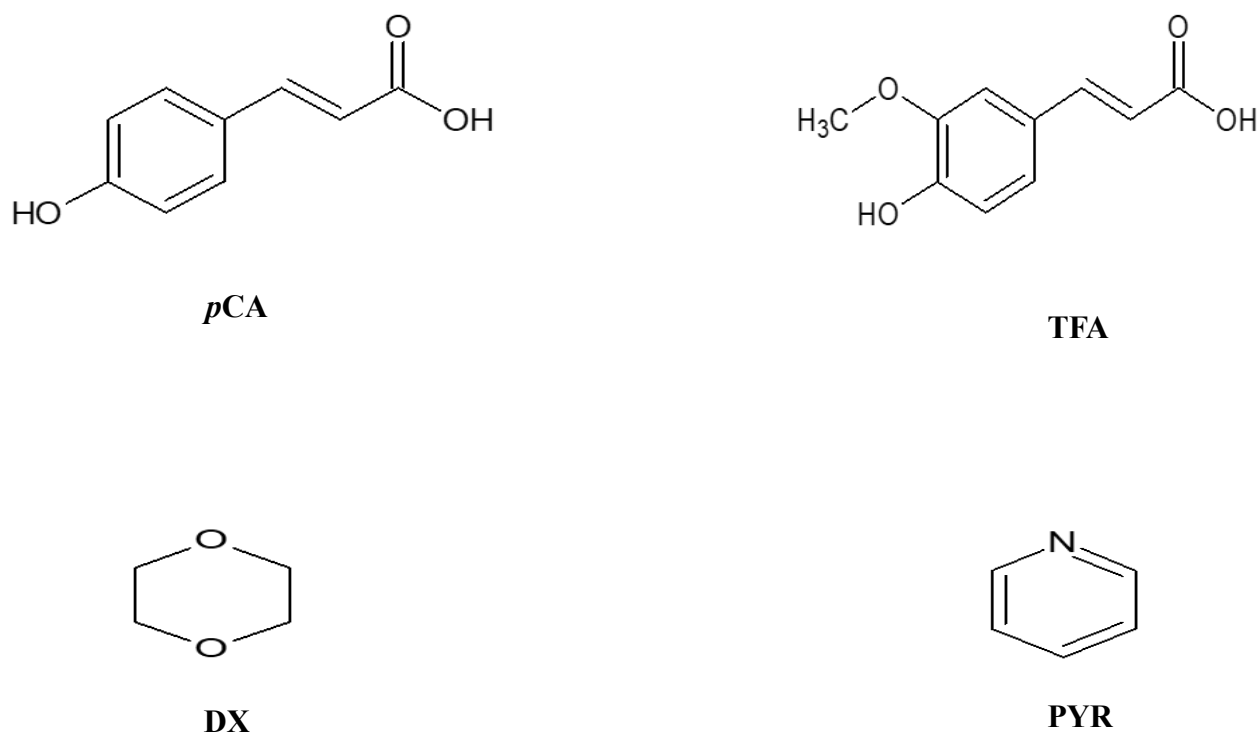

pCA

TFA

DX

PYR

Figure 5.1: Chemical structures used in this study.

5.2 Structural analysis of *p*-coumaric acid and *trans*-ferulic acid solvates

The compounds formed block-like crystals with different colours. Yellow crystals were observed for (*p*CA)•($\frac{1}{2}$DX) and 2*p*CA•2PYR solvates, whereas (TFA)•($\frac{1}{2}$DX) displayed colourless crystals. The structures were solved using direct methods with SHELXS-97 (Sheldrick, 1997). The crystal data is summarised in Table 5.1.

Table 5.1: Crystal data and refinement parameters of *p*CA and TFA solvates

Compound	(TFA)•($\frac{1}{2}$DX)	(*p*CA)•($\frac{1}{2}$DX)	2*p*CA•2PYR
Molecular formula	$C_{12}H_{14}O_5$	$C_{11}H_{12}O_4$	$C_{28}H_{26}N_2O_6$
M_r (g/mol)	237.23	208.21	486.51
Temperature (K)	173	173	173
Crystal system	Triclinic	Monoclinic	Orthorhombic
Space group	$P\bar{1}$	$P2_1/n$	*Pbca*
a (Å)	7.1405(14)	7.2450(14)	7.6983(15)
b (Å)	7.4221(15)	5.8712(12)	23.701(5)
c (Å)	11.830(2)	24.419(5)	26.655(5)
α (°)	79.44(3)	90	90
β (°)	86.14(3)	94.58(3)	90
γ (°)	68.28(3)	90	90
V (Å^3)	572.6(2)	1035.4(4)	4863.4(17)
Z	2	4	8
ρ (calcd) (g/cm^3)	1.382	1.336	1.329
Absorption coefficient μ (mm^{-1})	0.108	0.102	0.094
$2\theta_{max}$ (°)	56.5	55.1	55.9
Reflections collected	11209	13435	29508
No. data with $I > 2\sigma(I)$	2425	1903	3835
No. parameters	169	166	329
Final R ($I > 2\sigma(I)$)	R$_1$=0.0398; wR$_2$= 0.1438	R$_1$= 0.0512; wR$_2$= 0.1297	R$_1$= 0.0467; wR$_2$= 0.1306
R indices (all data)	R$_1$=0.0462; wR$_2$= 0.1514	R$_1$= 0.0636; wR$_2$= 0.1379	R$_1$= 0.0814; wR$_2$= 0.1592
Goodness-of-fit on F^2	1.214	1.062	0.941
Min, max e$^-$ density (e Å^{-3})	-0.275, 0.426	-0.407, 0.480	-0.225, 0.237

5.2.1 Solvate of *p*-coumaric acid with 1,4-dioxane, *p*CA•$\frac{1}{2}$DX

Yellow single crystals were obtained after a day of slow evaporation of *p*CA in DX with ethanol as a co-solvent. A single crystal taken from the bulk was analysed using single crystal X-ray diffraction and the structure was solved successfully in the monoclinic space group *P2₁/n*. The asymmetric unit comprises one molecule of *p*CA and half of a DX molecule, Figure 5.2. The 1,4-dioxane lies on a special position at Wyckoff position *d*. From the structural analysis, it was observed that the oxygen atom of DX is disordered over two positions with site occupancies of 0.69607 and 0.3093. The structure is characterised by the carboxylic acid homosynthon d(O2-O1) = 2.641(2) Å and an OH•••O interaction between *p*CA and DX with d(O3-O4A) = 2.612(11) Å, Figure 5.3. The geometrical data for the hydrogen bonds of *p*CA•$\frac{1}{2}$DX are summarised in Table 5.2.

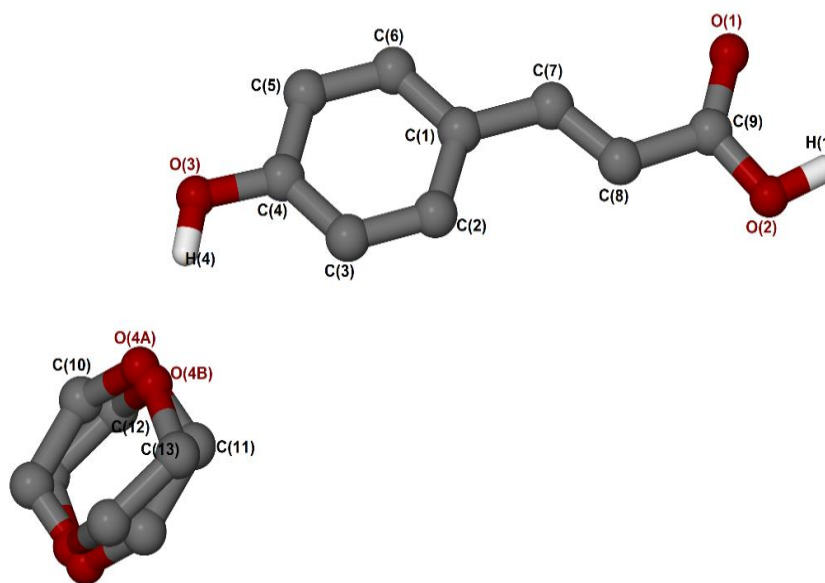
Figure 5.2: Numbering scheme of the asymmetric unit of *p*CA•$\frac{1}{2}$DX with some hydrogen atoms omitted for clarity.

The DX molecule adopts the chair conformation in the crystal structure, which is the most stable conformation, with oxygens in the DX molecule being *trans* to each other (see Figure 5.2.). An alternating arrangement of the *p*CA dimer with DX is observed in the packing diagram of the *p*CA$\cdot\frac{1}{2}$DX solvate along [100], shown in Figure 5.4. The carboxylic acid homosynthon forms $R_2^2(8)$ rings and *p*CA and DX molecules form zigzag $C_3^3(25)$ chains (Etter, et al., 1990).
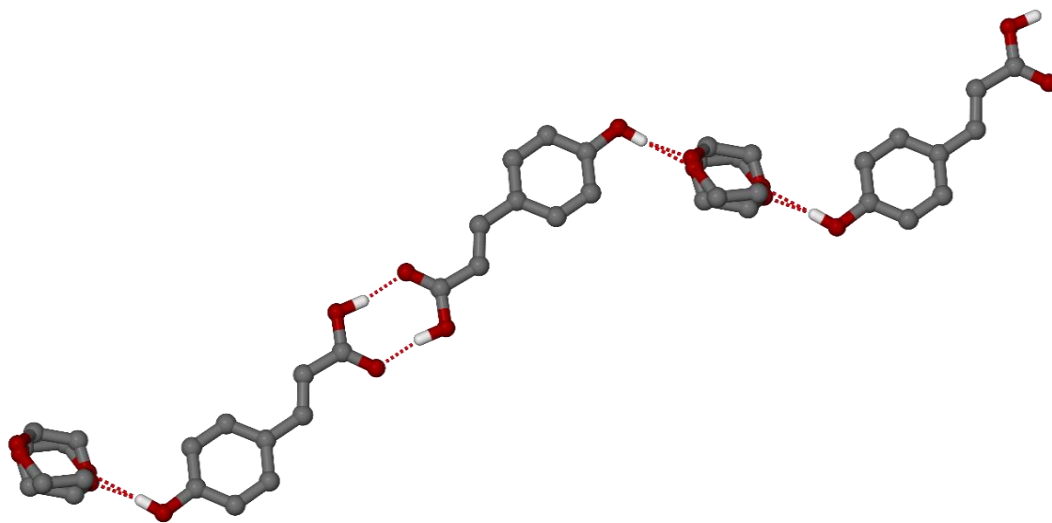

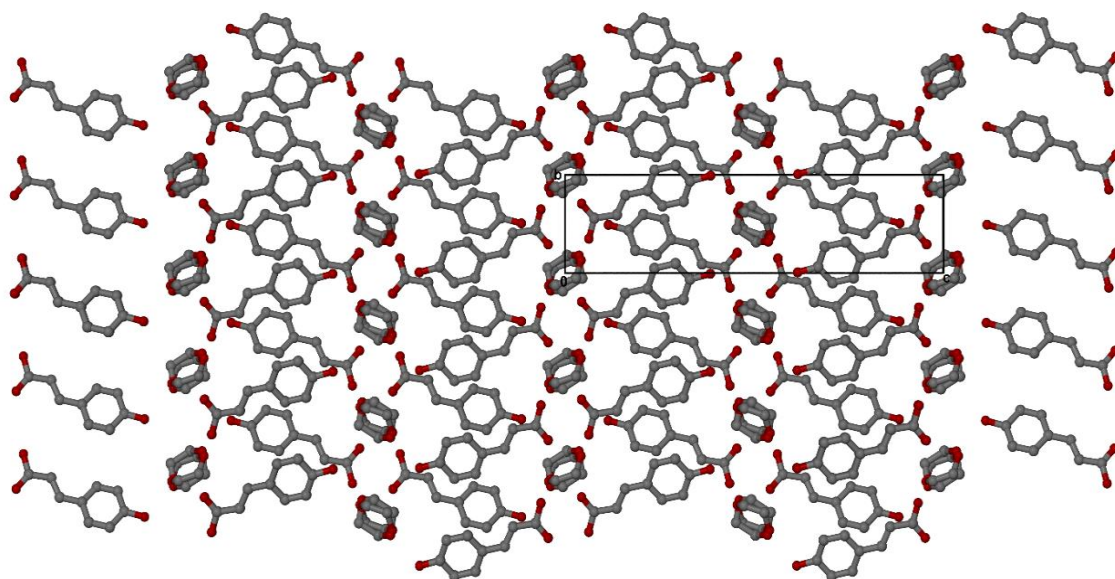Figure 5.3: Schematic diagram of the hydrogen bonding in *p*CA$\cdot\frac{1}{2}$DX solvate

Figure 5.4: Packing diagram of pCA•$\frac{1}{2}$DX along [100] with hydrogen atoms omitted.

Table 5.2: Geometrical data for hydrogen bonds of pCA•$\frac{1}{2}$DX

	D-H (Å)	H•••A (Å)	D•••A (Å)	<DHA (º)	Symmetry operation
O3-H4•••O5B	0.84	1.97	2.810(2)	172.0	
O3-H4•••O4A	0.84	1.79	2.612(1)	165.3	
O2-H1•••O1	0.95	1.70	2.641(2)	169.2	-x, -y+1, -z

5.2.2 Solvate of p-coumaric acid with pyridine 2pCA•2PYR

A concentrated solution of pCA in pyridine gave brown single crystals after 2 months via the solvent evaporation technique. The crystal structure was solved and refined in the orthorhombic space group *Pbca*. No proton transfer was found and this correlates with the ΔpK_a = (pK_{acid} − pK_{base}) = 1.11, which falls in the region where there is a probability of a co-crystal or a salt (Cruz-Cabeza, 2012). In this case no proton transfer was observed. The crystal structure comprises two pyridine molecules and two p-coumaric acid molecules in the asymmetric unit, Figure 5.5. Two major interactions are present, O-H•••O and O-H•••N, Figure 6. Again, the

carboxylic acid homosynthon is observed with d(O5-O1) = 2.638(2) and d(O2-O4) = 2.630(2). The 2pCA•2PYR also forms a carboxylic acid homosynthon with $R_2^2(8)$ rings, Figure 5.6. The hydrogen bonds data are summarised in Table 5.3.
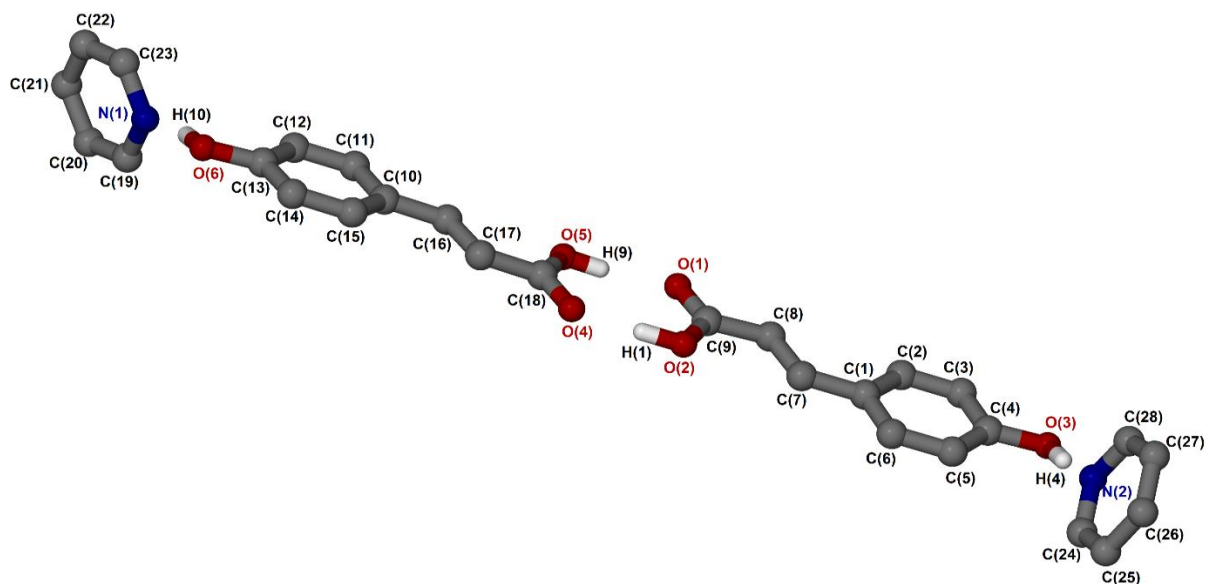

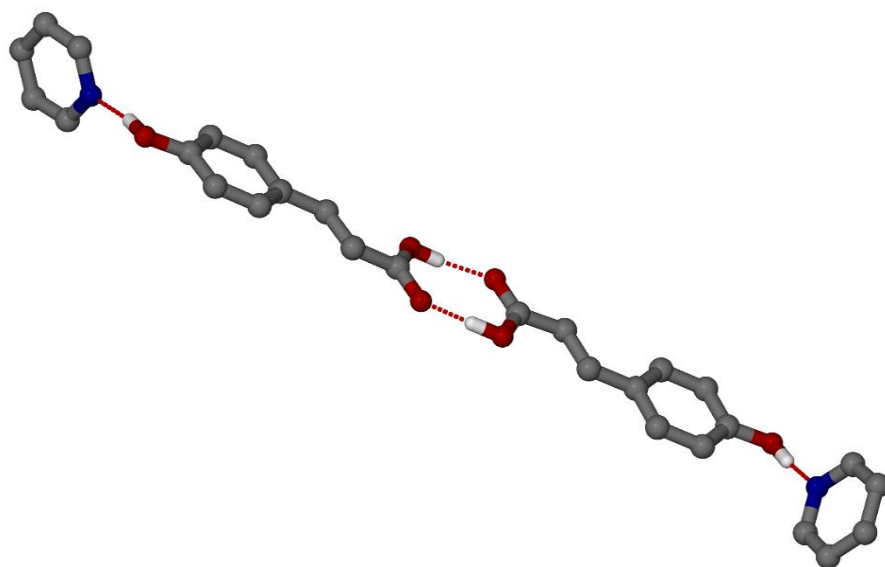Figure 5.5: Numbering scheme of the asymmetric unit of 2pCA•2PYR with some hydrogen atoms omitted for clarity.

Figure 5.6: Hydrogen bond diagram of 2pCA•2PYR

In the 2pCA•2PYR solvate, the pCA molecules are arranged in columns parallel to each other with the PYR molecules alternating between these columns. The PYR molecules are involved in π•••π stacking with d(Cg-Cg) = 3.903 Å. The packing has a wave-like shape, Figure 5.7.
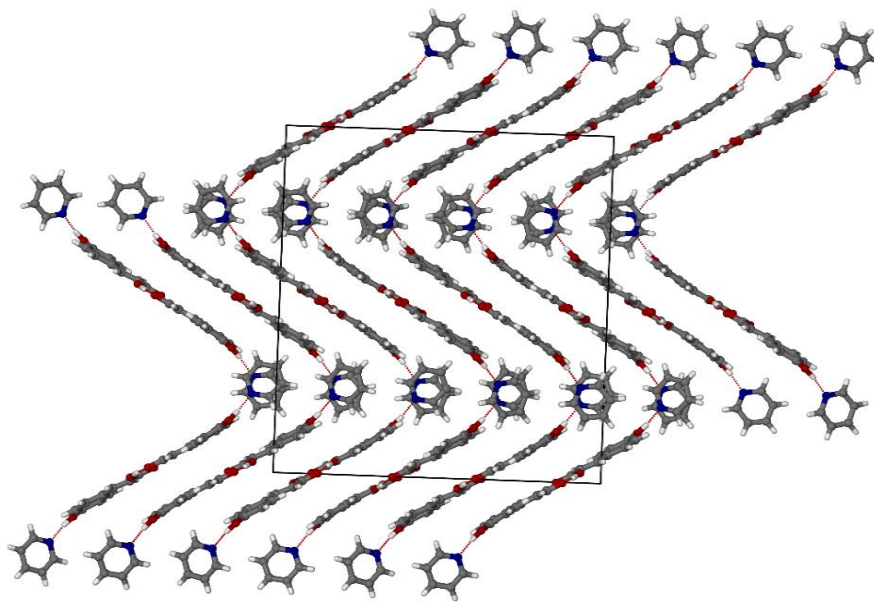

Figure 5.7: Packing diagram of 2pCA•2PYR along [010] with hydrogen bonds indicated.

Table 5.3: Geometrical data for hydrogen bonds of 2pCA•2PYR

	D-H (Å)	H•••A (Å)	D•••A (Å)	<DHA (º)
O2-H1•••O4	0.95	1.68	2.630(2)	171.7
O5-H9•••O1	0.87	1.77	2.638(2)	174.8
O3-H4•••N2	0.96	1.83	2.783(2)	173.1
O6-H10•••N1	0.95	1.79	2.739(2)	170.3

5.2.3 Solvate of *trans*-ferulic acid with 1,4-dioxane (TFA)•($\frac{1}{2}$DX)

Colourless single crystals were obtained after a day of slow evaporation. (TFA)•($\frac{1}{2}$DX) crystallised in the triclinic space group $P\bar{1}$ with one molecule of *trans*-ferulic acid and a half molecule of 1,4-dioxane in the asymmetric unit, Figure 5.8.

The carboxylic acid hydrogen is disordered over two positions with site occupancy of 0.53725 and 0.46275, This is reflected in the C-O bond distances of d(C9-O1) = 1.280 Å and d(C9-O2) = 1.271 Å.
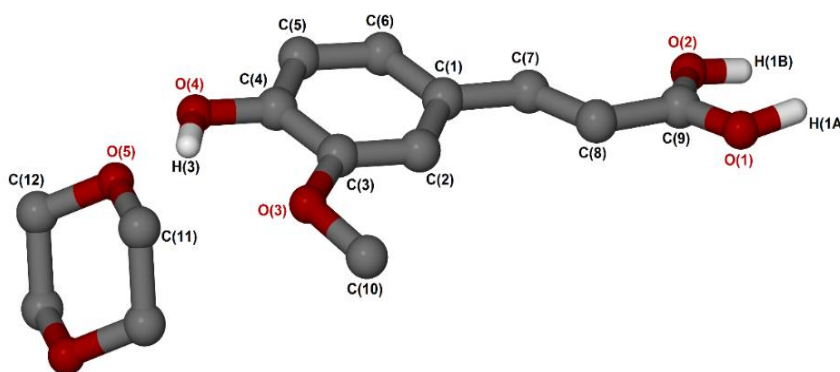

Figure 5.8: Numbering scheme of the asymmetric unit of (TFA)•($\frac{1}{2}$DX) with some hydrogen atoms omitted for clarity.

In Figure 5.9, the hydrogen bonding pattern of the $(TFA) \bullet (\frac{1}{2}DX)$ solvate is shown. TFA occupies general positions and 1,4-dioxane is situated on a centre of inversion. The oxygen atom of 1,4-dioxane formed an O-H•••O hydrogen bond with the hydroxyl group of TFA, d(O4-O5) = 2.708(1) Å. The carboxylic acid homosynthon persists with d(O1-O2) = 2.616(1) Å. Some weak C-H•••O hydrogen bonds were also observed with d(C11-O3) = 3.335(2) Å. The hydrogen bond data for $(TFA) \bullet (\frac{1}{2}DX)$ solvate is summarised in Table 5.4.

Figure 5.9: Hydrogen bonding of $(TFA) \bullet (\frac{1}{2}DX)$ with some hydrogen atoms omitted for clarity.

The packing of $(TFA) \bullet (\frac{1}{2}DX)$ solvate along [010] depicted in Figure 5.10, shows columns of TFA molecules alternating with DX molecules. There are π•••π stacking interactions between TFA molecules with d(Cg-Cg) = 3.581 Å. The carboxylic acid homosynthon also forms $R_2^2(8)$ rings with TFA and DX molecules forming zigzag $C_3^3(25)$ chains. This structure was compared to that of pCA•$\frac{1}{2}$DX using Mercury (Macrae et. al., 2008) but no packing similarity was found.

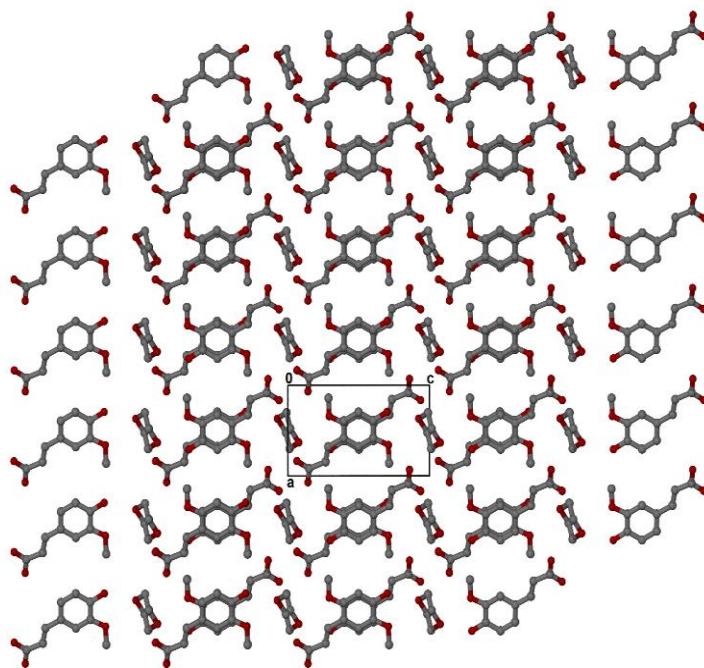Figure 5.10: Packing diagram of (TFA)•($\frac{1}{2}$DX) along [010] with hydrogen atoms omitted.

Table 5.4: Geometrical data for hydrogen bonds of (TFA)•($\frac{1}{2}$DX)

	D-H (Å)	H•••A (Å)	D•••A (Å)	<DHA (º)	Symmetry operation
O4-H3•••O5	0.90(2)	1.90(2)	2.708(1)	148(2)	
C11-H11B•••O3	0.99	2.88	3.335(2)	109.1	
C12-H12A•••O4	0.99	3.09	3.396(2)	99.6	
O1-H1A•••O2	0.98(2)	1.64	2.616(1)	172(3)	-x+2, -y+2, -z
C11-H11B•••O2	0.99	3.00	3.228(2)	94.3	-x+1, -y+2, -z+1
C12-H12A•••O2	0.99	2.96	3.619(2)	124.9	-x+1, -y+1, -z+1
C10-H10B•••O1	0.98	3.00	3.499(2)	112.6	-x+2, -y+2, -z+1

5.3 Torsion angles

The same torsion angles as described previously were considered for *p*CA and TFA (Figure 5.11). The molecule of *p*CA formed solvates with PYR and DX while TFA formed a solvate with DX only. Small variations were found in the ring twist torsion angle, τ_1 for the three solvate structures. Significant differences were observed in the carboxylic acid twist torsion angle (τ_2) with the 2*p*CA•2PYR displaying a *trans* conformation of the carbonyl group relative to the alkene group. The other two solvate structures showed a *cis* conformation. The torsion angles are summarised in Table 5.5.
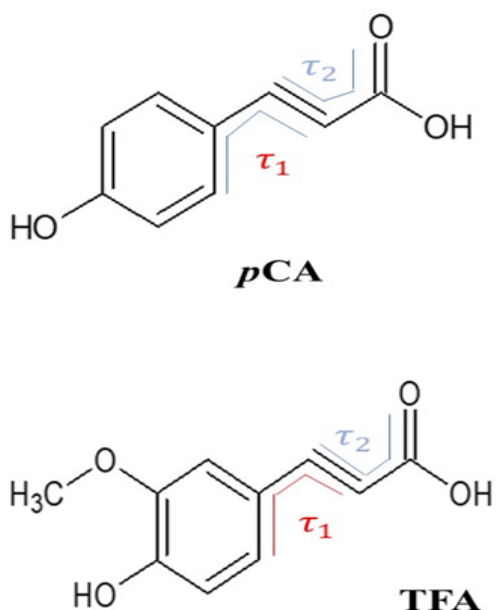

Figure 5.11: Torsion angles of solvates of *p*CA and TFA

Table 5.5: Torsion angles of solvates of *p*CA•$\frac{1}{2}$DX, 2*p*CA•2PYR and (TFA)•($\frac{1}{2}$DX)

	*p*CA•$\frac{1}{2}$DX	2*p*CA•2PYR	(TFA) • ($\frac{1}{2}$DX)
Torsion angle	(°)	(°)	(°)
τ_1(C2-C1-C7-C8)	6.6	4.0	8.1
τ'_1(C15-C10-C16-C17)	-	4.7	-
τ_2(C7-C8-C9-O1)	0.3	176.1	6.9
τ'_2(C16-C17-C18-O4)	-	179.4	-

5.4 Hirshfeld surface analysis of pCA•$\frac{1}{2}$DX, 2pCA•2PYR and TFA•$\frac{1}{2}$DX

The fingerprint plot for pCA in pCA•$\frac{1}{2}$DX is shown in Figure 5.12 and for the two molecules of pCA in 2pCA•2PYR see Figure 5.13 and 5.14. The plot for TFA in TFA•$\frac{1}{2}$DX is depicted in Figure 5.15. As observed previously, C-H, H-H, and O-H are the dominating contacts in the solvates of pCA and TFA. The molecular stacking π•••π represented by C•••C is one of the lowest contributing contacts with 1.4 % for pCA in the pCA•$\frac{1}{2}$DX solvate (Figure 5.12b), 2.5 % and 4.4 % for pCA in 2pCA•2PYR solvate (Figure 5.13b and 5.14b respectively) and 6.8 % for TFA in the TFA•$\frac{1}{2}$DX solvate (Figure 5.15b). The Hirshfeld surface area analysis revealed that the solvates are strongly stabilised by hydrogen bonding. For pCA•$\frac{1}{2}$DX solvate, the O-H contact contributes 27 % and can be assigned to the O-H•••O hydrogen bonding, Figure 5.12e. For the 2pCA•2PYR solvate, the two major hydrogen bonding is of the form O-H•••N and O-H•••O. These are depicted as % N-H with the contribution of 4.2 % and 3.6 % (Figure 5.13e and 5.14e respectively) and O-H contributing 31.3 % for each pCA in the asymmetric unit (Figure 5.13f and 5.14f respectively). The TFA•$\frac{1}{2}$DX solvate has strong hydrogen bonding, O-H•••O and weak hydrogen bonding C-H•••O. The O-H contact contributes 31.9 % and it is assigned to strong and weak hydrogen bonding, Figure 5.15e. The quantitative summary of various interactions of pCA and TFA are shown in Table 5.6.

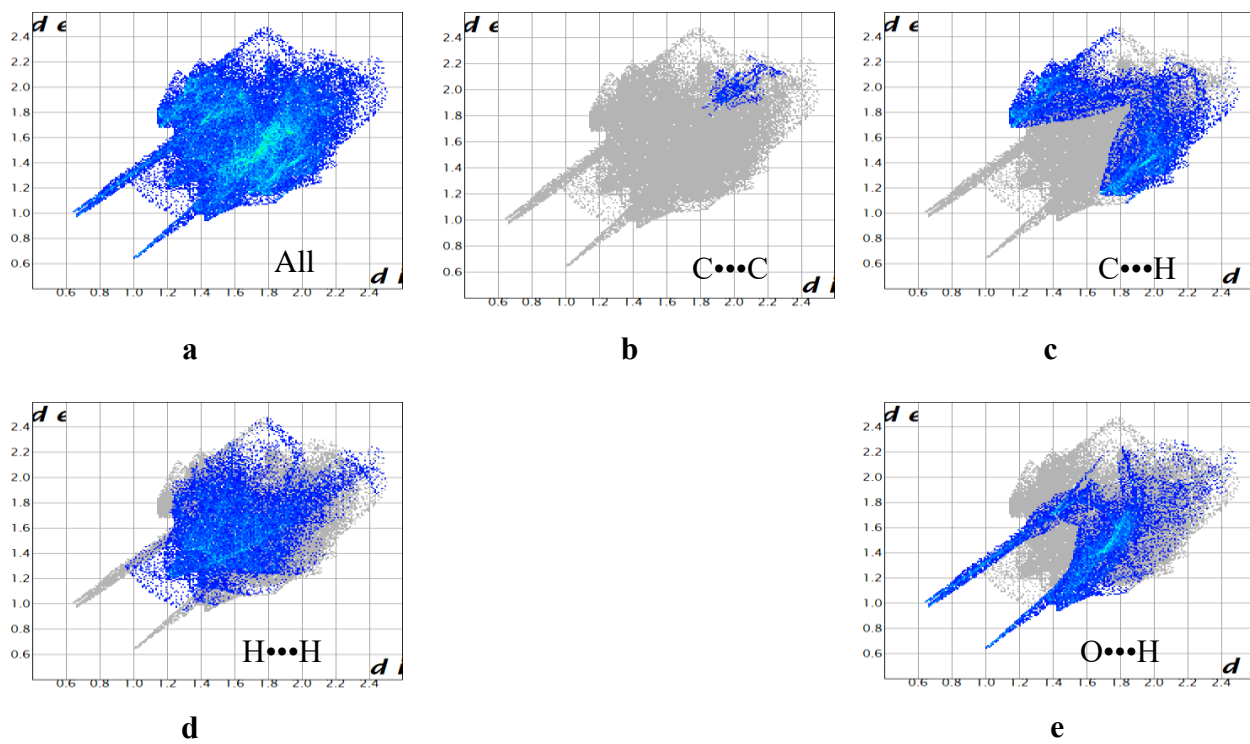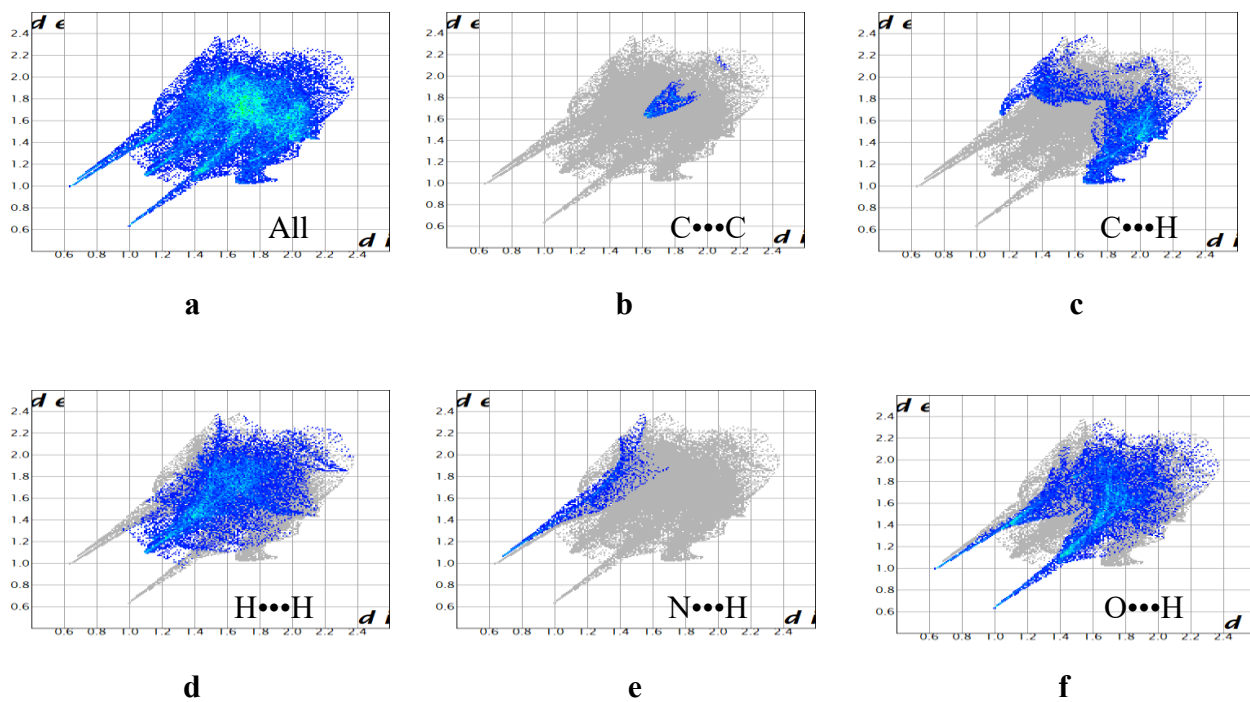Figure 5.12: Fingerprint plot of pCA in the pCA$\cdot\frac{1}{2}$DX salt with the main interactions shown.

Figure 5.13: Fingerprint plot of pCA in the 2pCA$\cdot$2PYR salt with the main interactions shown.
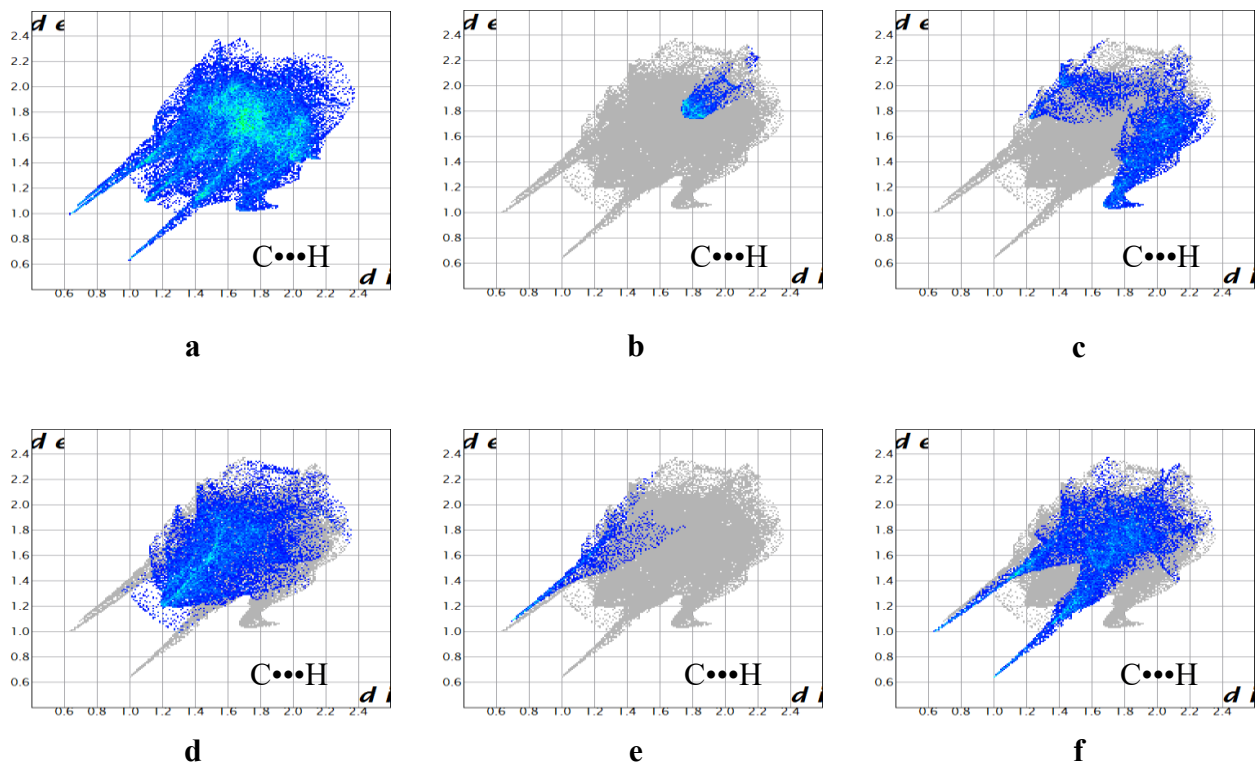
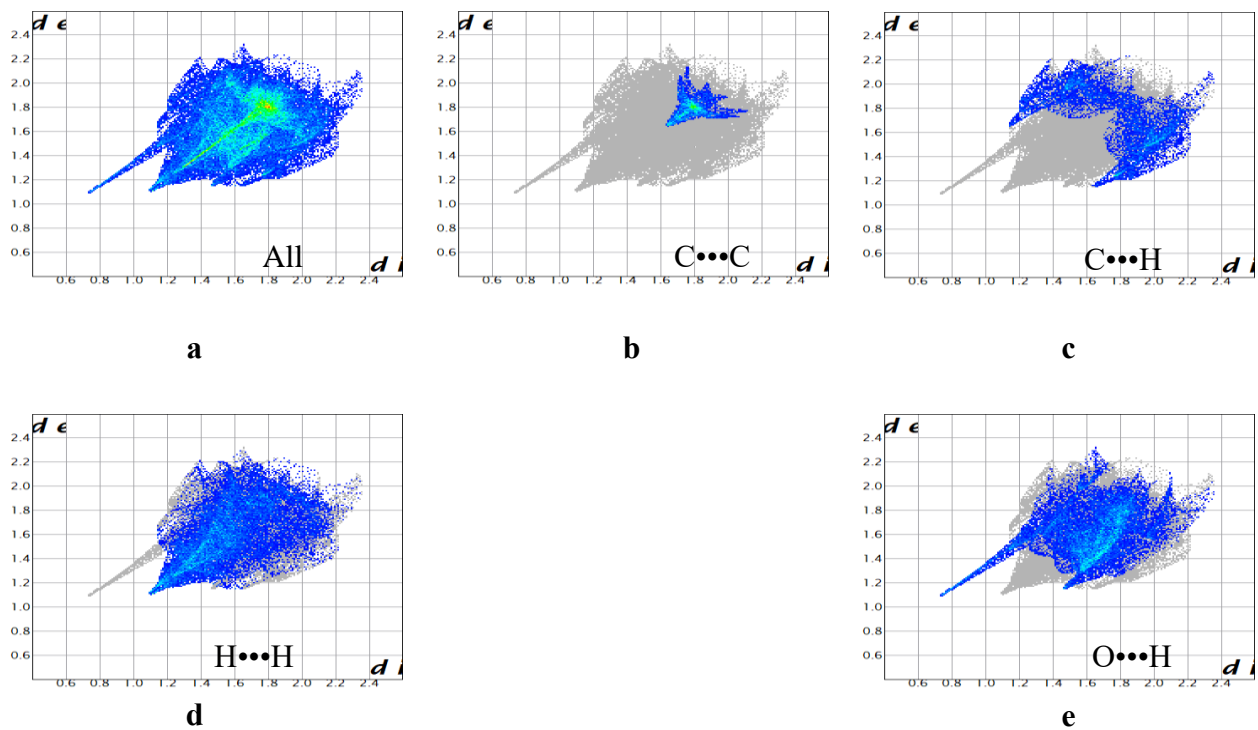Figure 5.14: Fingerprint plot of *p*CA in the 2*p*CA•2PYR′ salt with the main interactions shown

Figure 5.15: Fingerprint plot of TFA in the TFA• $\frac{1}{2}$ DX salt with the main interactions shown.

Table 5.6: Quantitative summary of the various interactions of *p*CA and TFA solvates

Compounds	C•••C (%)	C•••H (%)	H•••H (%)	N•••H (%)	O•••H (%)
*p*CA•$\frac{1}{2}$DX	1.4	30.3	37.6	-	27
2*p*CA•2PYR	2.5	21	36.1	4.2	31.3
	4.4	19.7	36.5	3.6	31.3
TFA•$\frac{1}{2}$DX	6.8	16.2	36	-	31.9

5.5 PXRD analysis of the (TFA)•($\frac{1}{2}$DX) solvate

PXRD analysis was conducted to determine whether the crystal prepared via the slow evaporation technique could be reproduced by the grinding technique. The PXRD patterns for the single crystals were calculated using LAZY PULVERIX (Yvon, *et al*., 1977). The grinding experiments were unsuccessful for the preparation of 2*p*CA•2PYR and *p*CA•$\frac{1}{2}$DX and resulted in the starting material (Figure 5.16 and Figure 5.17). The grinding experiment involving TFA and DX gave a mixture of the starting material, TFA•$\frac{1}{2}$DX solvate and an unknown product (Figure 5.18).
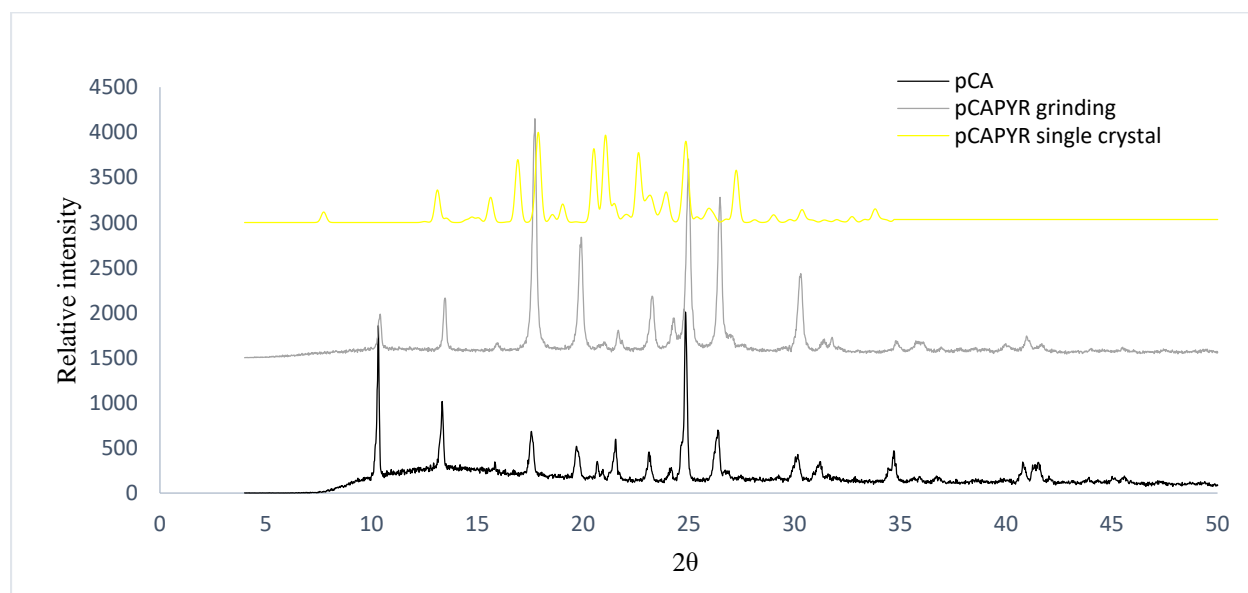

Figure 5.16: PXRD of analyses of 2*p*CA•2PYR, the LAZY PULVERIX calculated pattern in yellow, the grinding experiment in grey and black is the starting material *p*CA.
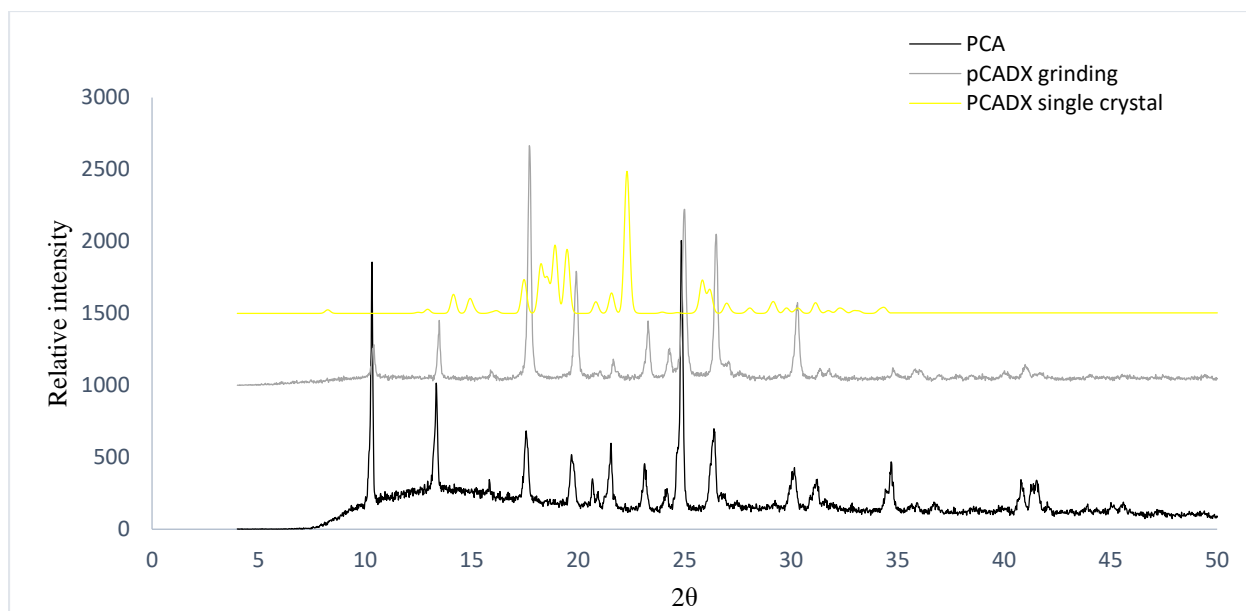
Figure 5.17: PXRD of analyses of pCA•$\frac{1}{2}$ DX, the LAZY PULVERIX calculated pattern in yellow, the grinding experiment in grey and black is the starting material pCA.
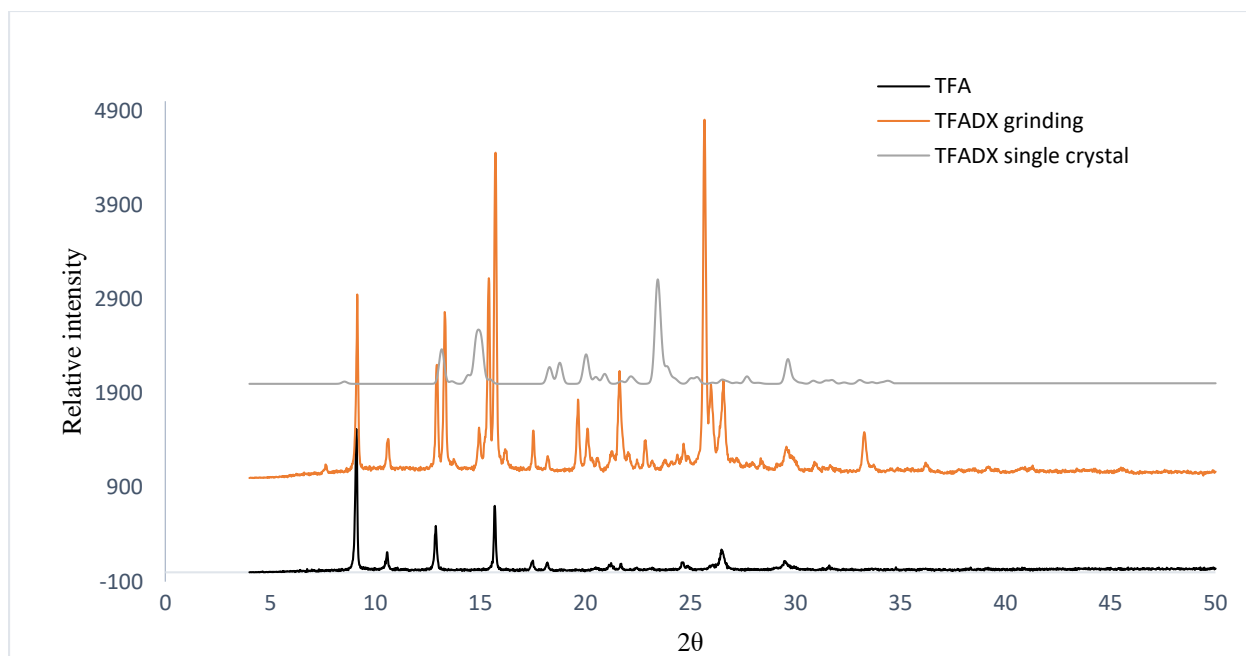

Figure 5.18: PXRD analyses of TFA•$\frac{1}{2}$ DX, the LAZY PULVERIX calculated pattern in grey, the grinding experiment in orange and black is the starting material TFA.

## 5.6 Thermal analysis of the pCA and TFA solvates

The TGA and DSC curves are shown in Figure 5.19. Single step mass losses were obtained for the loss of solvent from the solvates and the experimental values correlate with the calculated ones. The thermal analysis results are summarised in Table 5.7. Two endothermic peaks on the DSC curves were observed. The first one corresponds to the release of solvents; for (a) the release of DX at 87 °C in pCA•$\frac{1}{2}$DX, (b) the release of PYR at 73 °C in 2pCA•2PYR and (c) the release of DX at 105 °C in TFA•$\frac{1}{2}$DX. The second DSC peaks depict the melting point of pCA in (a) and (b) at 224 and 220 °C respectively, and the melting point of TFA in (c) at 175 °C. For all the solvates, the loss of solvent takes place at a lower temperature than the boiling point of the respective solvent. This is in agreement with the location of the 1,4-dioxane molecules in channels for TFA•$\frac{1}{2}$DX and pCA•$\frac{1}{2}$DX, with the pyridine molecules in layers for 2pCA•2PYR (Figure 5.20). The thermal stability is TFA•$\frac{1}{2}$DX > pCA•$\frac{1}{2}$DX > 2pCA•2PYR and this is confirmed with the T_{peak}/T_b (Gokel & Barbour, 2017) that are 1.04, 0.86 and 0.63 respectively. The thermal stability can also be correlated to the hydrogen bonding with 2pCA•2PYR displaying a single moderate hydrogen bond between pCA and PYR compared to the two interactions between the acids and DX.

Table 5.7: Thermal analysis data of the solvates

Solvates	pCA•$\frac{1}{2}$DX	2pCA•2PYR	TFA•$\frac{1}{2}$DX
Stoichiometric ratio	1: ½	1:1	1: ½
TGA calc % mass loss	21.1	29.1	18.5
Exp % mass loss	19.2	27	18
T_{peak} for solvent loss, °C	87	73	105
T_{peak} for pCA melting, °C	224	220	-
T_{peak} for TFA melting, °C	-	-	175
Normal boiling point of solvents, °C	101	115	101
Normal melting point of pCA, °C	214		
Normal melting point of TFA, ºC			194
T_{peak}/T_b	0.86	0.63	1.04
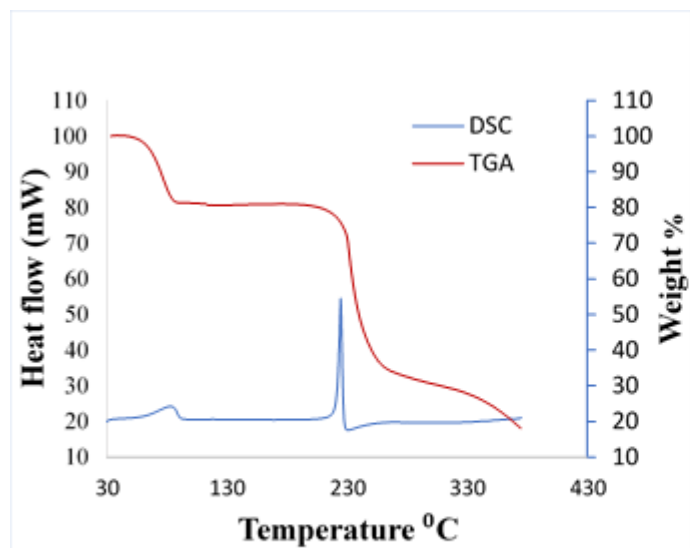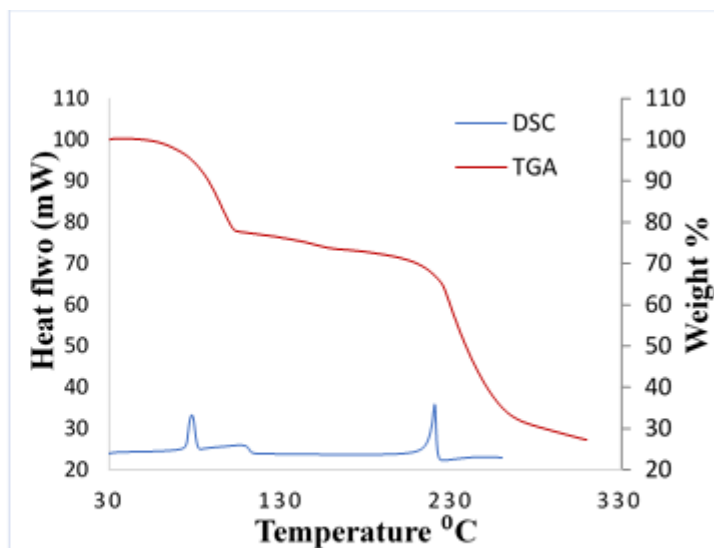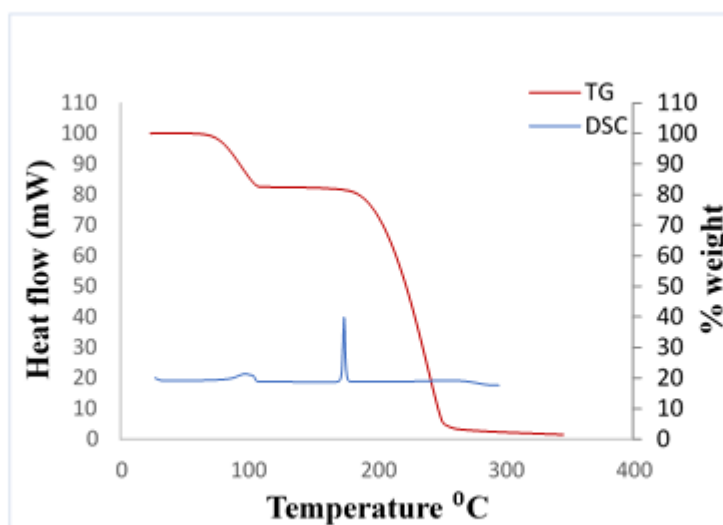
Figure 5.19: DSC and TGA curves of *p*CA solvates and the TFA solvate, DSC curves (blue) and TGA (red) with $p\text{CA} \cdot \frac{1}{2}\text{DX}$ solvate (a), $2p\text{CA} \cdot 2\text{PYR}$ solvate (b) and $\text{TFA} \cdot \frac{1}{2}\text{DX}$ solvate (c).
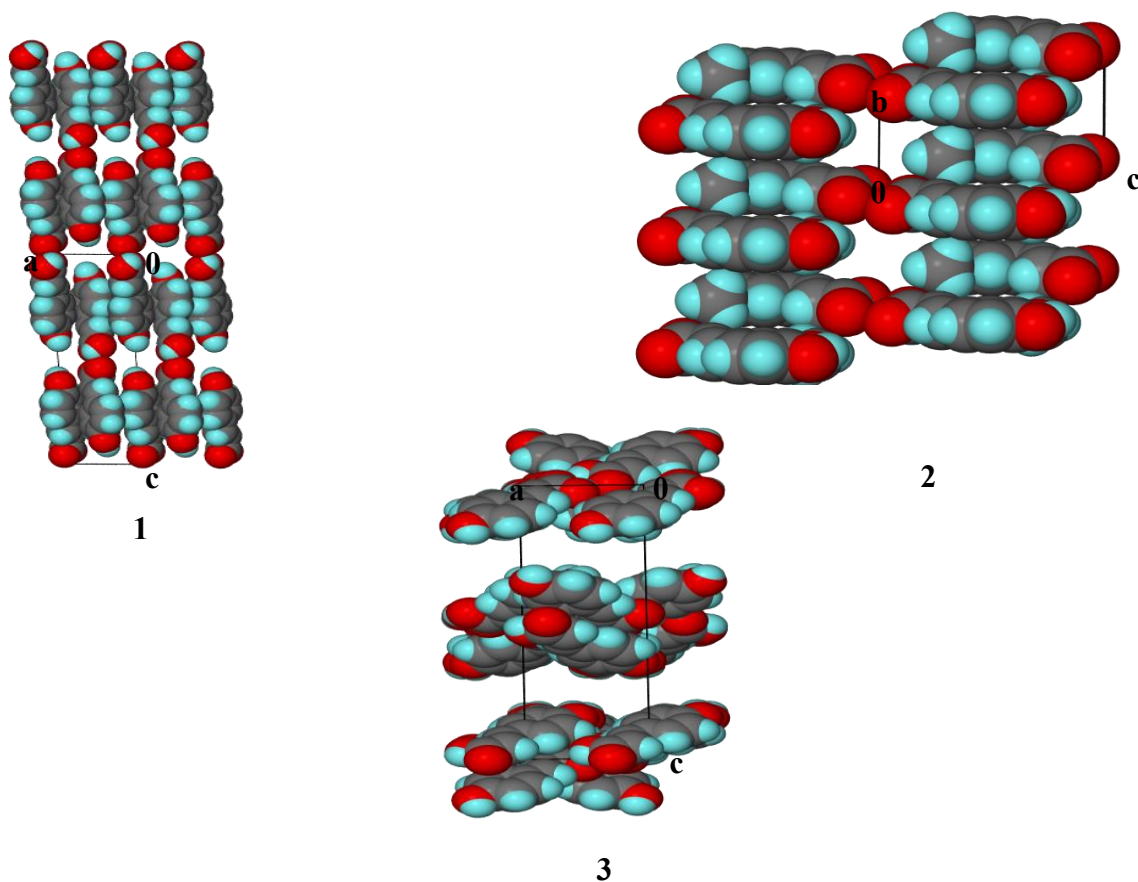
Figure 5.20: Packing diagrams showing the location of DX in pCA$\bullet\frac{1}{2}$DX (1) and in TFA$\bullet\frac{1}{2}$DX (2) and the location of PYR in 2pCA$\bullet$2PYR.

5.7 FTIR analysis

The FTIR spectra for the pCA$\bullet\frac{1}{2}$DX solvate and pCA are shown in Figure 5.21. The OH band shifted from 3373 to 3209 cm^{-1} due to the hydrogen bonding between the phenolic OH in pCA and the oxygen atom of DX. The carboxylic acid OH also shifted to 2599 and 2973 cm^{-1} due to the presence of the carboxylic acid homosynthon. Figure 5.22 displays the IR spectra of pCA and the 2pCA$\bullet$2PYR solvate. The phenolic OH is shifted from 3373 to 3071 cm^{-1} due to its hydrogen bonding with the nitrogen of pyridine. The pCA carboxylic acid homosynthon caused the shift of the COOH peak from 2577 to 2605 cm^{-1}. The (TFA)$\bullet$($\frac{1}{2}$ DX) solvate also shows a shift of the phenolic OH band when compared to its starting material. The shifts are from 3432 to 3515 and

3295 cm^{-1}. The TFA carboxylic acid homosynthon also resulted in a shift of the COOH peak from 2840 to 2915 cm^{-1}, Figure 5.23.
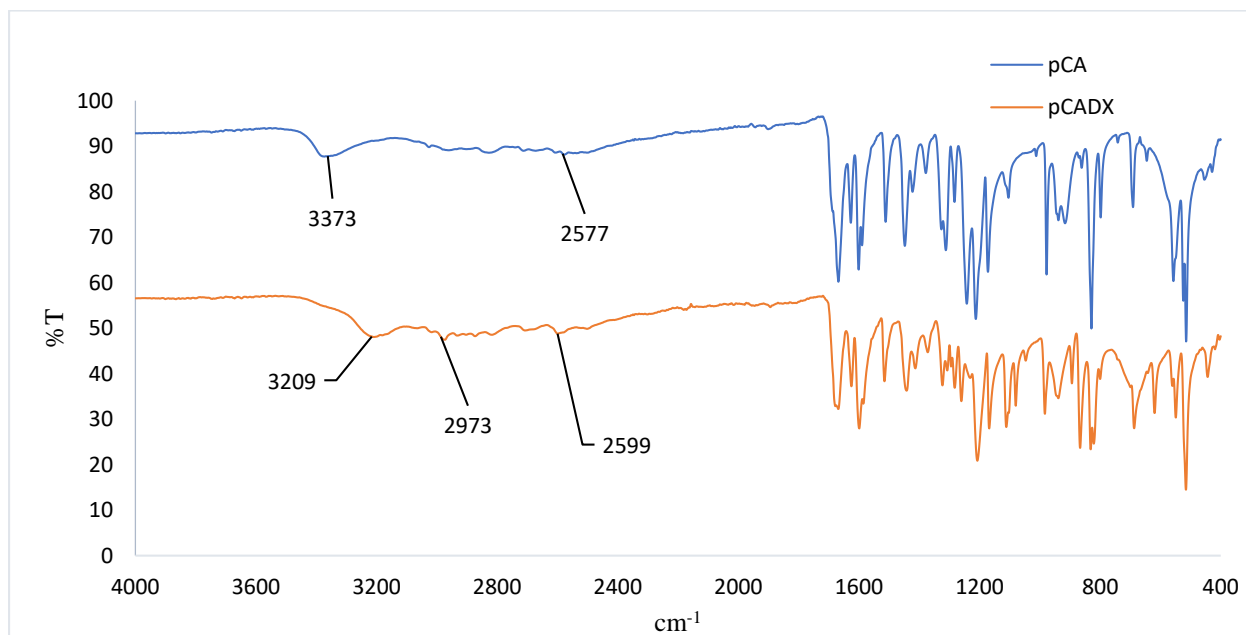

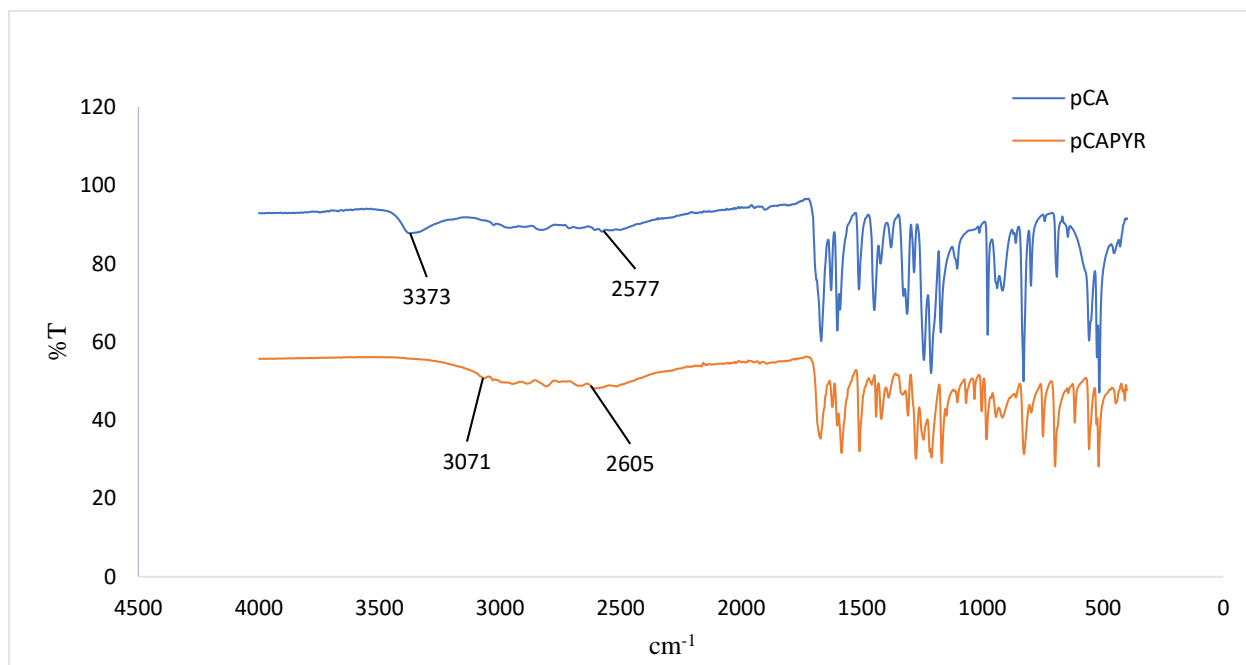Figure 5.21: FTIR spectra of pCA (blue) and pCA•$\frac{1}{2}$DX (orange).

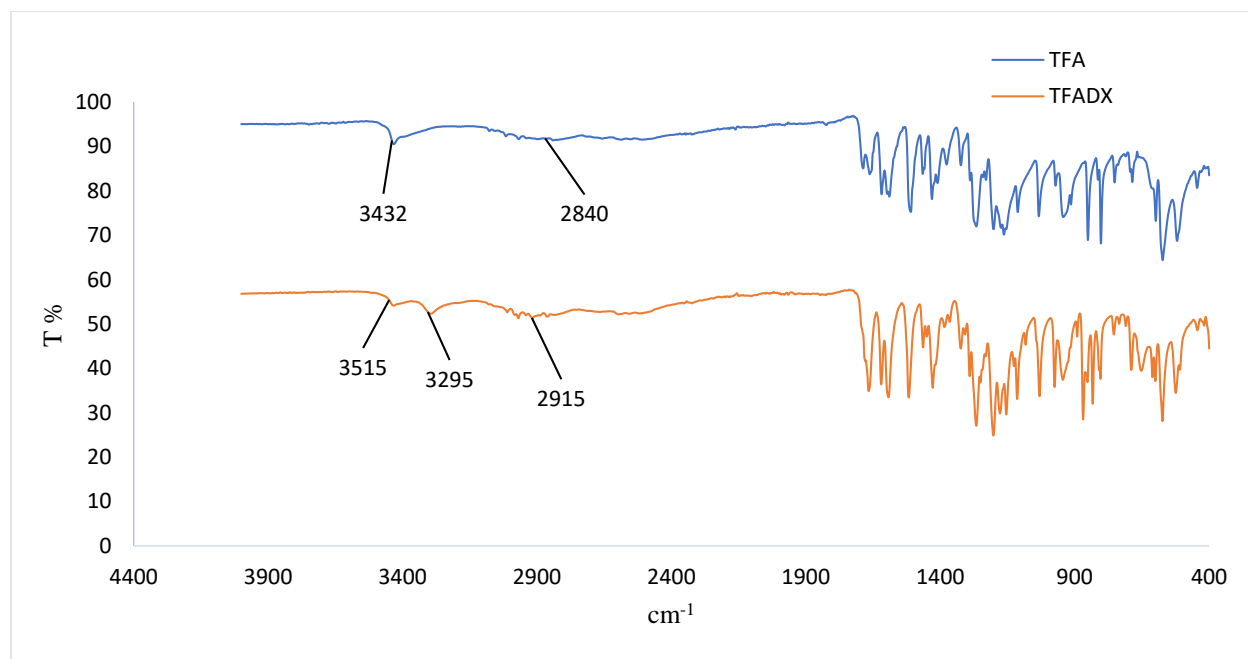Figure 5.22: FTIR spectra of pCA (blue) and 2pCA•2PYR (orange).

Figure 5.23: FTIR spectra of TFA (blue) and (TFA)•($\frac{1}{2}$DX) (orange).

5.8 Conclusion

Three solvates were obtained, pCA formed solvates with 1,4-dioxane and pyridine compared to TFA which only formed a solvate with 1,4-dioxane. The solvates crystallised in three different space groups; the orthorhombic space group Pbca for 2pCA•2PYR solvate, monoclinic P2$_1$/n space group for pCA•$\frac{1}{2}$DX solvate and the triclinic space group $P\bar{1}$ for TFA•$\frac{1}{2}$DX solvate. All three structures demonstrated the carboxylic acid homosynthon with the O-H•••O interaction forming $R_2^2(8)$ rings which indicates the robustness of this synthon. The solvate containing pyridine had both O-H•••O and O-H•••N interactions. The presence of the phenolic hydroxyl group on both pCA and TFA facilitated hydrogen bonding to the solvent molecules. Comparison of the structures showed that the packing in all the structures are different. The PXRD experiment showed that there was no reproducibility for the solvates of pCA and the TFA solvate using the grinding method. The thermal analysis revealed that the thermal stability trend was TFA•$\frac{1}{2}$DX > pCA•$\frac{1}{2}$DX > 2pCA•2PYR.

5.9 References

Cruz-Cabeza, A., 2012. Acid-base crystalline complexes and the pKa rule. *CrystEngComm,* Volume 14, pp. 6362-6365.

Etter, M., Macdonald, J. & Bernstein, J., 1990. Graph-set analysis of hydrogen bond patterns. *Acta crystallographica,* Volume 46, pp. 256-262.

Gokel, G. & Barbour, L., 2017. *Comprehensive supramolecular chemistry II.* Amsterdam: Oliver Walter.

Macrae, C. et al., 2008 . Mercury CSD 2.0 - New Features for the Visualization and Investigation of Crystal Structures. *J. Appl. Cryst.,* Volume 41, pp. 466-470

Sheldrick, G. M. , 1997. Program for the Refinement of Crystal Structures from Diffraction Data. University of Göttingen, Göttingen, Germany.

Surov, A. O., Solanko, K. A., Bond, A. D. & Bauer-Brandl, A., 2015. Diversity of felodipine solvates: structure and physicochemical properties.. *CrystEngComm,* Volume 17, p. 4089–4097.

Yvon, K., Jeitschko, W. & Parthe, E. J., 1977. LAZY PULVERIX: a computer program for calculating X-ray and neutron diffraction powder patterns. *J. Appl. Cryst.,* Volume 10, pp. 73-74.

CHAPTER 6: SUMMARY AND CONCLUSION

The design and synthesis of multicomponent crystals have considerable therapeutic and commercial benefits as they often modify physicochemical properties like solubility and bioavailability. Many factors are taken into consideration when constructing a co-crystal, salt and solvate. The functional groups of both starting material and co-former are important in predicting the formation of multicomponent crystals. For the prediction of co-crystals and salts, the focus was on the pK$_a$ rule and the study done by Cruz Cabeza. Both *p*-coumaric acid and *trans*-ferulic acid can form a heterosynthon and homosynthon due to their carboxylic acid.

In this study, eight new solid forms were successfully synthesized using *p*-coumaric acid (*p*CA) and *trans*-ferulic acid as starting materials in combination with several organic bases as co-formers. The crystals were prepared by slow evaporation methods and for their reproducibility, a solvent assisted grinding technique was used.

The co-crystals of *p*CA and TFA with 4,4'-bipyridine were both solved in the monoclinic space group *P*2$_1$/*c*. The 3(*p*CA)•3(BIPY) co-crystal had a Z' of 3 and TFA•BIPY had Z' of 1. The $C_2^2(19)$ chains in the packing diagram due to the O-H•••N hydrogen bonding is another similarity observed between the co-crystal of *p*CA to that of TFA, however, the structural packing arrangement of both co-crystals differed. The pK$_a$ rule was proven correct as the pK$_a$ difference between the starting material and BIPY indicates co-crystal formation. The thermal analysis showed that the TFA•BIPY is more stable than 3(*p*CA)•3(BIPY).

For the salts of *p*CA and TFA, the pK$_a$ rule was validated as the ΔpK$_a$ between the acids and the bases were found within the range for salt formation. This was confirmed by a proton transfer. The highest Z' in this study was observed with the 4(*p*CA$^-$) 4(2A6MP$^+$) salt. 4(*p*CA$^-$)4(2A6MP$^+$) and (*p*CA$^-$)(2A4MP$^+$) crystallized in the orthorhombic *Pbca* space group, while the (TFA$^-$)(2A4MP$^+$)•$\frac{3}{2}$(H$_2$O) crystal structure was solved in the monoclinic space group C2/*c*. $R_2^2(8)$ rings were found in all three salts due to the aminopyridinium carboxylate heterosynthon. $R_4^4(24)$ rings were observed in (TFA$^-$)(2A4MP$^+$)•$\frac{3}{2}$(H$_2$O) salt as the water molecule bridged the TFA molecules in the crystal packing arrangement.

The crystal structures of the *p*CA and TFA solvates were solved in different space groups, orthorhombic *Pbca* space group for 2*p*CA•2PYR, monoclinic P2$_1$/*n* space group for (*p*CA)•($\frac{1}{2}$DX) and triclinic P$\bar{1}$ space group for (TFA)•($\frac{1}{2}$DX). All three structures displayed the carboxylic acid homosynthon resulting in $R_2^2(8)$ rings.

The PXRD analysis revealed that the reproducibility experiment using the solvent assisted grinding technique for the co-crystals, salts and solvates of *p*CA and TFA resulted in unknown compounds. The presence of the methoxy group in TFA did not significantly affect the formation of the multicomponent crystals. Further studies should investigate the solubility and bioavailability of the co-crystals, salts and solvates of *p*CA and TFA. Additionally, the higher Z' found for certain *p*CA multicomponent crystals could be further investigated.